

# **Corrosion Protection of AA2024-T3 Alloy by Modified Hybrid Titania-Containing Sol-Gel Coatings**

A dissertation submitted to the University of Manchester  
for the degree of Master of Science by Research  
in the Faculty of Engineering and Physical Sciences

**2014**

**Feng Yu**

School of Materials  
University of Manchester

# List of Contents

LIST OF CONTENTS.....	2
LIST OF FIGURES .....	5
LIST OF TABLES.....	8
LIST OF ABBREVIATIONS .....	9
ABSTRACT.....	10
DECLARATION .....	11
COPYRIGHT STATEMENT .....	11
ACKNOWLEDGEMENTS .....	12
CHAPTER 1 INTRODUCTION .....	13
1.1    GENERAL BACKGROUND .....	13
1.2    AIMS AND OBJECTIVES.....	14
1.3    RESEARCH APPROACH .....	15
1.4    OUTLINE OF THE DISSERTATION .....	16
CHAPTER 2 LITERATURE REVIEW .....	17
2.1    CORROSION.....	17
2.1.1    Corrosion damage .....	17
2.1.2    Forms of corrosion .....	18
2.1.3    Mechanisms of corrosion .....	18
2.1.3.1    Thermodynamics of corrosion process.....	18
2.1.3.2    Kinetics of corrosion process.....	20
2.1.4    Corrosion protection .....	21
2.2    ALUMINIUM ALLOY .....	22
2.2.1    Introduction to AA2024.....	23
2.2.2    Corrosion of AA2024 .....	23
2.2.3    Corrosion protection of AA2024 .....	26
2.3    SOL-GEL TECHNOLOGY.....	28
2.3.1    Introduction to sol-gel process .....	28
2.3.2    Sol-gel coatings for corrosion protection .....	31
2.3.3    Titania-containing hybrid inorganic/organic sol-gel coating .....	32
2.4    CONDUCTING POLYMERS .....	34
2.4.1    Introduction to conducting polymers .....	34
2.4.2    Introduction to polyaniline.....	36
2.4.3    Synthesis of polyaniline.....	38
2.4.3.1    Synthesis of polyaniline nanofibers .....	41
2.4.3.2    Synthesis of polyaniline agglomerated particles.....	43
2.4.4    Corrosion protection by polyaniline .....	44

2.5	GLASS FLAKE .....	45
2.5.1	Introduction to glass flake.....	45
2.5.2	Corrosion protection by glass flake .....	46
CHAPTER 3 EXPERIMENTAL WORK .....		48
3.1	PREPARATION OF SAMPLES .....	48
3.1.1	Cleaning of AA2024 substrate.....	48
3.1.2	Synthesis of polyaniline .....	48
3.1.3	Preparation of sol-gel coatings .....	50
3.1.3.1	Synthesis of standard sol-gel .....	50
3.1.3.2	Synthesis of PVB modified sol-gel.....	51
3.1.3.3	Synthesis of PANI modified PVB sol-gel .....	51
3.1.3.4	Synthesis of GF modified PVB sol-gel.....	52
3.1.3.5	Synthesis of PANI and GF modified PVB sol-gel .....	52
3.1.3.6	Preparation of sol-gel coatings .....	53
3.2	CHARACTERIZATION TECHNIQUES .....	53
3.2.1	Scanning electron microscopy with energy dispersive X-ray spectroscopy (SEM/EDX) .....	53
3.2.2	Optical Microscopy .....	55
3.2.3	Fourier transformation infrared spectroscopy (FTIR) .....	55
3.2.4	Differential scanning calorimetry (DSC) and Thermogravimetry (TG) .....	56
3.3	TESTING TECHNIQUES .....	57
3.3.1	Electrochemical impedance spectroscopy (EIS) .....	57
3.3.2	Water drop contact angle .....	58
3.3.3	Cross-hatch adhesion testing .....	58
CHAPTER 4 RESULTS .....		61
4.1	CHARACTERIZATION OF MATERIALS .....	62
4.1.1	Surface condition of AA2024-T3 alloy .....	62
4.1.1.1	AR2024 .....	62
4.1.1.2	AD2024 .....	62
4.1.1.3	AE2024 .....	63
4.1.2	Morphology of polyaniline.....	63
4.1.2.1	PANI agglomerated particles.....	64
4.1.2.2	PANI nanofibers .....	65
4.1.2.3	Commercial PANI on carbon black.....	65
4.1.3	Morphology of glass flake.....	66
4.2	CORROSION PERFORMANCE .....	66
4.2.1	Bare AA2024 .....	67
4.2.2	Standard sol-gel coatings .....	69
4.2.3	Co-polymer modified sol-gel coatings .....	73
4.2.4	Polyaniline modified sol-gel coatings .....	77
4.2.5	Glass flake modified sol-gel coatings .....	81
4.3	PROPERTIES OF THE SOL-GEL COATINGS .....	84

4.3.1	Contact angle measurements .....	84
4.3.2	Cross-hatch adhesion tests.....	85
CHAPTER 5 DISCUSSION .....		90
5.1	PREPARATION OF MATERIALS.....	90
5.1.1	Surface pre-treatments of AA2024 alloy .....	90
5.1.2	Synthesis of nanostructured polyaniline.....	91
5.1.2.1	Chemical processes during the polymerization of aniline .....	92
5.1.2.2	Formation of different PANI nanostructures .....	93
5.1.3	Preparation of sol-gel coatings on AA2024.....	94
5.1.4	Modification of the standard sol-gel coatings .....	96
5.1.4.1	Influence on thermal properties .....	97
5.1.4.2	Influence on chemical bonding .....	98
5.2	CORROSION PERFORMANCE .....	101
5.2.1	Bare AA2024 .....	101
5.2.2	Standard sol-gel coatings.....	105
5.2.3	PVB modified sol-gel coatings.....	108
5.2.4	PANI modified sol-gel coatings .....	110
5.2.5	GF modified sol-gel coatings.....	114
CHAPTER 6 CONCLUSIONS AND FUTURE WORK .....		119
6.1	CONCLUSIONS .....	119
6.1.1	Preparation of materials .....	119
6.1.2	Properties of the sol-gel coatings .....	120
6.1.3	Corrosion performance.....	120
6.2	FUTURE WORK.....	122
REFERENCES .....		123

Word count 31,427



# List of Figures

Fig 2.1 Schematic of localized pitting corrosion of AA2024 [30].	25
Fig 2.2 Schematic presentation of components that make up an aircraft coating system [30].	26
Fig 2.3 Overview showing two synthesis examples by the sol-gel method; (a) films from a colloidal sol; (b) powders from a colloidal sol transformed into a gel [64].	29
Fig 2.4 The general scheme of sol-gel process of silicon alkoxide precursor [56].	30
Fig 2.5 Schematic representation of enhanced compatibility of different paint systems with an epoxy-functional hybrid sol-gel coating [67].	31
Fig 2.6 Representation of energy bands in insulator, semiconductor and conductor [85].	34
Fig 2.7 Conductivity range of ICPs varies from doping degree [88].	35
Fig 2.8 Conductivity of doped and undoped trans-(CH) <sub>x</sub> and emeraldine polyaniline [89].	36
Fig 2.9 Molecular structure of typical ICPs.	36
Fig 2.10 Schematic diagram showing the molecular structure, synthesis chemistry, reversible acid/base doping/dedoping, and redox chemistry of PANI [95].	38
Fig 2.11 Overall reaction of chemical oxidation synthesis of PANI ES [129].	40
Fig 2.12 Synthesis of different nanostructured PANI from various synthetic conditions [131].	40
Fig 2.13 Schematic illustration of the synthesis of polyaniline nanofibers by a rapidly mixed reaction [132].	42
Fig 2.14 Schematic illustration of the synthesis of polyaniline nanofibers using interfacial polymerization [132].	42
Fig 2.15 Schematic illustrations of the formation and aggregation of polyaniline particles. The green fibers and purple dots represent polyaniline particles that result from homogeneous and heterogeneous nucleation, respectively [133].	42
Fig 2.16 SEM images of PANI nanofibers made with following dopant acid in interfacial polymerization: (a) HCl, (b) H <sub>2</sub> SO <sub>4</sub> , (c) HNO <sub>3</sub> , and (d) HClO <sub>4</sub> [102].	43
Fig 2.17 Schematic diagram illustrating the formation of PANI agglomerates during conventional chemical synthesis [103].	43
Fig 2.18 Mechanism of PANI corrosion protection on aluminium [139].	44
Fig 2.19 SEM images of advanced nano glass flake [144].	45
Fig 2.20 The tortuous path effect [144].	46
Fig 3.1 Chemical formula of the PVB [154].	51
Fig 3.2 Image showing dip-coating method for preparation of sol-gel coatings.	53

Fig 3.3 Image of Quanta 200 FEG SEM/EDX.....	54
Fig 3.4 Images of Zeiss AXIO Lab.A1 2-D Optical Microscope (left) and Bruker ContourGT-I 3D Optical Microscope (right).....	55
Fig 3.5 Image of Thermo Electron FTIR Nicolet 5700 with diamond ATR unit. .	56
Fig 3.6 Images of Q-100 DSC (left) and Q-500 TGA (right) from TA instruments. .....	56
Fig 3.7 Image of typical aerated three-electrode cell used for EIS measurements .....	57
Fig 3.8 Image of FTA 188 Video Tensiometer used in this study.....	58
Fig 3.9 Schematic illustrations for the operation procedures of cross hatch adhesion test according to ASTM D3359-09E2 standard [157]. ....	59
Fig 4.1 SEM images of AR2024 surface. ....	62
Fig 4.2 SEM images of AD2024 surface. ....	63
Fig 4.3 SEM images of AE2024 surface. ....	63
Fig 4.4 SEM images of PANI ES agglomerated particles .....	64
Fig 4.5 SEM images of PANI ES nanofibers.....	65
Fig 4.6 SEM images of PANI ES on carbon black. ....	66
Fig 4.7 SEM images of GF001 glass flake.....	66
Fig 4.8 Bode (upper) and phase angle (bottom) plots of bare AR2024, AD2024 and AE2024 in 3.5% NaCl solution at 1h, 1 day and 8 days immersion. ...	68
Fig 4.9 Optical microscopy images of bare AR2024 (left), AD2024 (middle) and AE2024 (right) (a) before and (b) after 8 days immersion in 3.5% NaCl solution; (c) Digital images after 8 days immersion.....	69
Fig 4.10 Bode (upper) and phase angle (bottom) plots of standard sol-gel coated AR2024 (AR2024_SG), AD2024 (AD2024_SG) and AE2024 (AE2024_SG) in 3.5% NaCl solution at 1hour, 8 and 24 hours immersion. .....	70
Fig 4.11 Cross-section SEM images of standard sol-gel coatings on AR2024 (left), AD2024 (middle) and AE2024 (right).....	72
Fig 4.12 Optical microscopies(a),(b) of bare AR2024_SG (left), AD2024_SG (middle) and AE2024_SG (right) (a) before and (b) after 8 days immersion in 3.5% NaCl solution and (c) digital images after 8 days immersion. ....	73
Fig 4.13 Bode (upper) and phase angle (bottom) plots of PVB modified sol-gel coatings on AE2024 in 3.5% NaCl solution at 1 hour, 1 day and 4 days immersion. Volume ratios of PVB (10wt% solution in ethanol) versus the standard sol-gel were SG_PVB_4 and SG_PVB_8. ....	74
Fig 4.14 Cross-section SEM images of PVB containing sol-gel coatings, SG_PVB_8 (left), SG_PVB_4 (right).....	75
Fig 4.15 Optical micrographs of SG_PVB_8 (left) and SG_PVB_4 (right) (a) before and (b) after 8 days immersion in 3.5% NaCl solution and (c) digital images after 8 days immersion. ....	76
Fig 4.16 Cross-section SEM images of PANI_NF modified PVB sol-gel coatings. .....	78

Fig 4.17 Bode(upper) and phase angle (bottom) plots of PANI containing PVB sol-gel coatings on AE2024 in 3.5% NaCl solution at 1 hour, 4 days and 8 days immersion. (PANI_AP/NMP_PVB, PANI_NF/NMP_PVB and PANI_CB/NMP_PVB refers to the addition of PANI ES agglomerated particles, nanofibers and carbon black composites into SG_PVB_4 sol-gels, respectively.) .....	78
Fig 4.18 Optical micrographs of PANI_AP/NMP_PVB (left), PANI_NF/NMP_PVB (middle) and PANI_CB/NMP_PVB (right) (a) before and (b) after 8 days immersion in 3.5% NaCl solution and (c) Digital images after 8 days immersion. ....	80
Fig 4.19 Bode(upper) and phase angle (bottom) plots of glass flake containing PVB sol-gel coatings(GF001_PVB) on AE2024 in 3.5% NaCl solution at 1 hour, 1 days, 4 days immersion and combination of GF001 and PANI ES nanofibers (GF001_PANI_NF/NMP_PVB) at 1 hour, 4 days and 8 days immersion. ....	82
Fig 4.20 Optical micrographs of GF001_PVB (left) and GF001_PANI_NF/NMP_PVB (right) (a) before and (b) after 8 days immersion in 3.5% NaCl solution and (c) Digital images after 8 days immersion. ....	83
Fig 4.21 Contact angle for the surface of bare AA2024 and various sol-gel coatings. ....	85
Fig 4.22 Typical optical micrographs showing the condition of all the coatings after cross-hatch adhesion tests at dry (left) and wet (right) environment. ....	89
Fig 5.1 Proposed mechanism for polymerization of aniline by Wei et al [177]. ....	93
Fig 5.2 DSC/TG curves for standard sol-gel and PVB, PANI, GF001 modified sol-gel. ....	97
Fig 5.3 FTIR spectra of standard sol-gel coating and PVB, PANI, GF001, GF001/PANI modified sol-gel coatings .....	99
Fig 5.4 Two typical EECs used for the simulation of bare AA2024 immersed in 3.5% NaCl solution. ....	102
Fig 5.5 Nyquist plots of bare AA2024 alloy in 3.5% NaCl solution during 1 hour, 1 day and 8 days immersion for AR2024, AD2024 and AE2024. ....	103
Fig 5.6 SEM image of pits on AA2024 (Insert is Cu-rich aggregate) [51]. ....	104
Fig 5.7 Nyquist plots of standard sol-gel coated AA2024 in 3.5%NaCl solution during 1, 8 and 24 hours immersion for AR2024_SG, AD2024_SG and AE2024_SG. ....	105
Fig 5.8 Two typical EECs used for the analysis of sol-gel coated AA2024 immersed in 3.5% NaCl solution. ....	106
Fig 5.9 Nyquist plots of PVB modified sol-gel coated AA2024 in 3.5%NaCl solution for 1 hour, 1 day and 4 days immersion. ....	109
Fig 5.10 Nyquist plots of PANI AP and NF modified sol-gel coated AA2024 in 3.5%NaCl solution during 1 hour, 1 day, 4 days immersion and PANI CB modified coatings during 1 hour and 4 hours immersion. ....	111

Fig 5.11 EEC used for the simulation of PANI AP and NF modified coatings in 3.5% NaCl solution during 8 days immersion. ....	111
Fig 5.12 Images of three PANI modified sol-gels on glass slides; PANI_AP/NMP_PVB (left), PANI_NF/NMP_PVB (middle), PANI_CB/NMP_PVB (right) .....	113
Fig 5.13 Nyquist plots of GF001 modified PVB and PANI NF sol-gel coatings on AA2024 in 3.5%NaCl solution during 1 hour, 1 day, 4 days immersion and additional 8 days for GF001_PANI_NF/NMP_PVB coating. ....	115
Fig 5.14 Optical image of GF001 modified PANI sol-gel coating on 1 $\mu$ m mirror finished AA2024.....	117
Fig 5.15 Interferometry images of GF001 modified sol-gel coatings showing buried (left) and protruded (right) GF001. ....	117

## List of Tables

Table 3.1 Percent chemical composition of AA2024-T3 aluminium [151, 152].	48
Table 3.2 Chemical compositions of GF001 glass flakes [155].....	52
Table 3.3 Properties of GF001 glass flakes [155]. ....	52
Table 3.4 Descriptions and results for cross hatch adhesion test according to ASTM D3359-09E2 standard [157].....	60
Table 4.1 Cross-hatch adhesion for the surface of bare AA2024 and various sol-gel coatings.....	86
Table 5.1 Assignments for the peaks highlighted in the FTIR spectra of sol-gel coatings. ....	100
Table 5.2 Parameters of standard sol-gel coated AA2024 system after fitting the EIS data with different EECs.....	106
Table 5.3 Parameters of standard and PVB modified sol-gel coated AA2024 system after fitting the EIS data with different EEC in Fig 5.8 (a). ....	110
Table 5.4 Parameters of PVB and PANI modified sol-gel system after fitting the EIS data with different EECs in Fig 5.8 (a) and Fig 5.11.....	112
Table 5.5 Parameters of GF001 modified and unmodified PVB and PANI sol-gel system after fitting the EIS data with different EECs in Fig 5.8 (a) and Fig 5.11.....	115

# List of Abbreviations

AA2024	AA2024-T3 Aluminium Alloy
AR2024	As Received AA2024, Cleaned with Acetone
AD2024	30% HNO <sub>3</sub> Desmuted AA2024
AE2024	10% NaOH Etched, 50% HNO <sub>3</sub> Desmuted AA2024
IMP	Intermetallic Particles
ICP	Intrinsically Conducting Polymers
ANI	Aniline
APS	Ammonium Peroxodisulphate
PANI	Polyaniline
PNB	Polyaniline in Pernigraniline Base form
LB	Polyaniline in Leucoemeraldine Base form
EB	Polyaniline in Emeraldine Base form
PANI ES AP	Polyaniline Emeraldine Salt Agglomerated Particles
PANI ES NF	Polyaniline Emeraldine Salt Nanofibers
PANI ES CB	Polyaniline Emeraldine Salt on Carbon Black
i-PrOH	Isopropanol
GPTMS	3-Glycidoxypolydimethylmethoxydimethylsilane
VTES	Vinyltriethoxysilane
TIP	Titanium Isopropoxide
AcEt	Ethyl Acetoacetate
NMP	N-methyl-2-pyrrolidone
PVB	Polyvinyl Butyral
GF/GF001	Glass Flake/Glass Flake 001
SEM	Scanning Electron Microscopy
FTIR	Fourier Transformation Infrared Spectroscopy
DSC	Differential Scanning Calorimetry
TG	Thermogravimetry
EIS	Electrochemical Impedance Spectroscopy
SG/Standard sol-gel coating	Hybrid Titania-Containing Sol-gel Coating (Si:Ti=4)
AR2024_SG	Standard Sol-Gel Coatings on AR2024
AD2024_SG	Standard Sol-Gel Coatings on AD2024
AE2024_SG	Standard Sol-Gel Coatings on AE2024
SG_PVB_8	V(SG)/V(PVB 10% ethanol solution)=8(20/2.5)
SG_PVB_4	V(SG)/V(PVB 10% ethanol solution)=4(20/5.0)
SG_PVB_2	V(SG)/V(PVB 10% ethanol solution)=2(20/10.0)
PANI_AP/NMP_PVB	2% PANI ES AP dispersion in NMP(3.0ml) added into the as-prepared SG_PVB_4(25ml)
PANI_NF/NMP_PVB	2% PANI ES NF dispersion in NMP(3.0ml) added into the as-prepared SG_PVB_4(25ml)
PANI_CB/NMP_PVB	2% PANI ES CB dispersion in NMP(3.0ml) added into the as-prepared SG_PVB_4(25ml)
GF001_PVB	2.5% GF001 in 5.0ml PVB solution added into the as-prepared prepare SG_PVB_4(25ml)
GF001_PANI_NF/NMP_PVB	GF001_PVB with further addition of 2% PANI ES NF dispersion in NMP(3.0ml)
OCP	Open Circuit Potential
EEC	Equivalent Electrical Circuits
CPE	Constant Phase Elements
R <sub>s</sub>	Solution Resistance
R <sub>pore</sub>	Pore Resistance
Q <sub>coat</sub>	Coating Capacitance
R <sub>in</sub>	Intermediate Layer Resistance
Q <sub>in</sub>	Intermediate Layer Capacitance
R <sub>ox</sub>	Oxide Film Resistance
Q <sub>ox</sub>	Oxide Film Capacitance
R <sub>ct</sub>	Charge Transfer Resistance
Q <sub>dl</sub>	Double Layer Capacitance
W	Warburg Element

# Abstract

It is widely known that AA2024-T3 aluminium alloys are susceptible to localized corrosion. Corrosion protection of AA2024 has historically been via chromate treatments and chromate-containing coatings, which are shortly to be banned due to the hazardous and carcinogenic nature of Cr (VI).

Hybrid sol-gel coatings are promising systems to replace chromates for the corrosion protection of AA2024. However, due to the porous nature of sol-gel coatings, they have limited protection properties and need to be used together with functional polymers, inhibitors and barrier pigments. Candidate systems for improving the corrosion resistance of sol-gel coatings include; the co-polymer polyvinyl butyral (PVB) for reducing the porosity of organic coatings, the conductive polymer, polyaniline (PANI) as an efficient corrosion inhibitor and glass flake (GF) as an excellent barrier pigment.

In this study, a hybrid titania-containing sol-gel coating, designated the 'standard system', was modified by PVB, PANI and GF to investigate the influence of these pigments for the corrosion protection of AA2024.

Electrochemical impedance spectroscopy (EIS) results of these coatings immersed in 3.5% NaCl solution revealed that the modification by PVB in a volume ratio of sol-gel/PVB=4:1 can increase the resistance to electrolyte ingress of the sol-gel layer, whilst the PANI in agglomerate-type particles can produce a stable intermediate layer between the coating and substrate. No obvious improvement was observed by the addition of GF.

Differential scanning calorimetry and thermogravimetry (DSC/TG) analysis and water contact angle measurements indicated that GF increase the thermal stability and decrease the hydrophobicity of the standard coating, while PVB/PANI had negative and positive effects on both properties, respectively. Cross-hatch adhesion tests showed high adhesion strength between all the modified coatings and alkaline etched AA2024. Fourier transformed infrared spectroscopy (FTIR) analysis suggested that all these pigments affected the hydrolysis and condensation reactions taking place during the sol-gel synthesis.

**Keywords:** AA2024-T3 aluminium alloys, Corrosion protection, Hybrid sol-gel coating, Polyvinyl butyral, Polyaniline, Glass flake.

# Declaration

No portion of the work referred to in the dissertation has been submitted in support of an application for another degree or qualification of this or any other university or other institute of learning.

Signature

# Copyright Statement

The author of this dissertation (including any appendices and/or schedules to this dissertation) owns any copyright in it (the "Copyright") and s/he has given The University of Manchester the right to use such Copyright for any administrative, promotional, educational and/or teaching purposes.

Copies of this dissertation, either in full or in extracts, may be made only in accordance with the regulations of the John Rylands University Library of Manchester. Details of these regulations may be obtained from the Librarian. This page must form part of any such copies made.

The ownership of any patents, designs, trademarks and any and all other intellectual property rights except for the Copyright (the "Intellectual Property Rights") and any reproductions of copyright works, for example graphs and tables ("Reproductions"), which may be described in this dissertation, may not be owned by the author and may be owned by third parties. Such Intellectual Property Rights and Reproductions cannot and must not be made available for use without the prior written permission of the owner(s) of the relevant Intellectual Property Rights and/or Reproductions.

Further information on the conditions under which disclosure, publication and exploitation of this dissertation, the Copyright and any Intellectual Property Rights and/or Reproductions described in it may take place is available from the Head of School of Materials.

# Acknowledgements

I would like to express my sincerest gratitude to my supervisor Professor Robert Akid for his guidance over the last year. Without his great support on experiments and funding, expert advice on concept and progress, patient assistance on understanding and revision of this dissertation, it would be impossible for me to finish this mater project alone. One year cooperation with him was really an enjoyment of scientific research and corrosion study.

I would like to thank my co-supervisor Dr Robert Lindsay and course director Dr Xiaorong Zhou for their helpful guidance and suggestions through my study and research as well as Professor Peter Skelton, Professor Stuart Lyon, Dr Rafael Leiva-García, Dr Clara Escrivá-Cerdan, Dr Yuanfeng Yang, Dr Suzanne Morsch, Dr Tony Cook, Dr Yanwen Liu, Dr Andronikos Balaskas, Dr Alex Cassell, Mr Federico García-Galván, Mr Steve Blatch, Mr Simon Smith, Mr Paul Jordan, Mr Teruo Hashimoto, Mr Patrick Hill, Mr Hong Liu, Mrs Polly Greensmith and all the colleagues in BP lab for their important help on providing either conceptual or experimental suggestions and help. I would like to thank Professor Robert Freer, Dr Joe Robson, Dr Zhu Liu, Dr Michele Curioni, Dr Nick Stevens and Dr Dirk Engelberg for their help on introducing basic knowledge of either materials or corrosion during the taught units and Mrs Olwen Richert for her assistance on the problems in my programme.

I would like to thank Professor David Leigh, Ms Valerie Bruyr from the School of Chemistry and Professor Krishna Persaud, Dr Danesh Ehsan from the School of Chemical Engineering and Analytical Science for their kind assistance on preparation of polyaniline. I would like to thank Dr Gittens Jeanette from Sheffield Hallam University, Mr Charles Watkinson from CorroCoat UK, Mr Dave Gray from IMCD UK Ltd, Mr John Fletcher from Elcometer UK for their generous donation of materials or suggestions on the use of equipment as well as generous financial support from BP.

Last but not least, I would like to give my deepest gratitude to my family, especially my parents and brother, and best friends, who gave me so much support, care, encouragement and love so that I could overcome the difficulties over the last year.



# Chapter 1 Introduction

## 1.1 General background

Corrosion has always been a problem in society, especially in an economic sense in that it costs approximately 3-4% Gross National Product of many countries. Direct corrosion damage also increases the risk to safety and lack of conservation. Besides some common problems raised from indirect corrosion damage, including plant shutdown and contamination of products, many catastrophic failures may also bring serious problems to the society and humans, such as leaking of toxic chemicals and breakdown of bridges or nuclear power plants.

As the most widely used non-ferrous metal, aluminium has a long track history for the application in various important industries, including aircrafts, automobiles and construction. The alloy AA2024-T3 has the advantage of high strength to weight ratio being particularly important for the aerospace industry and is perhaps the best known of the Al alloys. Unfortunately, due to the introduction of alloying elements, notably Cu, AA2024 is susceptible to localized corrosion, especially in chloride containing environments.

Chromate based conversion coatings have achieved remarkable successes in the corrosion protection of AA2024 over many decades. However, the toxic and carcinogenic nature of chromium (VI) from these coatings has limited their application. A ban on these products is due to the increasing restrictions imposed by environmental legislation. As a result, this is leading to an increasing demand for environmentally friendly corrosion protection coatings.

Among all the alternatives to chromate conversion coatings, hybrid sol-gel coatings are showing promise, owing to ability to form thin films at low cure temperatures, excellent adhesion between the metal and topcoat, and importantly, their non-toxic properties. Moreover, the combination of both the benefits from inorganic ceramics and organic networks also provides the hybrid sol-gel coatings with excellent durability, scratch resistance, flexibility and

functional compatibility with organic paints. In addition, a good candidate for the replacement of chromate conversion coatings is that of conductive polymers, especially polyaniline (PANI), which is an interesting material for corrosion inhibition, due to the redox-active nature of PANI and its good stability in many systems.

As an excellent binder, the co-polymer Polyvinyl butyral (PVB) is superior in providing effective adhesion between organic coatings and metals, along with providing cross-linking properties for sol-gel coatings. High aspect ratio glass flake (GF), especially at nanoscale, has been successfully applied as an efficient physical barrier pigment in organic coatings for corrosion protection of metals. With the addition of glass flake, not only the mechanical properties but also the lifetime of organic coatings may be significantly improved.

In this study, a conductive polymer, PANI, a co-polymer of PVB and commercial corrosion resistant GF are used as pigments to modify a hybrid titania-containing sol-gel coating. An investigation on the modified sol-gel coatings was carried out for the corrosion protection of AA2024 alloy.

## 1.2 Aims and objectives

To meet the increasing demand for chromate conversion coating alternatives, a hybrid titania-containing sol-gel coating has been newly developed. However, corrosion protection for AA2024 by this coating is still limited due to the porous nature of hybrid sol-gel network.

The aim of this project is therefore to improve the performance of this coating for the corrosion protection of AA2024 and investigate the influences of different pigments on the hybrid titania-containing sol-gel coating.

The main objectives of the project are

1. To produce a dense thin film and increase the adhesion strength between the substrate and the sol-gel coating. Modification by the co-polymer of PVB may be

promising in achieving this goal, due to additional cross-linking properties introduced by PVB and its excellent binding properties.

2. To stabilise active corrosion inhibitors in the sol-gel network, which may provide long term corrosion protection properties. The addition of PANI, which predominantly acts as an anodic corrosion inhibitor, may be promising to improve the corrosion performance of the standard sol-gel coating.

3. To introduce additional physical barrier properties to the porous sol-gel network and decrease the permeability of aggressive species. From this point of view, corrosion resistant glass flake may be an ideal candidate and improvement may be obtained if used appropriately.

## 1.3 Research approach

To cover the aims and objectives listed above, this study is divided into two parts. In the first part, different surface pre-treatments for cleaning AA2024 alloy were studied on bare substrate of AA2024, as variations in properties of the substrate surface may be introduced by an inappropriate cleaning procedures, which influence subsequent performance of the sol-gel coatings.

In the second part, binary, ternary and quaternary systems were studied to evaluate the effect these pigments had on the corrosion performance of the sol-gel coatings.

In this study, scanning electron microscopy (SEM) was used to characterize the surface of AA2024, morphology of both PANI and GF as well as the cross-section thickness of the sol-gel coatings. Electrochemical impedance spectroscopy (EIS) was used to investigate the corrosion behaviour of bare AA2024 and sol-gel coated samples in 3.5% NaCl solution. Optical microscopy was used to compare the alloy and coating surface of AA2024 before and after corrosion, as well as evaluate the adhesion properties of the different coating systems to the substrate. Cross-hatch adhesion tests and water drop contact angle measurements were

used to study the adhesion strength and surface hydrophobicity of the coatings, respectively. Differential scanning calorimetry (DSC) and thermogravimetry (TG) were used to compare the thermal stability of different sol-gel coatings and study the influence of coating formulation on curing temperature. Fourier transform infrared spectroscopy (FTIR) was used to study the influence of these pigments on the chemical bonding properties in comparison to that of the standard sol-gel coating.

## 1.4 Outline of the dissertation

To provide essential background information of the research, chapter 2 provides a review of literature. The concept of corrosion, aluminium alloy, sol-gel process, conducting polymers and glass flakes, along with general corrosion protection, corrosion protection of AA2024 alloy, corrosion protection by sol-gel coatings, conducting polymers and glass flake were briefly reviewed in this chapter. The details of cleaning processes of AA2024 alloy, preparation procedures of PANI and sol-gel coatings along with characterization and testing techniques were given in chapter 3. Chapter 4 presents the results on the morphology of different AA2024 alloy surface, different nanostructured PANI and glass flake, the corrosion performance of substrates cleaned under different conditions and performance of standard and modified sol-gel coatings, and surface hydrophobicity and adhesion strength between the coatings.

Chapter 5 discusses the influence of cleaning procedures on substrate behaviour; the synthesis of different nanostructured PANI, preparation of hybrid sol-gel coatings; the influence of formulation modifications on corrosion resistance in comparison to the standard coating. Finally, general conclusions and some recommendations for future work are given in chapter 6.

# Chapter 2 Literature Review

## 2.1 Corrosion

Corrosion is generally described as the result of interaction between materials and the environment. The term corrosion is associated with metals only. The term environment, normally aggressive to the materials, may range from humid air and marine water to soils etc. The magnitude of corrosion does not depend on the materials or environment alone, but upon the positive or negative interaction between them [1]. More specifically, corrosion is defined as the destructive attack of a metal or alloy by the chemical or electrochemical reaction with the environment, leading to a gradual degradation of the material. Physically deterioration of materials, e.g., galling, erosion or wear is not termed as corrosion, however in some cases, physical deterioration is accompanied by chemical degradation of the materials, for example, erosion-corrosion or tribocorrosion [2, 3].

### 2.1.1 Corrosion damage

Corrosion damage is mainly divided into three aspects, including loss of economy, failure of safety and lack of conservation. According to recent studies [1, 4], the direct economic loss of corrosion is approximately 3-4% of the Gross National Product (GNP) in the United States, Great Britain, China, Australia, Japan and many other countries. Although indirect loss of the economy is difficult to assess, some important types include, plant shutdown, loss of product and plant efficiency, contamination of products and overdesign. Corrosion of operating equipment materials could lead to catastrophic failure of, for example, pressure vessels, toxic chemical metallic containers, bridges and especially nuclear power plants. The lack of conservation for metals is not only a bare loss of materials, but also

a waste of energy as well as human efforts and raw materials required for the lost metals [2].

## 2.1.2 Forms of corrosion

Corrosion of materials may be classified into numerous forms, as shown below [5]:

1. Uniform corrosion
2. Intergranular corrosion
3. Galvanic corrosion
4. Crevice corrosion
5. Pitting corrosion
6. Erosion corrosion
7. Stress corrosion cracking
8. Biological corrosion
9. Selective leaching

The order of this list does not mean any order of importance and each form would need to be considered for a specific couple of metal and environment.

## 2.1.3 Mechanisms of corrosion

### 2.1.3.1 Thermodynamics of corrosion process

Generally, corrosion processes follow the First and Second Law of thermodynamics [6].

The energy conservation principle in the First Law of thermodynamics defines that the internal energy change in a corrosion system is equal to the sum of work done to or by a corrosion system and the heat released or absorbed by a corrosion system, according to equation (2-1).

$$\Delta U = W + Q \quad (2-1)$$

Where

- $\Delta U$  is the internal energy change in a corrosion system (J)
- $W$  is the work done to or by a corrosion system (J)
- $Q$  is the heat released or absorbed by a corrosion system (J)

A closed corrosion system then follows the Second Law of thermodynamics, which also refers to the entropy principle. In case of constant pressure and temperature, the Gibbs free energy of a corrosion system must decrease for the corrosion process to be spontaneous. The Gibbs free energy is presented in the form of enthalpy and entropy, according to equation (2-2).

$$G=H-TS \quad (2-2)$$

Where

- $G$  is the Gibbs free energy ( $\text{J}\cdot\text{mol}^{-1}$ )
- $H$  is the enthalpy ( $\text{J}\cdot\text{mol}^{-1}$ )
- $S$  is the entropy ( $\text{J}\cdot\text{mol}^{-1}\cdot\text{K}^{-1}$ )
- $T$  is the absolute temperature (K)

For electrochemical corrosion reactions in aqueous solutions [7], Faraday's law relates the Gibbs free energy to electrode potential as shown in equation (2-3).

$$\Delta G=-nEF \quad (2-3)$$

Where

- $\Delta G$  is the Gibbs free energy change ( $\text{J}\cdot\text{mol}^{-1}$ )
- $E$  is the reversible electrode potential at constant temperature and pressure (V)
- $F$  is the Faraday's constant ( $96,485 \text{ C}\cdot\text{mol}^{-1}$ )
- $n$  is the number of electrons transferred during the reaction

It is important to note that the potential in the equation (2-3) is the standard electrode potentials, where reactants and products are in their standard states.

The relationship between actual reversible potential and standard reversible potential of an electrode may be expressed by the Nernst equation. Taking anodic reaction of metallic dissolution reaction



for an example, the Nernst equation can be expressed as

$$E=E^0+\frac{RT}{nF}\ln\alpha M^{n+} \quad (2-5)$$

Where

- E is the actual reversible potential of anodic reaction (V)
- $E^0$  is the standard reversible potential of anodic reaction (V)
- R is the universal gas constant ( $8.314 \text{ J}\cdot\text{K}^{-1}\cdot\text{mol}^{-1}$ )
- T is the absolute temperature (K)
- $\alpha$  is the chemical activity for the metal ions
- F is the Faraday constant ( $96,485 \text{ C}\cdot\text{mol}^{-1}$ )
- n is the number of electrons transferred in the anodic reaction

#### 2.1.3.2 Kinetics of corrosion process

While a corrosion process may be considered spontaneous in thermodynamics aspect, this information does not indicate the rate of corrosion reaction. Corrosion kinetics is determined from the relationship between electrode potential and current flow between the anode and cathode. For determining the rate of uniform corrosion, McCafferty [8] suggested a number of methods as listed below:

1. Weight loss
2. Chemical analysis of the solution
3. Metal thickness measurements
4. Electrical resistance probes
5. Electrochemical techniques

For electrochemical corrosion, the charge transfer can be directly related to mass change according to Faraday's law, it is therefore available to determine the corrosion rate of metal from current of the corrosion process with equation (2-6) [9, 10].

$$CR=\frac{M}{nF\rho}i_{\text{corr}} \quad (2-6)$$



Where

- CR is the corrosion rate of metal ( $\text{mm}\cdot\text{year}^{-1}$ )
- M is the molar mass of the metal ( $\text{g}\cdot\text{mol}^{-1}$ )
- n is the number of electrons transferred during metal dissolution
- F is the Faraday constant ( $96,485 \text{ C}\cdot\text{mol}^{-1}$ )
- $\rho$  is the mass density of the metal ( $\text{g}\cdot\text{cm}^{-3}$ )
- $i_{\text{corr}}$  is the current density of the corrosion process ( $\text{A}\cdot\text{m}^{-2}$ )

## 2.1.4 Corrosion protection

Strategies for corrosion protection of metals may be mainly summarized into three categories, including cathodic protection, corrosion inhibition and protective coatings [1, 11].

In terms of cathodic protection, sacrificial anode systems and impressed current cathodic protection systems are extensively employed in concrete structures, pipeline systems, petroleum storage tanks and metallic structures in seawater [12-14].

Corrosion inhibition with inhibitors, may be classified as either passivation inhibitors (e.g. Chromate), organic inhibitors (e.g. Benzoate) or precipitation inhibitors (e.g. Sodium pyrophosphate), have various mechanisms of protection including interface inhibition, electrolyte layer inhibition, membrane inhibition and passivation [15]. Corrosion protection by inhibitors also has wide applications in oil and gas industries, reinforcing steels in concrete and mining industries [16].

For protective coatings, three types are mainly used for corrosion protection of metals, including metallic coatings, inorganic coatings and organic coatings [2].

The three major protective mechanisms are based upon; a barrier effect, an inhibition effect and a galvanic effect [17].

Generally, anticorrosive metallic coatings provide anodic protection from noble metal coatings (Ni, Cr, Ti, Pb), cathodic protection by sacrificial metal coatings (Zn, Ca, Mg) or mixed control protective coatings (phosphate, chromate) [7].

Inorganic coatings are usually made of natural minerals, amongst which zinc silicate was once the most extensively applied. Another significant type of inorganic coating is the sol-gel coating, which creates solid ZnO, SiO<sub>2</sub> or SiO<sub>2</sub>-TiO<sub>2</sub> barrier inorganic network from liquid organic precursors for corrosion protection of metals [17].

Typically, organic coatings are utilized to prevent or reduce the contact of corrosive species with a metal surface [10]. Resins (e.g. Acrylic resins, polyester resins, amino resins, epoxy resins), waxes, oils and latexes are commonly used organic coatings for corrosion protection [18]. Organic coatings are rarely used alone, but in combination with a conversion or anodized coatings [10, 19].

## 2.2 Aluminium alloy

As the most widely used non-ferrous metal and the most abundant metallic element in the earth crust, the production and application of aluminium and its alloys have been increasing since 1950s. While the naturally formed oxide on pure aluminium provides excellent anticorrosion properties, the key intrinsic drawback of pure aluminium is its poor mechanical properties such as strength and ductility, which have greatly limited its applications. The addition of alloying elements improves the mechanical properties, whilst cost effectively retaining the core advantages of pure aluminium, such as lightness, thermal and electrical conductivity [20]. Typical alloying elements include copper, manganese, magnesium, silicon, iron, zinc and other minor constituents. From a metallurgical point of view, aluminium alloys are generally classified into two types; wrought and cast alloys. Wrought alloys are semi-finished products and subsequent work is required to make end-use products. Cast aluminium alloys are final or near-

final products, which are produced by pouring molten alloys into a mould followed by cooling to give the final shape [21, 22].

### 2.2.1 Introduction to AA2024

With the very high strength to weight ratio, aluminium alloys are particularly important structural materials for aerospace industries. Among various aerospace aluminium alloys, AA2024 is one of the most extensively used due to its excellent strength to weight ratio and good fatigue resistance. AA2024 is the best known aluminium alloy in the 2xxx group, whose primary alloying element is copper. AA2024-T3 is solution heat treated, cold worked and naturally aged to a substantially stable condition to produce the desired mechanical properties [9]. It is important to note that the introduction of Cu (up to 5wt%) to the aluminium alloy, whilst increasing strength, leads to the formation of supersaturated solid solution particles or Cu-rich intermetallic particles (IMP), which are heterogeneously distributed throughout the alloy [23].

The most predominant IMP in AA2024 is found to be the S-phase precipitates ( $\text{Al}_2\text{CuMg}$ ) with 60% volume out of all the IMPs and 3% of the geometrical surface area of the alloy [24]. The second largest type of IMP is  $\text{Al}_6(\text{Cu}, \text{Fe}, \text{Mn})$ , which comprise about 12% volume of all the precipitates. Minor proportions of  $\text{Al}_2\text{CuFe}$ ,  $(\text{Al}, \text{Cu})_6\text{Mn}$  and  $\text{Al}_2\text{Cu}$  are also present in the alloy [25].

### 2.2.2 Corrosion of AA2024

General corrosion for aluminium is rare and only experienced if the metal is exposed to highly acidic or alkaline media. Aluminium, although thermodynamically reactive, is often naturally oxidized in air and water, providing a thin passive film on the surface. This uniform oxide thin film is effective in preventing the underlying aluminium from corrosion, and is able to naturally reform on a freshly abraded surface, in the presence of oxygen. However, when

the protective layer is removed or damaged under conditions that the film is not able to repair, the breakdown usually initiates localized corrosion attack of the aluminium [26].

Due to the formation of IMPs in the AA2024 alloy matrix, the alloy is much more susceptible to localized corrosion attack than pure aluminium, especially in chloride containing aqueous environments. Pitting corrosion and intergranular corrosion are two major forms of localized corrosion on AA2024 alloy.

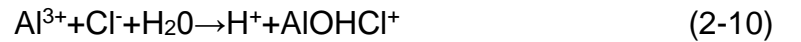
Pits are usually formed by two steps including initiation and propagation. The alloy matrix underneath the passive film is either aluminium or IMPs. When chloride ions attack passive film and cause breakdown in the area where aluminium is underneath, the dissolution of aluminium (equation (2-7)) will initiate pitting corrosion.



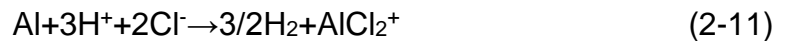
Simultaneously, cathodic reaction of oxygen reduction (in neutral or alkaline solution) (equation (2-8)) or hydrogen evolution (in acidic solution) (equation (2-9)) will take place.



Following this, the formation of  $\text{Al}^{3+}$  will attract  $\text{Cl}^-$  to migrate from the bulk solution into the pit solution. With the accumulation of  $\text{Al}^{3+}$  and  $\text{Cl}^-$  in pits,  $\text{H}^+$  is produced through the hydrolysis of  $\text{Al}^{3+}$  with the presence of  $\text{Cl}^-$  (equation (2-10)).



The production of  $\text{H}^+$  in pits then catalyses the dissolution of Al (equation (2-11)), leading to further propagation of pitting.



When chloride ions attack the oxide film and cause breakdown at IMPs on the alloy surface, the dissolution and dealloying of aluminium and magnesium (equation (2-7), (2-12)) in the anodic S-phase IMPs ( $\text{Al}_2\text{CuMg}$ ) will further initiate the formation of pits and releasing copper ions into solution [24, 27].



Simultaneously, a thin copper layer then redeposit on the surface and acts as a cathode supporting the cathodic reaction (equation (2-8), (2-9)) and coupling with surrounding aluminium pits to further propagate it [25, 27-29]. Schematic of localized pitting corrosion of AA2024 is shown in Fig 2.1.

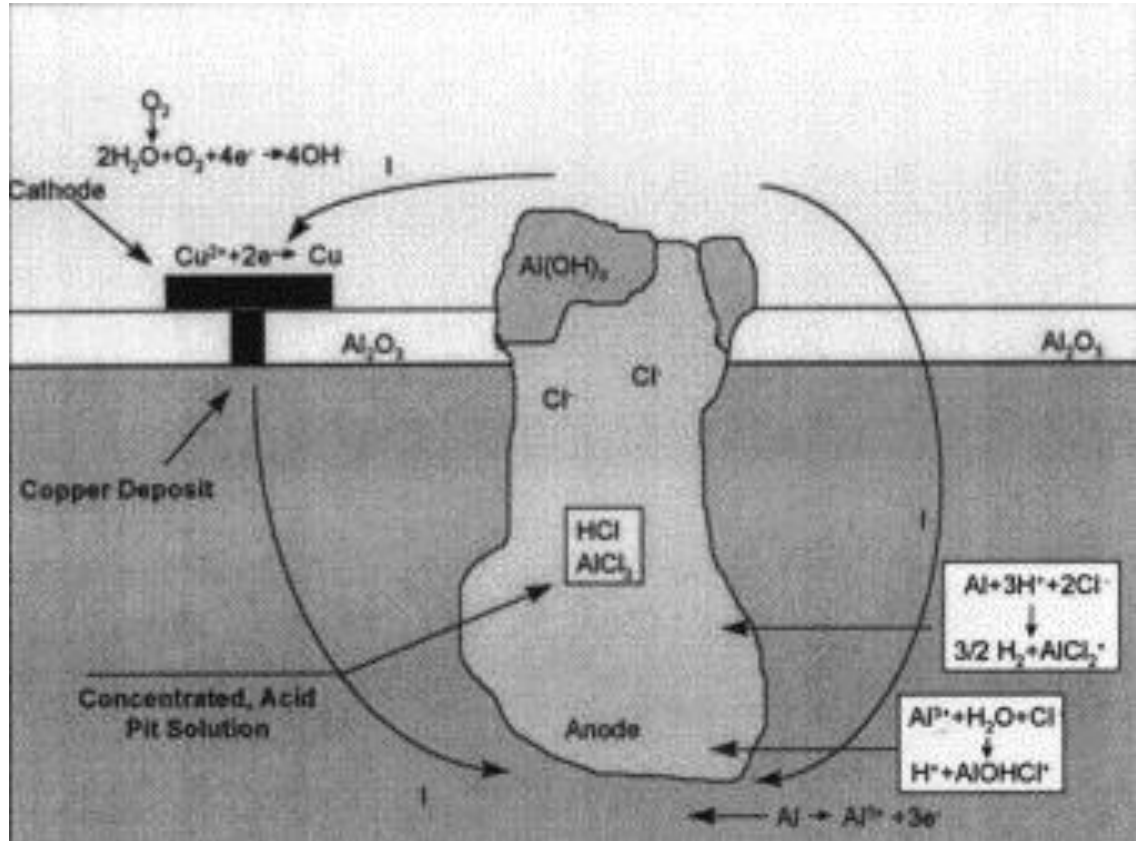


Fig 2.1 Schematic of localized pitting corrosion of AA2024 [30].

It is widely accepted that other second phase particles, mainly  $\text{Al}_6(\text{Cu, Fe, Mn})$ ,  $\text{Al}_2\text{CuFe}$ ,  $(\text{Al, Cu})_6\text{Mn}$  and  $\text{Al}_2\text{Cu}$ , with nobler elements, act as cathodic sites relative to the matrix, rather than a transformation of  $\text{Al}_2\text{CuMg}$  from anode to cathode, during immersion in chloride-containing electrolyte [23, 31, 32].

Since both pitting and intergranular corrosion stems from the local breakdown of the passive film on the surface, they seem to be similar in nature from an electrochemical point of view. However, pitting generally suffer from attack of IMPs or the grain in the alloy matrix, where intergranular corrosion is a result of attack at grain boundaries. Moreover, intergranular corrosion is regarded as a

special kind of pitting corrosion, when pits grow into the microstructure and develop into intergranular corrosion [33].

### 2.2.3 Corrosion protection of AA2024

As one of the most widely used aerospace alloys, the corrosion protection system of AA2024-T3 typically comprises of three individual layers when applied to aircraft structures (Fig 2.2) [30]. The first layer on the substrate is a thin (<10-60nm) inorganic conversion pre-treatment layer, which mainly provides enhanced adhesion between the substrate and the second layer of primer but also corrosion protection. The primer is mainly for corrosion protection function and made up of a pigmented organic resin matrix, which is relatively thick vary from 5 to 200µm. Finally, a top coat is applied as the third layer, whose principal function is to offer a barrier against environmental influence such as extreme climates and ultra-violet rays. Moreover, the topcoat is also used for decoration or camouflage of aircrafts.

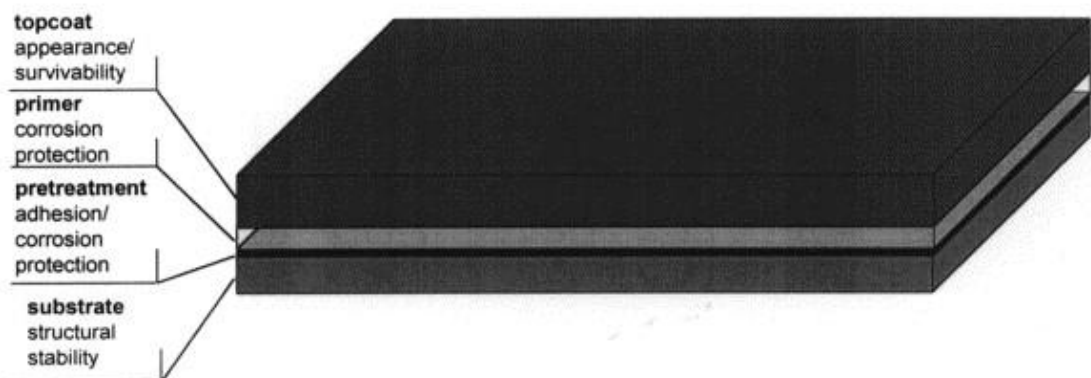


Fig 2.2 Schematic presentation of components that make up an aircraft coating system [30].

Since the advent of chromate inhibitor in the late 1970s, it has proved to be the most effective method for corrosion protection of aluminium alloys in pre-treatment layer and primer. However, due to its carcinogenic effects on humans and adverse effects on the environment, the application of chromium (VI) containing compounds has been gradually restricted by many countries.

To develop effective alternatives to chromate inhibitors, great efforts have been spent in the last decades. Promising alternatives could be generally classified into four types, including chromate replacement inhibitors, barrier coatings, conducting polymers and surface modification.

Numerous active inhibitors have found to be promising as chromate replacement inhibitors, such as rare-earth compounds [25], phosphates [34], organic inhibitors [35] or a combination of these [36]. With regards to barrier coatings; plasma deposition [37, 38], sol-gel coatings [39-41], self-priming topcoats [42] and electrodeposited coatings [43, 44] have been shown to be successful to a greater or lesser degree. Two major types of conducting polymers have been applied for the corrosion protection of AA2024 [45], i.e. polyaniline [46] and polypyrrole [47]. Differing from inhibitors, coatings and conducting polymers, surface modification creates a conversion layer on an aluminium surface by electrochemical anodization [48] or laser ablation [49] to improve adhesion or optimize the second phase particles on the surface.

It is also vital to note that more studies have been focused on a binary or ternary system from these alternatives. Wang & Akid, have reported a series of successful systems for corrosion protection of AA2024 alloy, including cerium nitrate inhibitors containing hybrid sol-gel system [39] and hybrid polyaniline/sol-gel coatings. Various nanostructured hybrid sol-gel coatings with organic and inorganic inhibitors have also been reported to provide active protection for AA2024 by Ferreira et al [50, 51]. Other studies on modified sol-gel coatings have also been reported by Thompson [52, 53] and Donley [54, 55].

Moreover, the majority of modified sol-gel coatings reported are not only anticorrosive and environmentally friendly but also offer self-repair functionality, which make the modified hybrid sol-gel coatings a promising candidate for the alternative to chromate-based inhibitors. The aim of this study also stems from the advantages of these newly developed hybrid sol-gel systems.

## 2.3 Sol-gel technology

The sol-gel process, which is initially employed in the preparation of inorganic materials such as glasses and ceramics, is a chemical synthesis method mainly based on inorganic polymerization reactions [56, 57]. More specifically, the sol-gel process is defined as the preparation of a sol, gelation of the sol, and removal of the solvent [58]. The sol-gel history dates back to the mid-1800s from Ebelman and Graham's discoveries [59] on the formation of "glass-like"  $\text{SiO}_2$  material from the hydrolysis of tetraethylorthosilicate (TEOS). However, little attention was paid at that time until a breakthrough was made by Roy and co-workers in 1950s. They synthesised many novel ceramic oxides using sol-gel process rather than traditional ceramic power methods [60]. It was after this breakthrough that the sol-gel process attracted a lot of attention from both the industry and academia. In the middle 1980s, hybrid organic/inorganic sol-gel materials were proposed and synthesised by Wilkes and Schmidt et al., which they termed as "ormosils" or "ceramer" [56]. Since then, sol-gel technology was extensively applied to prepare novel materials and further investigated in the field of ceramics, polymer chemistry, inorganic and organic chemistry and physics [61].

### 2.3.1 Introduction to sol-gel process

The sol-gel process, as the name implies, involves the terms of sol and gel. A sol is a stable suspension of colloidal solid particles within a liquid. A gel is a porous 3-D interconnected solid network that expands in a stable manner throughout a liquid medium and is only limited by the size of the container. The process here refers to gelation, during which a sol can be converted to a colloidal or polymeric gel by going through a gel-point [58, 62].

In a typical sol-gel process [63, 64], presented in Fig 2.3 (b), the first step is the formation of homogeneous solution of the precursor in a solvent. Then hydrolysis and polymerization will initiate the production of sol species, such as oligomers,



crosslinking chains and polymers, colloids. The sol is subsequently subjected to a series of condensation reactions. Once the solid gel is formed, the syneresis and aging processes keeps changing the chemical and physical properties of the gel.

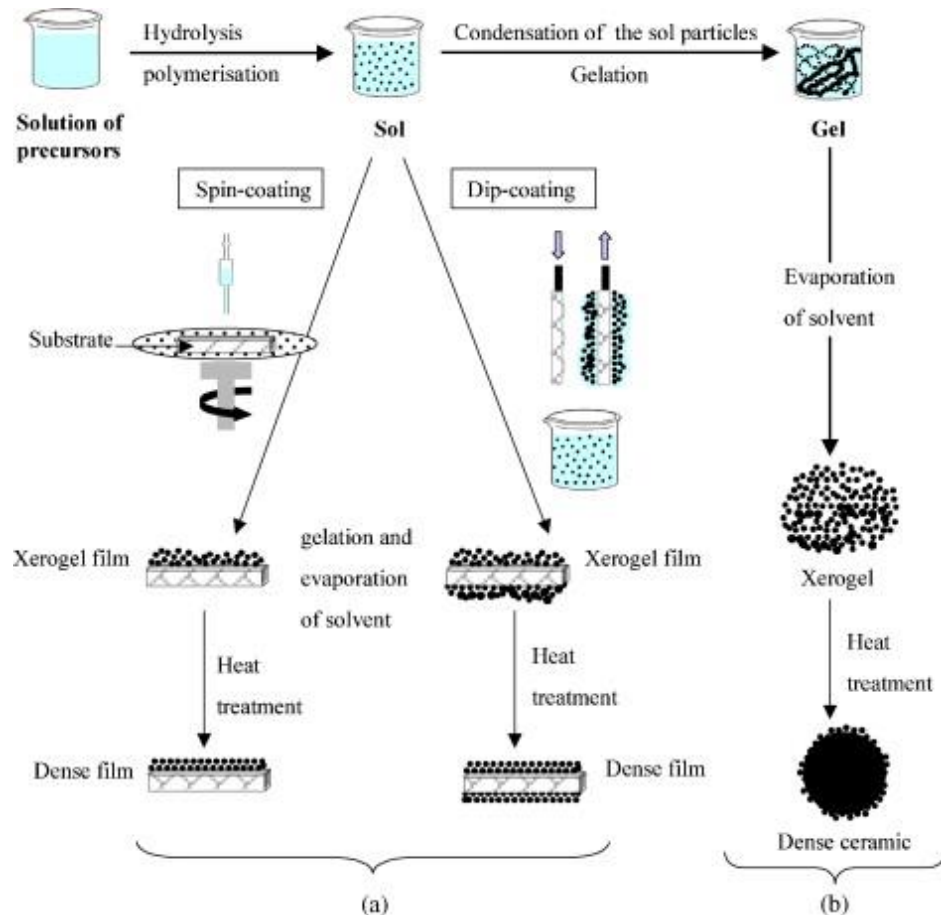


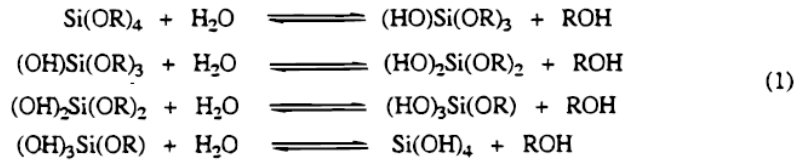
Fig 2.3 Overview showing two synthesis examples by the sol-gel method; (a) films from a colloidal sol; (b) powders from a colloidal sol transformed into a gel [64].

After further elimination of the solvent and drying, the dense solid xerogel of ceramic is obtained. It is a little different to deposit a sol-gel thin film on a substrate Fig 2.3 (a) from the production of dense ceramic. After the preparation of the sol, spin-coating or dip-coating may be applied to deposit prepared sol on the substrate. The deposited sol then undergoes gelation and evaporation of the solvent to produce the xerogel film, which is further heat-treated to obtain the final dense film.

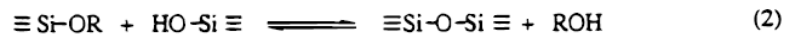
From a chemistry point of view, taking silicone alkoxide precursor as an example, chemical process of the sol-gel reaction may be represented as shown in Fig 2.4

[56]. The reaction typically follows two steps. The first step is the formation of hydroxyl groups on metal alkoxides by the hydrolysis reaction Fig 2.4 (1). Then, the polycondensation of hydroxyl groups and residual alkoxyl groups Fig 2.4 (2, 3) produce a three-dimensional network Fig 2.4 (4).

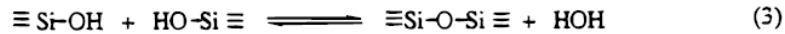
Hydrolysis



Alcohol Condensation (Alcoxolation)



Water Condensation (Oxolation)



Overall Reaction

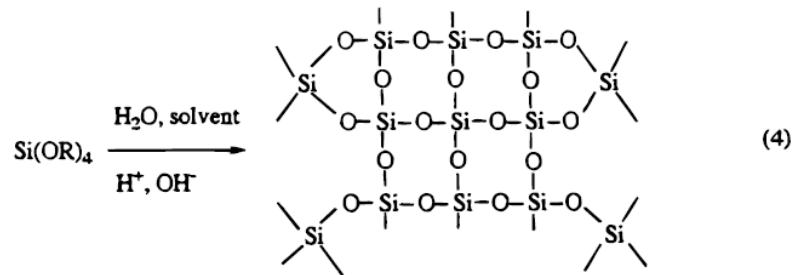


Fig 2.4 The general scheme of sol-gel process of silicon alkoxide precursor [56]. It is important to note that, hydrolysis and polycondensation reactions, in fact, occur simultaneously once the hydrolysis reaction has been initiated by the catalyst. Moreover, the small molecular by-products of alcohol and water during the reactions were then driven off from the 3-D network by drying. This will lead to shrinkage of the network, which may lead to the development of cracks in the thin sol-gel film. Essentially, the sol-gel process is comprehensively influenced by reaction parameters, including the nature of the precursor and solvent, pH of the catalysis water, precursor/solvent and precursor/water ratio, aging and drying conditions, temperature and ageing time [57]. Therefore, by controlling these process parameters, it is possible to produce a sol-gel material having a wide

range of functional properties. To date, sol-gel materials have provided successful solutions for many areas such as controlled release, inks and coatings, catalyst for fine chemicals production, nanocomposites, ceramic membranes, etc [65].

The fundamental advantage of the sol-gel technique is that it not only allows for the production of inorganic structures, but also the production of novel hybrid organic-inorganic material which does not naturally exist. It is also advantageous in producing excellent adhesion between the metallic substrate and the top coat as an intermediate bond-coating. Moreover, it is superior in preparing high purity products and materials with complex geometries. The relatively low temperature required and simple process makes this technology cost-effective for industries. However, the sol-gel materials also have some drawbacks limiting its applications, including poor wear-resistance, thickness limitation, substrate-dependent, shrinkage cracking and sensitivity to manufacturing conditions [62, 66].

### 2.3.2 Sol-gel coatings for corrosion protection

As described before, sol-gel condense thin films are able to provide excellent adhesion between the metallic substrate and the top coat, which act as an intermediate bonding-coating and hydrophobic barrier layer to water and vapour permeation as schematic illustrated in Fig 2.5.

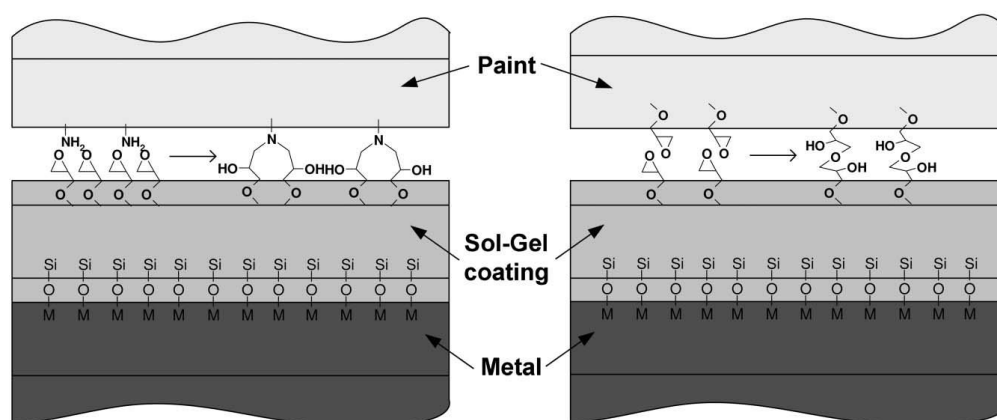


Fig 2.5 Schematic representation of enhanced compatibility of different paint systems with an epoxy-functional hybrid sol-gel coating [67].

The research of sol-gel coatings as substrate pre-treatment for corrosion protection of metals has expanded in the past decades. Various metallic substrates, including steel [68], aluminium [39], magnesium [69] and copper [70], have been effectively protected from corrosion using sol-gel coatings. Many oxide systems have been developed besides the most frequently used  $\text{SiO}_2$  [61, 67, 71-73], such as  $\text{ZrO}_2$  [74],  $\text{Al}_2\text{O}_3$  [75],  $\text{TiO}_2$  [76], and combined oxides [77-79]. However, there are some drawbacks of the pure metal oxide coatings. Firstly, crack free thick films ( $>1\mu\text{m}$ ) are difficult to achieve as they are brittle. Moreover, relatively high temperature ( $400\text{-}800^\circ\text{C}$ ) is required to achieve good properties [61].

Hybrid organic/inorganic sol-gel coatings were then developed to overcome the difficulties faced by pure inorganic oxide films. The introduction of organic components allows increased density, flexibility of the film and functional compatibility with organic paints, while retaining the advantages of scratch resistance, durability and adhesion, which are provided by inorganic components in the hybrid sol-gel coatings. With hybrid sol-gel, it is also possible to prepare thick crack-free coatings at low temperature [67, 80].

In the last decade, a great number of studies have been conducted on metallic corrosion protection by hybrid sol-gel coatings. Among these studies, the pursuit of hybrid sol-gel coatings as an alternative to chromate conversion coatings for corrosion protection of aluminium alloys have attracted a lot of attention.

### 2.3.3 Titania-containing hybrid inorganic/organic sol-gel coating

The standard titania-containing hybrid sol-gel applied in this study follows from the initial work of Ferreira et al. in 2006 and 2007 [79, 81, 82]. The nanostructured hybrid sol-gel system is based mainly on the hydrolysis and condensation of 3-glycidoxypropyltrimethoxysilane (GPTMS) and the in-situ synthesised titania

nanoparticles from the precursor of titanium isopropoxide (TIP). Their results showed that the hybrid sol-gel coating exhibits both good anticorrosive performance and excellent adhesion between the metallic substrate and the top paint.

Moreover, their work was further studied by Jiménez-Morales et al [83, 84]. They discovered that the molar ratio of Si/Ti has a great influence on the performance of the coating. Among the three different molar ratio studied, Si/Ti=4 has proven to be the optimal formulation with the best anticorrosive performance for an aluminium alloy. Compared with Si/Ti=2 and Si/Ti=8, the Si/Ti=4 sol-gel coating not only has the highest initial contact angle, most hydrophobic coating surface, but also it retains its hydrophobic properties, due to the lowest water uptake in the coating. The adhesion between the Si/Ti=4 sol-gel coatings and the metal substrate is also the strongest among the three ratios. EIS results and coating morphology after immersion in 3.5wt% NaCl solution indicate that the optimal sol-gel coating could better protect the aluminium substrate. Moreover, the best anticorrosive coating also has better mechanical properties such as hardness.

An explanation for the reason why the Si/Ti=4 ratio is better was attributed to the pore blocking effect from the titania nanoparticles in the polymeric network. For Si/Ti=8 sol-gel coatings, the ratio of titania nanoparticles is relative low and lead to a porous thin film. For Si/Ti=2 sol-gel coating, titania nanoparticles in the coating is excessive and too high for the polymeric network. Although the sol-gel coating prepared from this formulation is dense, the pore blocking by titania nanoparticles is uniform, leading to excessive blocking in some areas, where other areas remain porous. However, the corrosion protection performance of the Si/Ti=2 sol-gel coating is somewhat similar to that of the Si/Ti=4 sol-gel coating than the porous one of Si/Ti=8.

## 2.4 Conducting polymers

### 2.4.1 Introduction to conducting polymers

Materials can be classified into four types according to electrical properties, including insulator, semiconductor, conductor and superconductor. Insulators have the lowest conductivity of less than  $10^{-7}$  S/cm and the conductivity of a metal is usually higher than  $10^3$  S/cm. Generally, a material with a conductivity between  $10^{-7}$  S/cm and  $10^3$  S/cm is regarded as semiconductor.

Semiconductor can be divided into two types; namely inorganic semiconductor and organic semiconductor. The small energy gap for the movement of electrons within semiconductors from valence band to the higher energy of conduction band is the key to the conductivity of semiconductors. Differences of energy gap in insulator, semiconductor and conductor are presented in Fig 2.6.

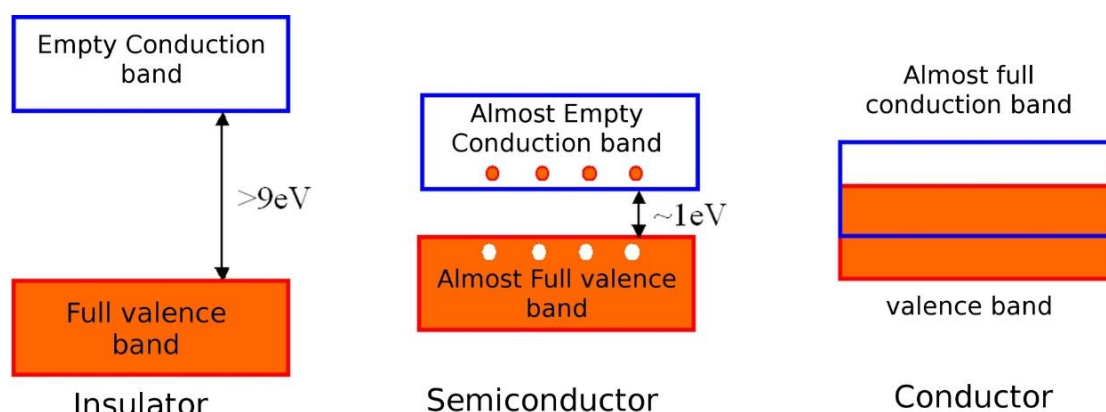


Fig 2.6 Representation of energy bands in insulator, semiconductor and conductor [85]

Polymers have long been considered to be insulators due to the large energy gap between the two bands. However, the discovery of conductive iodine doped polyacetylene (PA) opened a new field of conducting polymers [86]. The breakthrough was mainly made by three leading scientists, Heeger, MacDiarmid and Shirakawa in 1977 and their creative work was later awarded the Chemistry Nobel Prize in 2000. Completely different from the traditional conducting polymers, which were produced by merely physically mixing conducting materials of metals or carbon powders with nonconductive polymers, the novel conducting

polymers they developed are more specifically termed as “intrinsically conducting polymers” (ICPs) or “synthetic metal” [87]. While retaining the mechanical properties, easy processing and other properties of a conventional polymer, ICPs can also possess electrical, electronic, magnetic and optical properties of metals. In the discovery and development of ICPs, controlled conductivity stems from the concept of doping. By changing the degree of doping, the conductivity of ICPs can almost cover the whole region of insulator-semiconductor-metal as presented in Fig 2.7. Taking trans-(CH)<sub>x</sub> and emeraldine polyaniline for example, the doped forms of both could obtain a conductivity resembling that of a metals, where undoped forms of trans-(CH)<sub>x</sub> is similar to Si and polyaniline have conductivity values close to glass, see Fig 2.8.

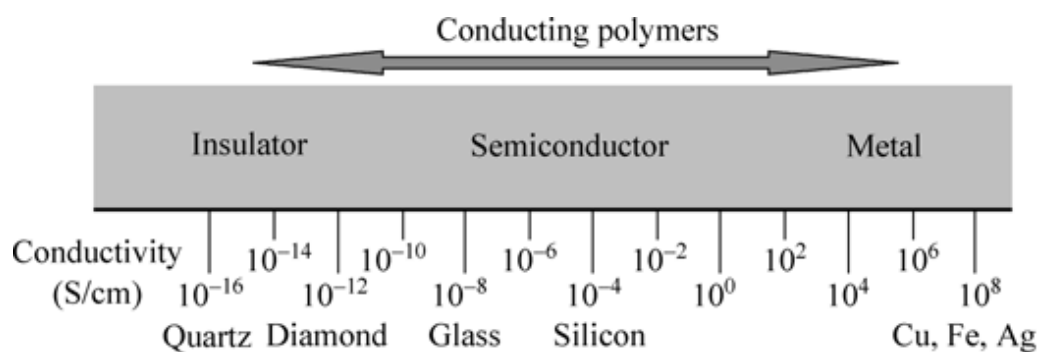


Fig 2.7 Conductivity range of ICPs varies from doping degree [88].

It is important to emphasize that doping in ICPs differs significantly from traditional inorganic semiconductor [88]. Firstly, p-type doping and n-type doping in ICPs are oxidation or reduction processes, rather than atom replacements in inorganic semiconductors. Secondly, doping in ICPs can be acquired and maintained with the incorporation of a counter ion. Thirdly, doping and de-doping in ICPs can be easily processed by chemical or electrochemical methods. Finally, the degree of doping in ICPs can be as high as 50%, where it is very low (1%) in inorganic semiconductors.

Conductivity increases with increased doping

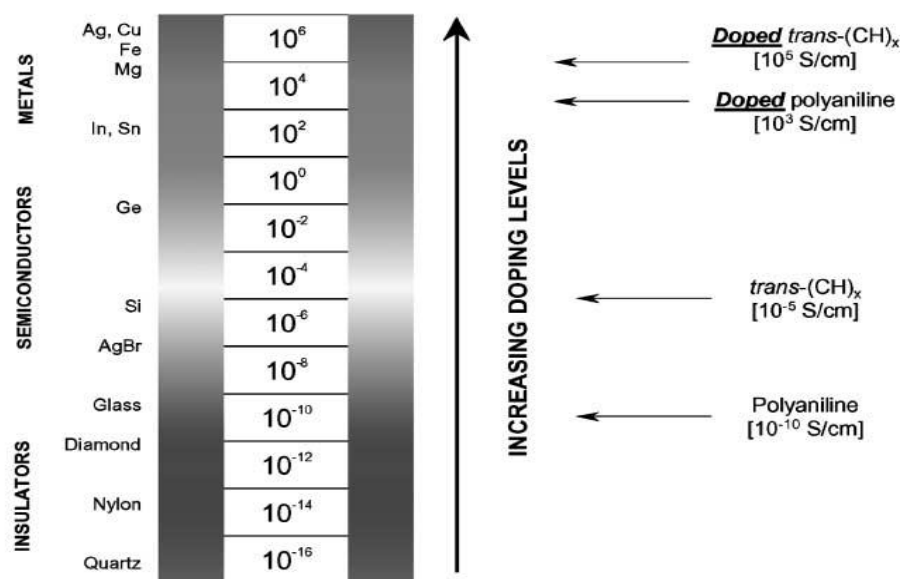


Fig 2.8 Conductivity of doped and undoped  $\text{trans}-(\text{CH})_x$  and emeraldine polyaniline [89].

## 2.4.2 Introduction to polyaniline

Since the breakthrough on ICPs made by MacDiarmid et al in 1977, a great amount of ICPs have been discovered, synthesised and applied. The molecular structures of typical ICPs are presented in Fig 2.9. It is evident that  $\pi$ -conjugated chains on the polymer backbone is a shared feature in ICPs.

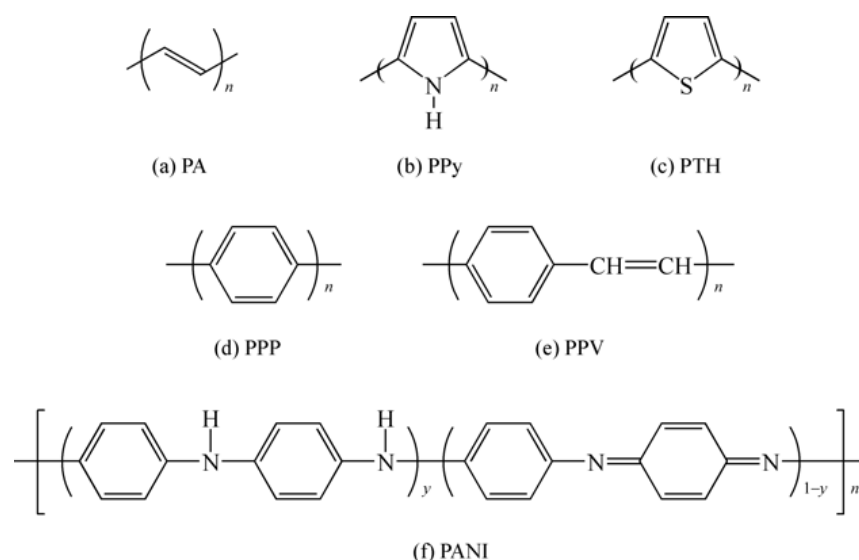


Fig 2.9 Molecular structure of typical ICPs.

(a) trans-polyacetylene (PA); (b) polythiophenes (PPy); (c) poly(p-phenylene) (PTH); (d) polypyrrole (PPP); (e) poly(p-phenylenevinylene) (PPV); (f) poly(2,5-thienylenevinylene) (PANI) [90].



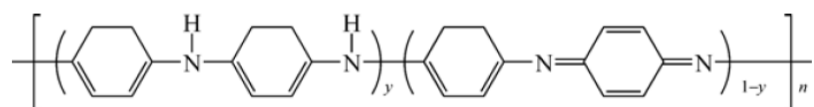
Among the various ICPs, polyaniline (PANI) is one of the most promising, due to the advantages of easy synthesis, low cost of raw materials, environmental stability and controllable physical properties via different oxidation and proton doping states. Moreover, PANI has many potential application in the area of energy transformers, optical information storage, non-linear optics, membranes, corrosion protection etc.

Although, polyaniline was first electrochemically synthesised in 1862 [91], which is now recognized as “aniline black”, the electrical properties indicating the nature of ICPs was not studied at that time. It was for the first time in 1985 [92] that MacDiarmid synthesised the green power of PANI with a conductivity of 3S/cm via chemical oxidation of aniline monomer by ammonium peroxydisulphate (APS) in acid aqueous solution. The protonic doping enabled the emeraldine oxidation state of PANI convert from undoped “insulator” of emeraldine base (EB) form ( $\sigma \sim 10^{-10}$  S/cm) to a doped “metal” of emeraldine salt (ES) form ( $\sigma \sim 5$  S/cm) of emeraldine hydrochloride by treatment with 1M aqueous HCl solution [93, 94].

The widely accepted chemical structure of PANI was proposed by MacDiarmid in 1987 [93]. He suggested a model of PANI composed of both the reduced repeat

units of  and oxidized repeat units of .

The general formula for a series of PANI in the base form is



In this formula,  $y$  is the oxidation-reduction degree in PANI and  $0 < y < 1$ . When  $y=0$ , PANI is in fully oxidized state of pernigraniline base (PNB). The fully reduced state of leucoemeraldine base (LB) corresponds to a value of  $y=1$ . The half oxidized or half reduced state of emeraldine base (EB) has a value of  $y=0.5$ . PNB, LB and EB are three oxidation states of PANI and their relationship is explained in Fig 2.10. In the form of EB, PANI could turn to electrically conducting from of

emeraldine salt (ES) after doping with an acid and return to the insulated form of EB by dedoping with alkaline solution.

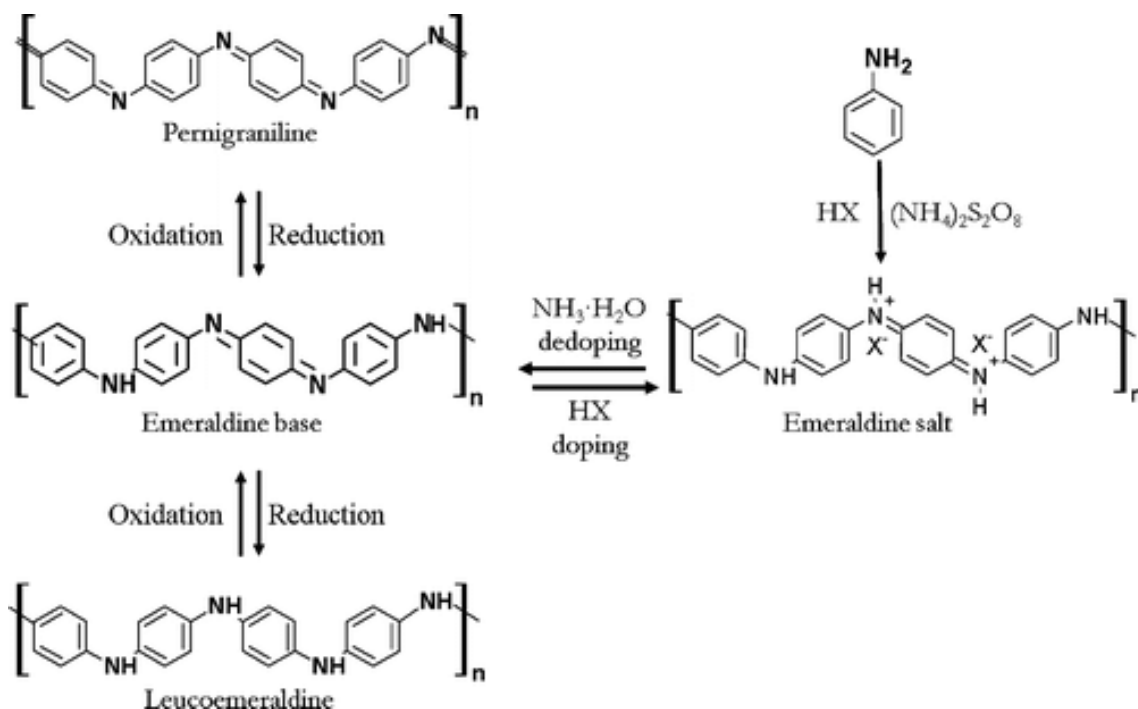


Fig 2.10 Schematic diagram showing the molecular structure, synthesis chemistry, reversible acid/base doping/dedoping, and redox chemistry of PANI [95].

### 2.4.3 Synthesis of polyaniline

In terms of PANI synthesis, various methods have been demonstrated to be successful, including chemical [96-112], electrochemical [113-115], mechanochemical [116], template [117-120], enzymatic [121-123], plasma [124, 125] and photo [126, 127], etc. Chemical polymerization could be further subdivided into heterophase [96, 97], solution [98, 99], interfacial [100-102], rapid-mixing [103, 104], seeding [105, 106], metathesis [107], self-assembling [108-110] and sonochemical [111, 112] polymerizations.

Due to the advantages of simple synthesis, low cost of raw materials, mild reaction conditions and high yield, chemical synthesis of PANI is ideal for industries. The synthesis is generally performed by chemical oxidation polymerization. Aniline monomer in aqueous strong doping acid solution (e.g. 1M HCl) was oxidized by a suitable oxidant (e.g. ammonium peroxodisulphate (APS)).

The reaction is mainly influenced by the concentration of monomer, type and concentration of both the oxidant and doping acid, temperature and reaction time, along with other solution treatment methods. Among all these factors, the oxidant and doping acid are the most important and widely investigated by researchers. There is a wide range of oxidants available and demonstrated to be successful in the chemical synthesis of PANI [128]. APS and Fe(III) compounds are the two vital and most frequently used oxidizers. Various other oxidants were also developed, including transition metal compounds (Mn(III), Mn(IV), Mn(VII), Cr(VI), Ce(IV), V(V), Cu(II)), noble metal compounds (Au(III), Pt(IV), Pd(II), Ag(I)) and KIO<sub>3</sub>, H<sub>2</sub>O<sub>2</sub>, benzoyl peroxide or mixtures of oxidants (e.g. FeCl<sub>3</sub>/H<sub>2</sub>O<sub>2</sub> and KIO<sub>3</sub>/NaClO). Doping acid also has abundant choices from traditional mineral acid (hydrochloric, sulphuric, nitric, perchloric or phosphoric, etc.) and organic acid (formic, acetic, camphorsulphonic, methylsulphonic, 4-toluene-sulphonic, ethylsulphonic, tartaric, etc.).

Due to the oxidising power and high yield of APS, it is regarded as an optimal oxidant for the chemical synthesis of PANI. Taking APS as the oxidant, chemical polymerization synthesis reaction of PANI ES is briefly given in Fig 2.11 [129]. The final product of chemical oxidation of aniline by APS in strong acidic medium is PANI in green doped emeraldine salt form and by-products of sulphuric acid and ammonium sulphate. It is clear that the final products are produced after the formation of an intermediate of blue protonated PNB. Although, the process for the formation of PANI ES is complicated and various mechanisms were proposed, the formation of fully oxidized blue PNB intermediate is widely accepted. Moreover, the stoichiometric monomer/oxidant ratio, obvious from the reaction, is 0.8, which was found in 1996 by Stejskal et al [130].

However, it does not need to exactly follow this ratio when using APS to prepare PANI. Some synthesis of different PANI nanostructures may require special ratio or oxidant to achieve the goal. In Fig 2.12, some very interesting PANI nanostructures were synthesized using various oxidants, ratios and conditions.

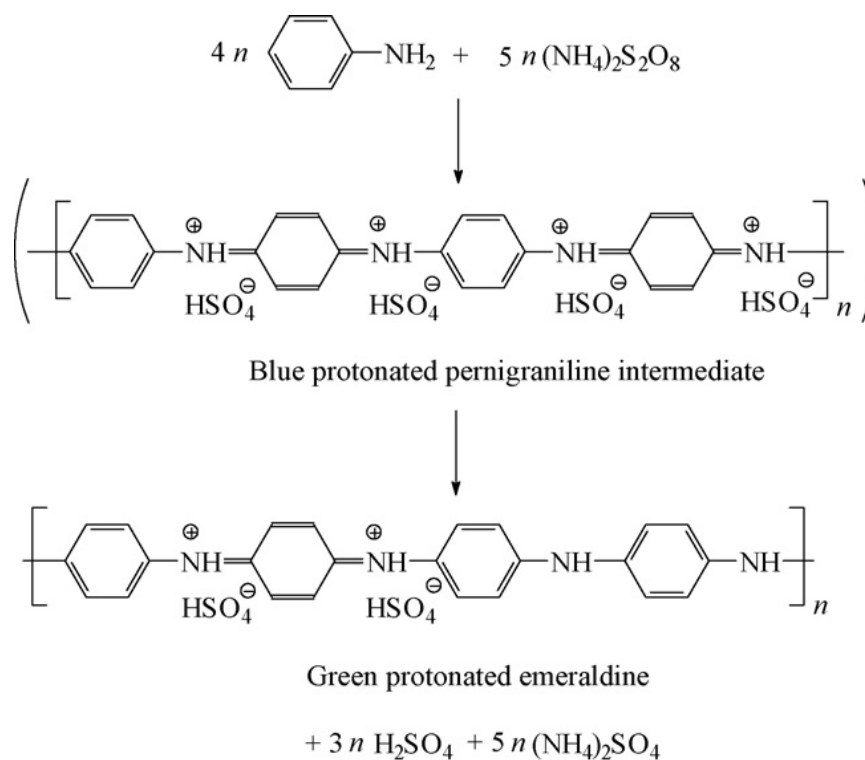


Fig 2.11 Overall reaction of chemical oxidation synthesis of PANI ES [129].

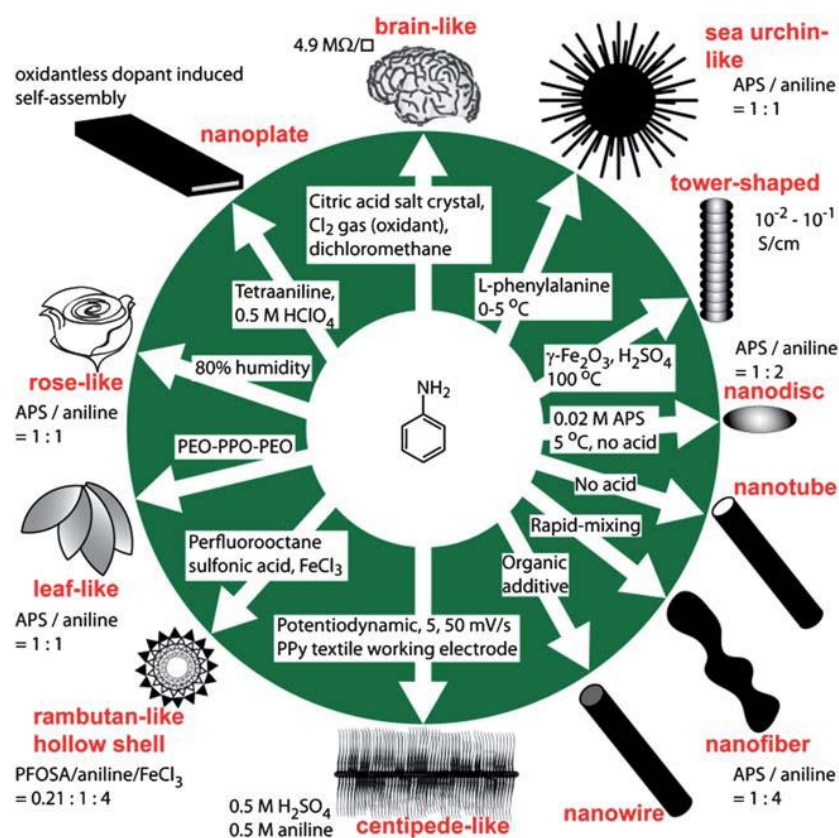


Fig 2.12 Synthesis of different nanostructured PANI from various synthetic conditions [131].

#### 2.4.3.1 Synthesis of polyaniline nanofibers

Developed by Kaner's group in UCLA [103], rapid-mixing method of synthesis PANI nanofibers is advantageous in robust reaction conditions, uniform size of pure nanofibers and simple process. The preparation procedures are briefly described as below. Firstly, 3.2mmol aniline (ANI) was dissolved in 10ml 1M HCl to obtain the monomer solution. 0.8mmol APS was dissolved in 10ml of the same doping acid to form the initiator solution. Secondly, the initiator solution was poured into the monomer solution all at once, followed by 30s of stirring with a magnetic stirrer to ensure sufficient mixing. Finally, the mixed solution was then left still at room temperature for two hours and green power of PANI ES nanofiber was then obtained after filtration or centrifugation and drying.

In this method, the key for producing nanofiber is the prevention of secondary growth of PANI. As all the reactants are evenly distributed and simultaneously consumed during the formation of PANI nanofibres, no extra reactants are available for further reaction on fresh formed PANI nanofibers to produce aggregates. In other words, PANI nanofibers form and grow by homogeneous nucleation.

Knowledge of suppressing secondary growth of PANI stems from their initially developed method of interfacial polymerization, where the formation of PANI nanofiber occurs just at the interface between the organic phase of aniline solution and the aqueous solution of APS. A schematic illustration of both the rapid-mixing method and interfacial polymerization are presented in Fig 2.13 and Fig 2.14. Moreover, to prepare PANI nanofibers, stirring is not preferred during the polymerization, due to the initiation of secondary growth on PANI nanofibers with the application of stirring, as illustrated in Fig 2.15. The aim in preventing stirring also means stopping heterogeneous nucleation growth of PANI on freshly formed PANI nanofibers.

In terms of the doping acid, they also found that in both the rapid-mixing method and interfacial polymerization, pure and uniform PANI nanofibers could all

obtained in HCl, H<sub>2</sub>SO<sub>4</sub>, HNO<sub>3</sub> and HClO<sub>4</sub>. SEM images of PANI nanofibres synthesised in different doping acid are presented in Fig 2.16.

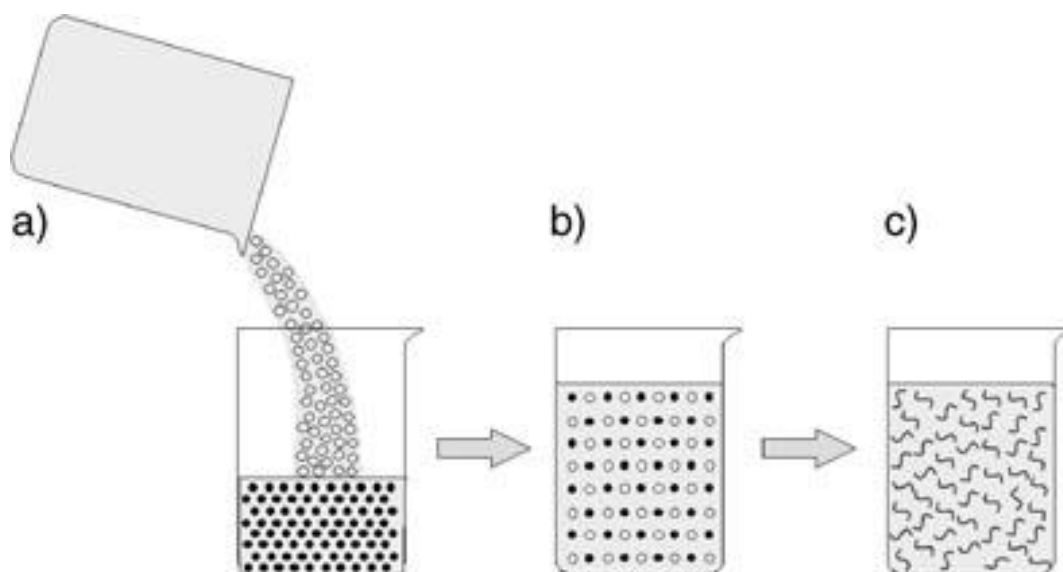


Fig 2.13 Schematic illustration of the synthesis of polyaniline nanofibers by a rapidly mixed reaction [132].

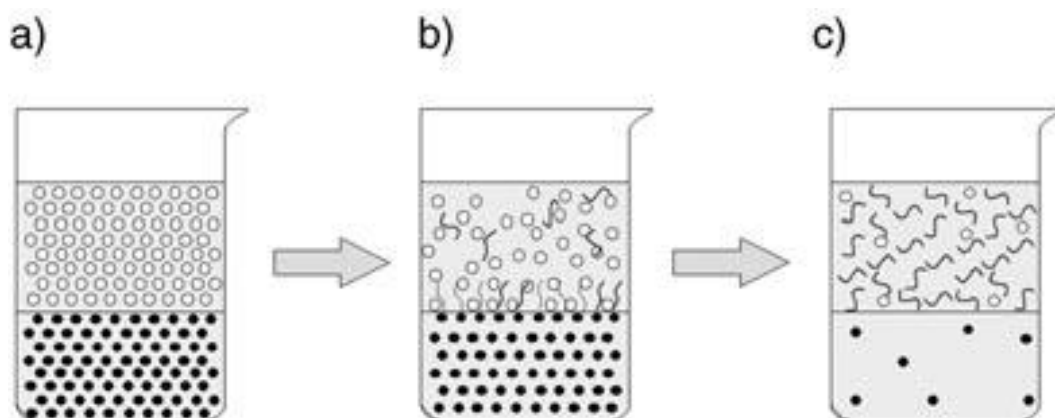


Fig 2.14 Schematic illustration of the synthesis of polyaniline nanofibers using interfacial polymerization [132].

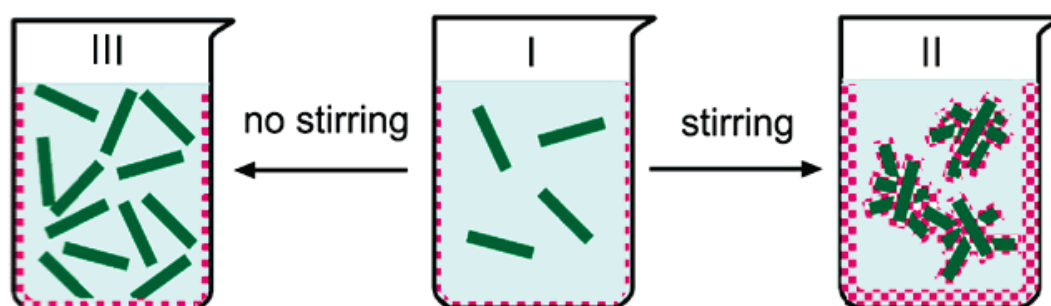


Fig 2.15 Schematic illustrations of the formation and aggregation of polyaniline particles. The green fibers and purple dots represent polyaniline particles that result from homogeneous and heterogeneous nucleation, respectively [133].

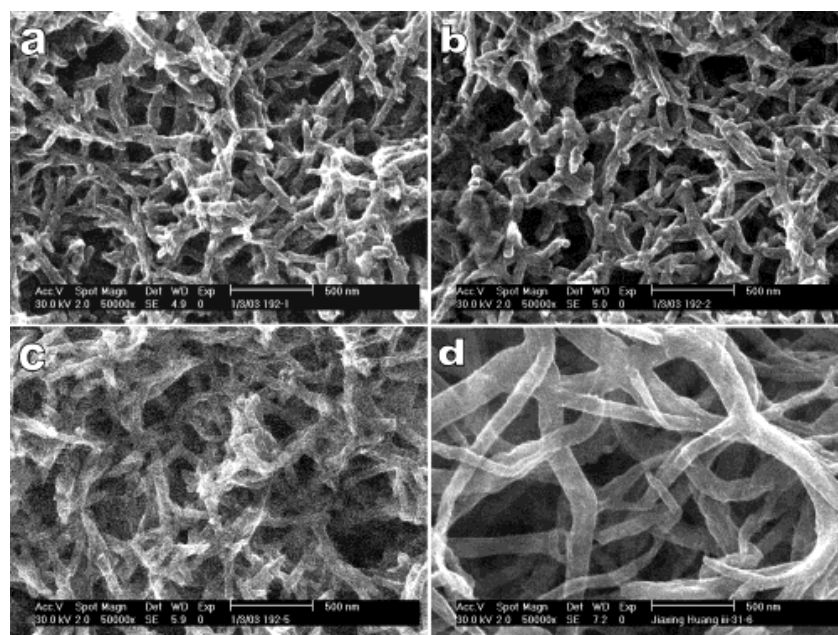


Fig 2.16 SEM images of PANI nanofibers made with following dopant acid in interfacial polymerization: (a) HCl, (b) H<sub>2</sub>SO<sub>4</sub>, (c) HNO<sub>3</sub>, and (d) HClO<sub>4</sub> [102].

#### 2.4.3.2 Synthesis of polyaniline agglomerated particles

In traditional chemical synthesis, the initiator solution is added slowly into the monomer solution by titration or syringe-pumping. As the fresh produced PANI was exposed to aniline monomers and the doping acid, secondary growth of PANI in this situation is severe, which leads to the formation of agglomerates of PANI nanoparticles. Fig 2.17 briefly illustrate the formation of PANI agglomerated particles during conventional chemical synthesis.

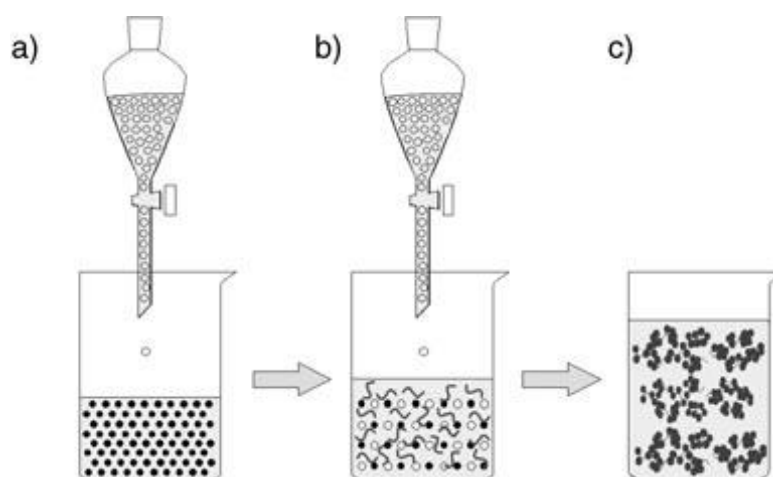


Fig 2.17 Schematic diagram illustrating the formation of PANI agglomerates during conventional chemical synthesis [103].

## 2.4.4 Corrosion protection by polyaniline

The earliest work on corrosion protection by PANI was conducted by DeBerry in 1985 [134]. He confirmed that the deposition of PANI on stainless steel would initiate the formation of a passivation layer on the substrate to provide anodic protection [135].

For aluminium alloys, the first report on the corrosion protection by PANI was published by Racicot et al in 1997 [136]. He also found evidence of the formation of a passivation layer between the substrate surface and the double-strand PANI layer. Moreover, the EB and ES form of PANI were also studied by Epstein for the corrosion protection of AA2024 [137]. His results revealed that both the two forms of PANI have similar corrosion protection properties for AA2024.

The formation of the passivation layer initiated by PANI on both the surface of steels and aluminium alloys may be attributed to the redox-active nature of PANI. Moreover, the half oxidized EB form of PANI is able to be recovered by oxidation from the reduced LB form of PANI, which was produced from the corresponding process of metal passivation [138]. The mechanism is schematically presented as below in Fig 2.18.

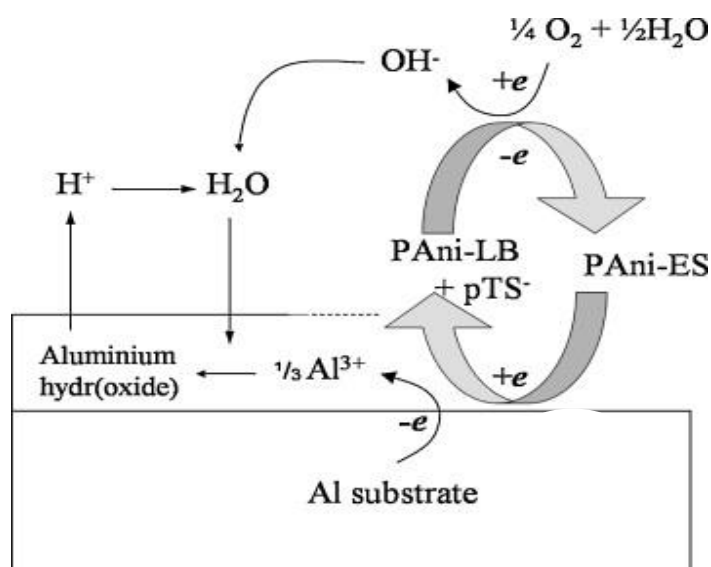


Fig 2.18 Mechanism of PANI corrosion protection on aluminium [139].

Besides bare PANI thin films for corrosion protection of aluminium alloy, various advanced PANI containing anticorrosive coatings have been developed as well.



Enhanced corrosion protection performance could be obtained by the addition of PANI in these successful systems, including PANI/epoxy coatings [140, 141], PANI/sol-gel coatings [142], PANI/co-polymer coating [139, 143], etc.

In this study, PANI ES was added into the hybrid titania-containing sol-gel system. PANI modified hybrid sol-gel coatings were then deposited on the AA2024 substrate to study the corrosion protection properties.

## 2.5 Glass flake

### 2.5.1 Introduction to glass flake

Glass flakes were developed from the U.S.A in the late 1950s. They were initially used to reinforce polyester roof-light panels. It was later in the 1960s that glass flake found its way into the coating industry sector especially due to their high aspect ratio. Nowadays, advanced nano glass flakes have also been developed with extremely high aspect ratio as presented in Fig 2.19.

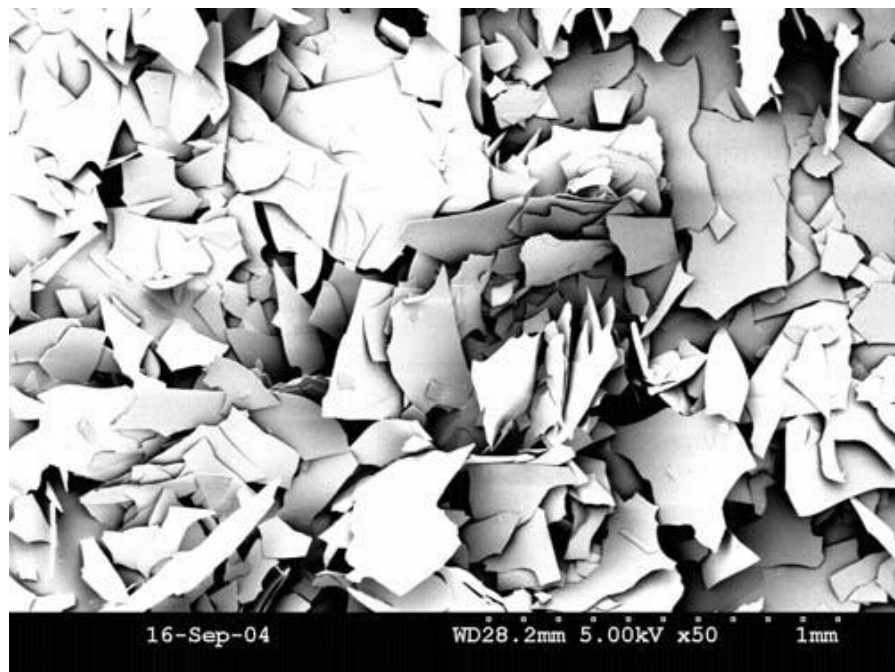


Fig 2.19 SEM images of advanced nano glass flake [144].

For the industrial application of three-coat corrosion protection system, which comprised of sacrificial primer, intermediate coat and top coat, it is well known that the porous nature of organic films has poor permeability to moisture vapour

and other corrosive species. Therefore the corrosion resistant glass flakes with high aspect ratio were considered as a good filler to reduce the permeation of the coating. Overlapped glass flakes could act as efficient barrier to the permeation of moisture and gas diffusion in the film. The tortuous path effect (Fig 2.20) could explain the effect of how glass flakes extend the diffusive path length [144]. Compared with other barrier pigments such as micaceous iron oxide, glass flake has many advantages including clear colour, high chemical resistance, good mechanical properties and is non-hazardous to humans and the environment.



Fig 2.20 The tortuous path effect [144].

## 2.5.2 Corrosion protection by glass flake

Since the late 1980s, glass flakes containing organic coatings have become more and more acceptable due to the apparent long life performance. The epoxy resin organic coating system is the dominant matrix for glass flake application in corrosion protection of carbon steel. Many researchers find that suitable addition of glass flakes could improve not only the corrosion resistance and the service life of the coating, but also the mechanical properties such as dimensional stability, surface hardness, wear resistance, tensile and flexural stiffness [145-147]. The morphology, rheology, thermal, viscoelastic properties and mixing methods [145, 148] of glass flake/epoxy resin coatings have also been studied in recent years. Moreover, the system has been successfully adopted in the oil and gas sector for the corrosion protection of pipelines. It is also important to note that

surface modified glass flake by silane or polyaniline, compared with bare glass flakes, have been shown to provide excellent corrosion protection performance for epoxy resin coatings due to better bonding properties of glass flakes in the polymeric matrix [147, 149].

However, until now, all the studies for the corrosion protection of glass flake containing organic coatings are epoxy resin systems and the substrate based is just carbon steel. To the authors knowledge, sol-gel coatings, incorporating glass flake for the corrosion protection of aluminium alloys, has never been reported before. In this study, glass flake were added in the hybrid titania-containing sol-gel systems and applied to the AA2024. The corrosion protection of the coating systems were then assessed.

# Chapter 3 Experimental work

## 3.1 Preparation of samples

### 3.1.1 Cleaning of AA2024 substrate

The metal substrate was bare AA2024-T3 aluminium alloy supplied by Wilsons metals, UK (thickness is 2.0mm) and Q-Lab, UK (thickness is 1.6mm). Chemical composition of the QQ-A-250/4 AA2024-T3 alloy is listed in the Table 3.1. Before applying the coating, three methods were used to clean the substrate respectively, including acetone cleaning, acid desmutting and alkaline etching of AA2024 samples [150].

Cu	Mg	Mn	Si	Fe	Zn	Ti+Zr	Ti	Cr	Others	Al
3.80-4.90	1.20-1.80	0.30-0.90	0.5	0.5	0.25	0.2	0.15	0.1	0.15	Balance

Table 3.1 Percent chemical composition of AA2024-T3 aluminium [151, 152].

(All values shown are % maximum unless shown as a range)

AA2024 coupons were ultrasonically cleaned in acetone, rinsed with deionized water and dried with a fan heater. These samples were denoted as ‘as-received AA2024’ (AR 2024) samples and were kept in a desiccator prior to use.

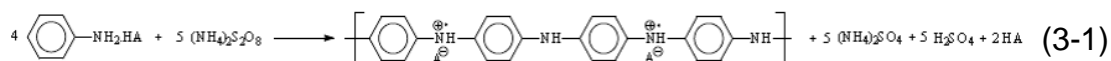
Acid desmuted samples, denoted (AD2024) were prepared by immersing in 30% (v/v) nitric acid ( $\text{HNO}_3$ ) at room temperature for 7.5 minutes, washed in deionized water and rinsed in acetone to dry the sample.

Alkaline etched samples, denoted (AE2024) were prepared by conventional etching in 10wt% sodium hydroxide ( $\text{NaOH}$ ) solution for 30s at 60 °C and desmutting in 50% (v/v)  $\text{HNO}_3$  for 30s at room temperature. Samples were then rinsed with deionized water and dried with a fan heater. AE2024 samples were also kept in a desiccator prior to use.

### 3.1.2 Synthesis of polyaniline

Polyaniline (PANI) was chemically synthesised via oxidative polymerization of aniline in aqueous 1M  $\text{HNO}_3$  using ammonium persulphate (APS) as oxidising

agent. Two different forms of nanostructured PANI were obtained using different preparation methods. PANI nanofibres were synthesised via rapid-mixing reaction [103] and agglomerates of PANI particles were prepared through traditional polymerization reaction [153]. The overall reaction may be described as shown in equation (3-1), based on the work of J. Stejskal et al [130].



Prior to the rapid-mixing reaction, monomer aqueous solution was prepared by dissolving 3.2 mmol aniline in 10ml 1M doping agent of HNO<sub>3</sub> and 0.8 mmol of APS (NH<sub>4</sub>)<sub>2</sub>S<sub>2</sub>O<sub>8</sub> was also dissolved in 10ml 1 M HNO<sub>3</sub> to form the aqueous oxidising solution.

Rapid polymerization of aniline was then initiated by pouring the oxidising solution into the monomer solution in one batch, followed by stirring with a magnetic stirrer for 30s and then left unstirred in a room temperature water bath for two hours. The collection of HNO<sub>3</sub> doped polyaniline emeraldine salt (PANI ES) nanofibres was then conducted by traditional vacuum filtration. The filter cake was washed with 1M HNO<sub>3</sub> to replace the H<sub>2</sub>SO<sub>4</sub> doped PANI by-products during the reaction. Then ethanol (absolute) was used to wash away any remaining small monomers or other organic molecules. Finally, the cake was washed with deionized water to remove residual acid until the filtrate reached a clear colour and neutral pH. The filter cake was dried in an oven at 60°C for 48 hours and a green powder of HNO<sub>3</sub>-doped PANI ES nanofibres was obtained.

During the traditional polymerization synthesis of agglomerated PANI particles, the same concentration of both the monomer solution and the oxidiser solution was used as that of rapid-mixing reaction. However, 100ml of oxidising solution was added drop wise into 100ml monomer solution using a cylindrical funnel over a period of 30 mins. The solution was continually stirred during the reaction for 2 hours at room temperature in a water bath. After the reaction was complete, the

same procedures of filtration and drying, as used for preparing nanofibres, were applied to generate the HNO<sub>3</sub>-doped agglomerates of PANI particles.

Blue PANI EB powers were obtained by dedoping the green PANI ES powders in 1M NH<sub>4</sub>OH overnight following by filtration and drying.

### 3.1.3 Preparation of sol-gel coatings

#### 3.1.3.1 Synthesis of standard sol-gel

Original work on preparation of the hybrid titania containing sol was reported elsewhere [79, 83], however for fullness, details of the synthesis is provided below.

The main procedure of the hybrid sol was obtained by two alcosols, which were formed by dispersing solid components in alcohols. The first alcosol was prepared by the hydrolysis of silane precursors. 5.2ml 3-glycidoxypropylmethyl-diethoxysilane (GPTMS/C<sub>9</sub>H<sub>20</sub>O<sub>5</sub>Si) and 1.3ml vinyltriethoxysilane (VTES/H<sub>2</sub>C=C-HSi(OC<sub>2</sub>H<sub>5</sub>)<sub>3</sub>) was mixed in 6.5ml absolute isopropanol (i-PrOH/(CH<sub>3</sub>)<sub>2</sub>CHOH). Then 1.6ml acidified water of pH 1 HNO<sub>3</sub> was added into the silane precursors to catalyse the hydrolysis process. Mechanically magnetic agitation was then applied during the hydrolysis for 1 hour. The second alcosol with in-situ formed titania nanoparticles was prepared by controlled hydrolysis of 2.12 ml titanium isopropoxide (TIP/Ti{OCH(CH<sub>3</sub>)<sub>2</sub>}<sub>4</sub>) in the 2.12 ml isopropanol. Ethyl acetoacetate (AcEt/CH<sub>3</sub>COCH<sub>2</sub>COOC<sub>2</sub>H<sub>5</sub>) (2.12ml) was also added as a complexing agent to reduce the reactivity of the metallic alkoxides of TIP. After the mixture was sealed at room temperature for 20 mins to form the titanium (IV) coordination complex, 0.53ml acidified water of pH 1 HNO<sub>3</sub> was added into the mixture under magnetic stirring for another 20 mins to synthesise the titania nanoparticles containing alcosol. Finally, the second alcosol was added drop wise into the first alcosol under magnetic stirring for 1 hour. The hybrid sol system was then aged at room temperature for 24 hours before being deposited on the AA2024 substrates. The

hybrid titania-containing sol-gel prepared from this method was termed as the 'standard sol-gel' in this study.

### 3.1.3.2 Synthesis of PVB modified sol-gel

In order to increase the cross-linking properties and viscosity of the hybrid sol, a co-polymer or binder, commercial Mowital B 60 H polyvinyl butyral (PVB) from Kuraray Europe GMBH, was added into the sol-gel system. The chemical formula of the PVB is presented in Fig 3.1.

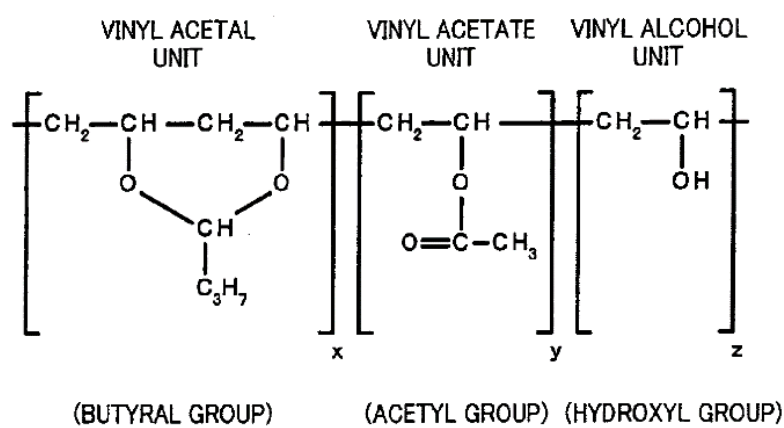


Fig 3.1 Chemical formula of the PVB [154].

Before the synthesis of PVB modified sol-gel, Mowital B 60 H polyvinyl butyral, the fine powder was firstly dissolved in ethanol to form a 10wt% solution. Magnetic stirring and ultrasonically agitation was applied to the solution until the PVB powder was completely dissolved in ethanol and a transparent solution without any bubbles was obtained. Three different PVB/hybrid sols were prepared by adding, individually, 2.5ml, 5.0ml and 10.0ml of PVB solution drop wise into the as synthesised hybrid sol just before the aging stage. These sol-gels were termed as SG\_PVB\_8, SG\_PVB\_4 and SG\_PVB\_2, respectively.

### 3.1.3.3 Synthesis of PANI modified PVB sol-gel

The synthesised PANI ES nanofibres, agglomerated particles and commercial PANI ES on carbon black were solution blended before added into the PVB sol-gel. The solution blending strategies applied involved the preparation of 2wt%

PANI ES dispersions in the traditional solvent of N-methyl-2-pyrrolidone (NMP) with both the as prepared PANI and commercial PANI ES (20wt%) on carbon black (Sigma Aldrich). PANI ES powders were firstly ground with agate and then slowly added into the NMP. Magnetic stirring and ultrasonically agitation were applied to the dispersion until no large precipitates of PANI ES were observed in the dispersion.

PANI ES in NMP hybrid sol was prepared by the addition of 3.0ml 2wt% PANI ES NMP dispersion into the as synthesised hybrid PVB sol just before the aging stage.

#### 3.1.3.4 Synthesis of GF modified PVB sol-gel

The corrosion resistance glass flake (GF) used in this study was from CorroCoat, UK. Chemical compositions in weight ratio and other properties of the glass flakes were provided by CorroCoat and are listed in Table 3.2 and Table 3.3. Before preparing the glass flake containing sol, 0.125g of GF001 was firstly dispersed in 5.0ml PVB solution. After slurry of 2.5wt% glass flakes in the PVB solution was prepared, it was then added drop wise into the standard sol-gel before aging to prepare the glass flake modified PVB sol-gel.

SiO <sub>2</sub>	Al <sub>2</sub> O <sub>3</sub>	CaO	MgO	B <sub>2</sub> O <sub>3</sub>	Na <sub>2</sub> O	K <sub>2</sub> O	TiO <sub>2</sub>	ZnO
64-70%	3-6%	3-7%	1-4%	2-5%	8-13%	0-3%	0-3%	1-5%

Table 3.2 Chemical compositions of GF001 glass flakes [155].

50<D<300μm	D<50μm	Thickness/μm	Type	Density/g·cm <sup>-3</sup>	Melt Temperature/°C
<12%	>88%	1.0-1.3	ECR	1.6	930-1020

Table 3.3 Properties of GF001 glass flakes [155].

Notes: 1. Extra corrosion resistant (ECR) glass flake is manufactured from a modified C glass

2. The GF001 glass flakes are micronized

#### 3.1.3.5 Synthesis of PANI and GF modified PVB sol-gel



During the preparation of PANI and GF modified PVB sol-gel, 3.0ml PANI ES nanofibers NMP dispersion and 2.5wt% slurry of GF001 in 5.0ml PVB solution were added into the standard sol-gel before aging.

#### 3.1.3.6 Preparation of sol-gel coatings

The sol-gel thin films were deposited on the surface of AR2024, AD2024 or AE2024 coupons from the as synthesised sols using a dip-coating method, as shown in Fig 3.2. Immersion time for all samples was controlled to be 100s. AA2024 coupons were withdrawn from the sols at a speed of 2.0mm/s. All the sol-gel coated AA2024 coupons were then cured in an oven at 120°C for 2 hours. The samples were kept at the level position to ensure a uniform coating thickness of the sol-gel.

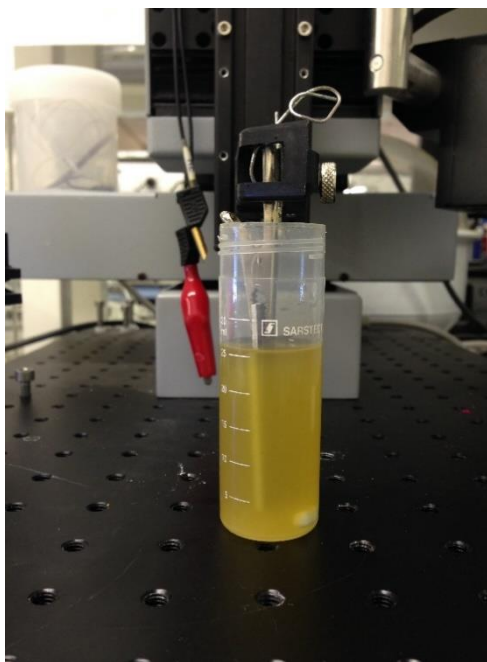


Fig 3.2 Image showing dip-coating method for preparation of sol-gel coatings.

## 3.2 Characterization techniques

### 3.2.1 Scanning electron microscopy with energy dispersive X-ray spectroscopy (SEM/EDX)

The SEM/EDX used in this study was a Quanta 200 FEG Environmental Scanning Electron Microscope (ESEM), as shown in Fig 3.3. The surface morphology and microstructure of the AA2024 alloy with different cleaning procedures were directly examined under SEM/EDX. For the cross-section analysis of the sol-gel coating, AA2024 coupons were embedded in a mixture of Araldite resin and hardener in a weight ratio of 10:1 for 24 hours. Two samples were placed face-to-face to minimise the contact between the sol-gel coating and resin. The surface to be analysed was ground and polished to a mirror finish of 1 $\mu$ m. A thin film of carbon black coating was applied to the surface to prevent charging during analysis in the SEM. Note glass flakes and PANI ES, were conducting, hence they could be both directly observed as fine powers under SEM.

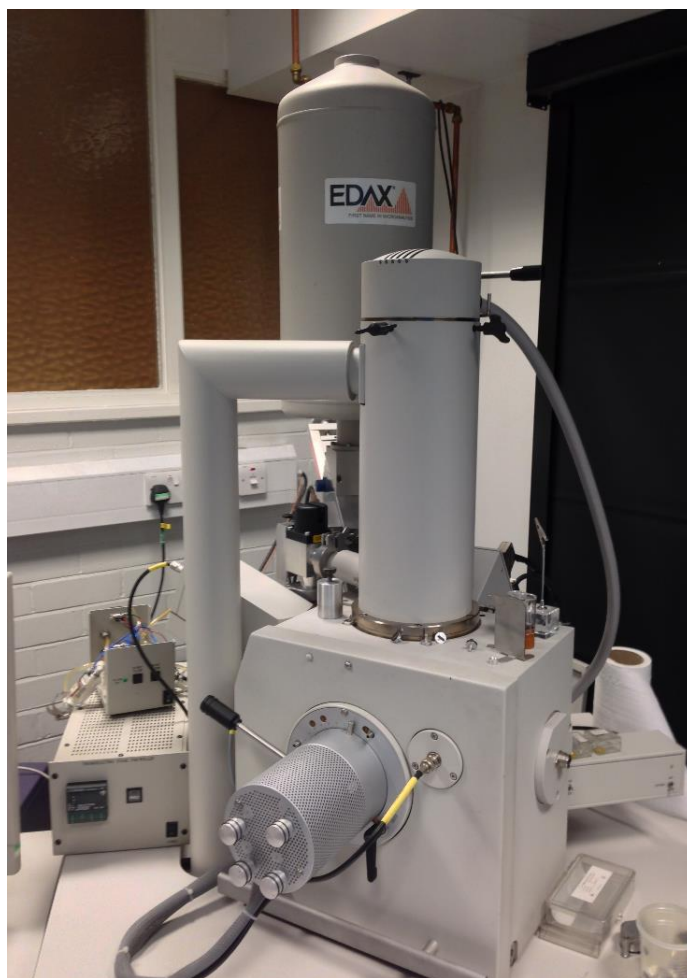


Fig 3.3 Image of Quanta 200 FEG SEM/EDX.

### 3.2.2 Optical Microscopy



Fig 3.4 Images of Zeiss AXIO Lab.A1 2-D Optical Microscope (left) and Bruker ContourGT-I 3D Optical Microscope (right).

A Zeiss AXIO Lab.A1 2-D optical microscope equipped with an AxioCam ERc 5s microscope camera was used to observe the surface condition of both the AA2024 substrate and the deposited sol-gel coatings. A Bruker ContourGT-I 3D optical microscope, which is mainly based on interferometry, was employed to characterize the surface of glass flake modified sol-gel coatings. Images of the two optical microscopes were shown in Fig 3.4.

### 3.2.3 Fourier transformation infrared spectroscopy (FTIR)

A Thermo Electron FTIR Nicolet 5700 with diamond ATR unit was used to investigate the bonding properties of the organic compounds in this study, see Fig 3.5. For the FTIR analysis of organic bonding in sol-gel coating samples, all AA2024 coupons were coated with three layers of sol-gel to enhance the absorbance. Three cycles of immersion and curing were applied to achieve this, as used in the preparation of single layer sol-gel coating on AA2024.



Fig 3.5 Image of Thermo Electron FTIR Nicolet 5700 with diamond ATR unit.

### 3.2.4 Differential scanning calorimetry (DSC) and Thermogravimetry (TG)



Fig 3.6 Images of Q-100 DSC (left) and Q-500 TGA (right) from TA instruments.

Differential scanning calorimetry (DSC) and thermogravimetry (TG) was employed to determine the glass transition and curing temperature, along with the thermal stability of the sol-gel coatings. Three layered sol-gel coatings were deposited onto glass slides with the dip coating method and then used for



DSC/TG analysis. The measurement was carried out on a Q-100 DSC and a Q-500 TGA from TA instruments, USA, as shown in Fig 3.6. The scan rate was 10°C/min from room temperature to 300 °C under the protection of nitrogen atmosphere.

## 3.3 Testing techniques

### 3.3.1 Electrochemical impedance spectroscopy (EIS)

Electrochemical impedance spectroscopy (EIS) was the main technique employed for evaluating the corrosion protection performance of the sol-gel coatings. EIS tests were carried out in a typical aerated three-electrode cell at room temperature. A saturated calomel reference electrode (SCE) and platinum foil (1cm<sup>2</sup>) counter electrode were used in the test electrolyte of 3.5% NaCl aqueous solution in a 200ml plastic vial, as presented in Fig 3.7.

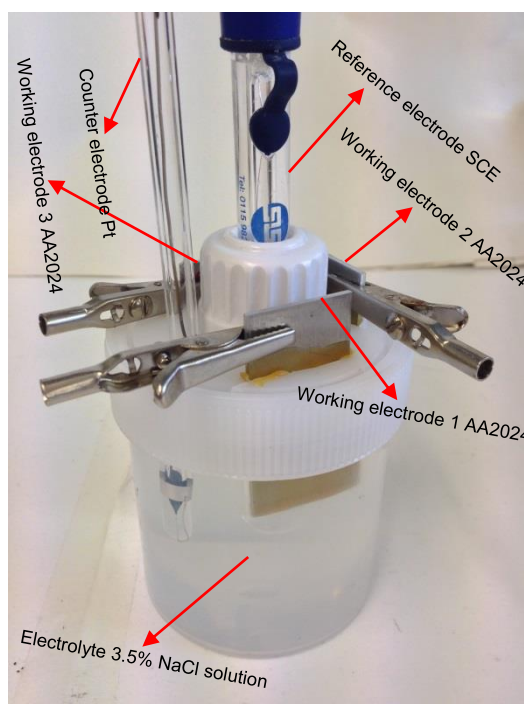


Fig 3.7 Image of typical aerated three-electrode cell used for EIS measurements  
The rear side and edges of the AA2024 samples were all coated with bees wax and colophony resin mixtures in a weight ratio of 3:1. Three samples from the same sol-gel coating were prepared and studied in the same cell. The EIS

measurements were then performed using a Princeton Applied Research Versa STAT 3F. The frequency range applied was from 100,000 Hz to 50mHz with a step of 10 points per decade. All the spectra were recorded with 10mV sinusoidal perturbation at the measured open circuit potential (OCP). Impedance spectra were fitted using ZView 2.70 software from Scribner Associates Inc.

### 3.3.2 Water drop contact angle

Evaluation of surface hydrophobicity was conducted with an FTA 188 Video Tensiometer, as shown in Fig 3.8. For water drop contact angle measurements, one single layered sol-gel coating on AA2024 was used. For each measurement, 8.0 $\mu$ l of deionized water was used to form a water drop on the sample, which was then kept still for 5s to reach equilibrium before the measurement. Ten measurements were taken for each kind of surface on two separate coupons.

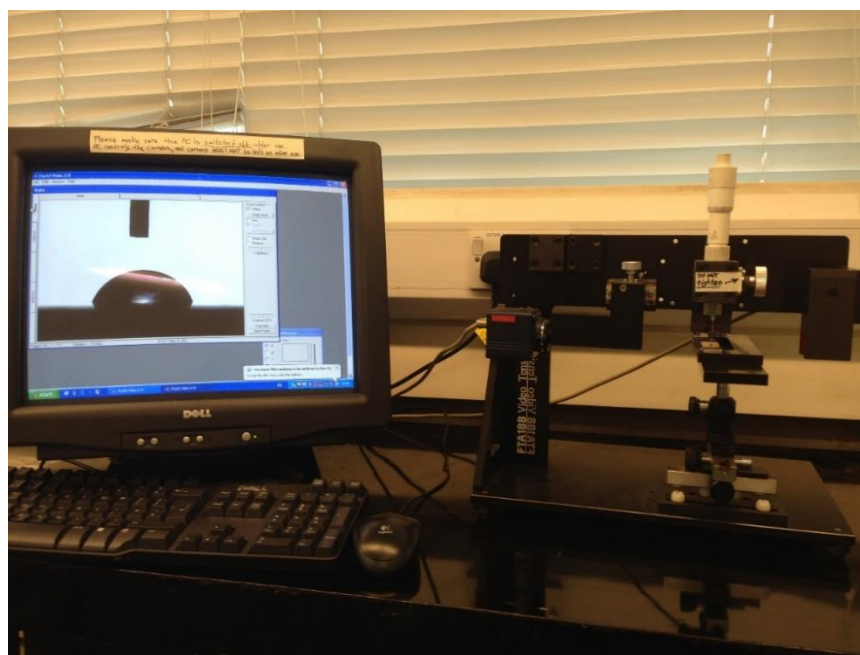


Fig 3.8 Image of FTA 188 Video Tensiometer used in this study.

### 3.3.3 Cross-hatch adhesion testing

The adhesion strength of the sol-gel coating on the AA2024 substrate was tested according to ASTM D3359-09E2 standard [156] using an Elcometer 107 cutter.

Brief operation procedures are described as following steps, see Fig 3.9. Firstly, apply sufficient pressure on a cutter blade to cut through the coating to the substrate. Steadily pull the cutter blade to make a series of parallel cuts about 30mm long. Secondly, make another series of cuts vertical to the first one to create a lattice pattern of cuts (10×10 units (1mm×1mm)), which were then cleaned with a brush. Thirdly, place an ASTM 3359 adhesive tape (~50mm long, 3M Scotch Brand) on the coating to cover the lattice of cuts. Rub the tape firmly using an eraser to ensure good adhesion between the tape and the coating. Fourthly, after applying the tape for between one and two minutes, remove the tape by pulling in a single direction opposite to the coating surface. Finally, observe the condition of the cut lattice under an optical microscopy and apply the results to the ASTM standard listed in Table 3.4.

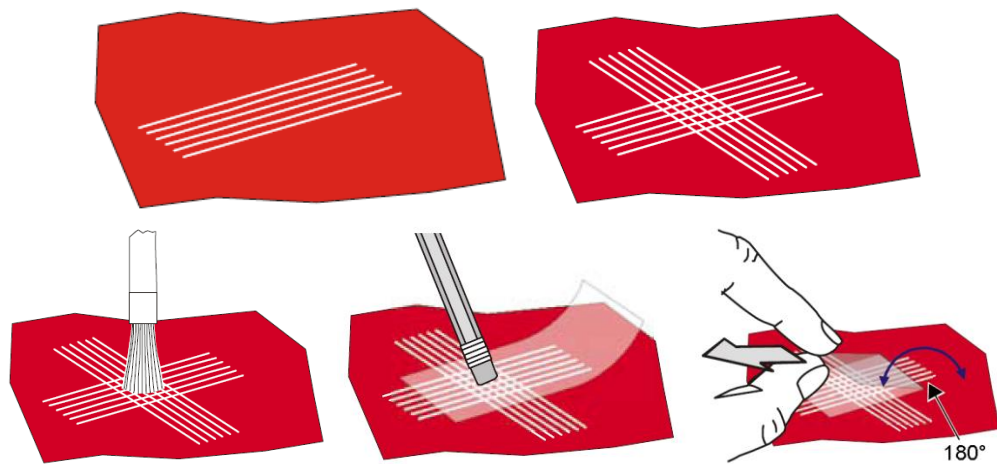


Fig 3.9 Schematic illustrations for the operation procedures of cross hatch adhesion test according to ASTM D3359-09E2 standard [157].

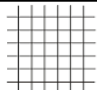
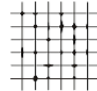
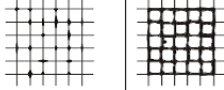
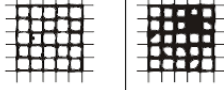
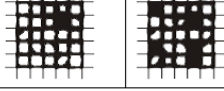

Surface	Description	ASTM
	The edges of the cuts are completely smooth; none of the squares of the lattice is detached.	5B
	Detachment of flakes of the coating at the intersections of the cuts. A cross cut area not significantly greater than 5% is affected.	4B
	The coating has flaked along the edges and/or at the intersections of the cuts. A cross cut area significantly greater than 5%, but not significantly greater than 15% is affected.	3B
	The coating has flaked along the edges of the cuts partly or wholly in large ribbons, and/or it has flaked partly or wholly on different parts of the squares. A cross cut area significantly greater than 15%, but not significantly greater than 35%, is affected.	2B
	The coating has flaked along the edges of the cuts in large ribbons and/or some squares have detached partly or wholly. A cross cut area significantly greater than 35%, but not significantly greater than 65%, is affected.	1B
	Any degree of flaking that cannot be classified even by classification 4 (1B).	0B

Table 3.4 Descriptions and results for cross hatch adhesion test according to ASTM D3359-09E2 standard [157].



# Chapter 4 Results

This chapter consists mainly of three parts, including characterization of materials, corrosion performance of both coated and uncoated samples, and other properties of sol-gel coatings.

In part one, the results on the characterization of the different systems are presented. Firstly, an SEM study was carried out to characterize the surface condition of AA2024 alloy following the different cleaning procedures, to assess the morphology of polyaniline synthesised via different methods and commercial products, as well as the morphology of glass flake.

Part two details the results of the corrosion performance of bare AA2024-T3 alloy and sol-gel coated samples in 3.5% NaCl solutions via EIS measurements. Bare AA2024 with different cleaning procedures and their standard sol-gel coated samples are also presented. The influence of PVB on bare titania-containing sol-gel coatings for the protection of AA2024 were then investigated. Following this, the different kinds of PANI were dispersed in N-Methyl-2-pyrrolidone (NMP) to study their effects on the sol-gel for corrosion protection. Results from sol-gel formulations containing, bare glass flake and its combination with PANI are also provided.

In part three, the hydrophobic nature of the sol-gel coatings was examined using the water drop contact angle technique. Finally, adhesion strength between different sol-gel coatings and substrates was examined by cross-hatch tests.

## 4.1 Characterization of materials

### 4.1.1 Surface condition of AA2024-T3 alloy

The AA2024-T3 alloy was prepared using three different procedures generating samples denoted; acetone cleaning AR2024, nitric acid desmutting AD2024 and alkaline etching AE2024. Scanning electron micrographs (SEM) images showing surface morphologies of these three treatments are displayed in Fig 4.1, Fig 4.2 and Fig 4.3, respectively.

#### 4.1.1.1 AR2024

The AR2024 showed surface damage from the rolling process used to manufacture the sheet material, scratches and cavities, arising from thermomechanical processing, along with the alloy matrix and second phase particles (in the red circles shown in Fig 4.1 b) were also present (Fig 4.1).

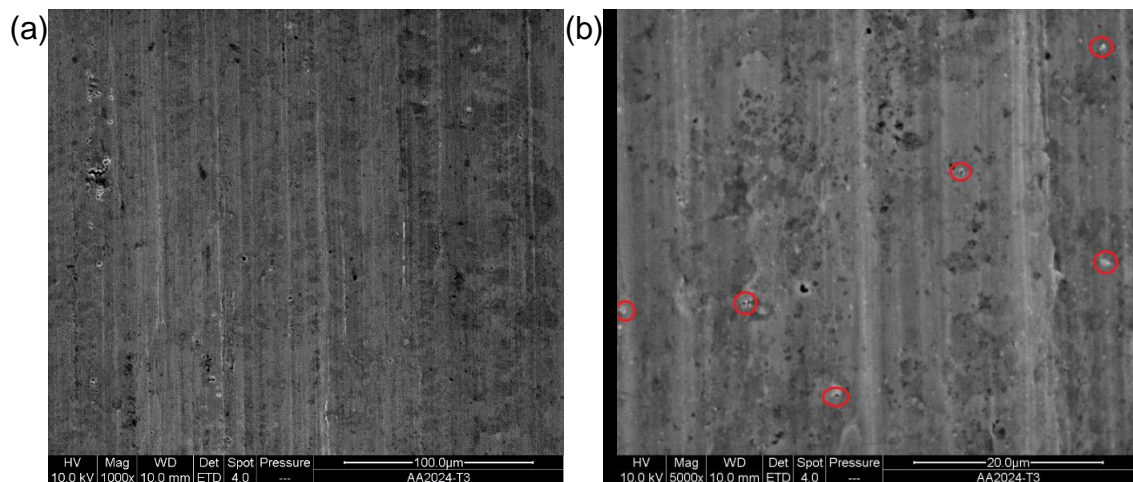


Fig 4.1 SEM images of AR2024 surface.

#### 4.1.1.2 AD2024

After desmutting in nitric acid without prior alkaline etching, the SEM images of AD2024 surface (Fig 4.2) showed residual rolling lines, which were partly dissolved compared with AR2024, and more cavities in various sizes were observed due to the preferential dissolution of second phase particles (in the red circles shown in Fig 4.2 b) on the surface of AD2024.

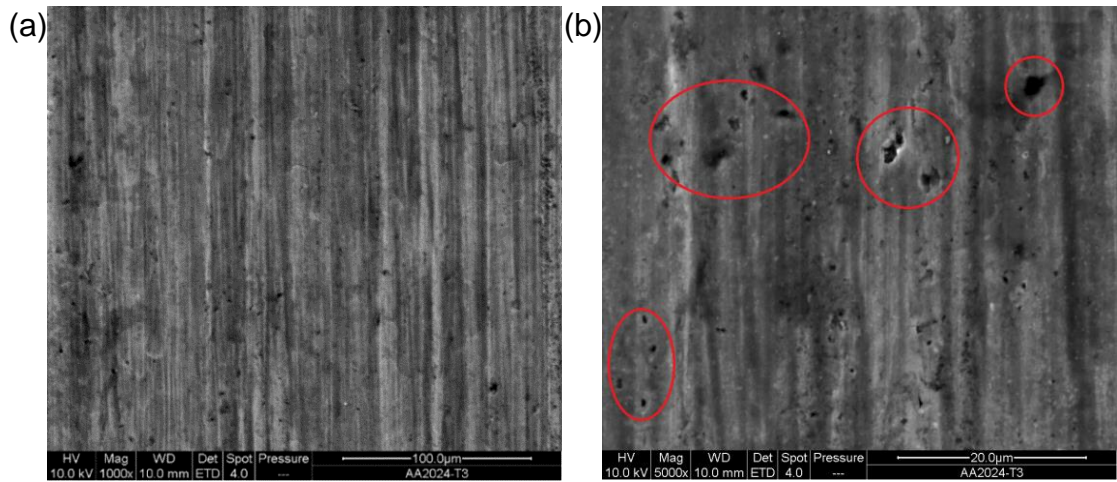


Fig 4.2 SEM images of AD2024 surface.

#### 4.1.1.3 AE2024

AE2024 was prepared following traditional alkaline etching and acid desmutting processes of AA2024. The surface morphology of AE2024 (Fig 4.3) revealed a multi-pitted appearance as the main feature. Many cavities in various sizes were observed due to the loss of second phase particles, some of which were still partly preserved on the surface and in cavities (in the red circles shown in Fig 4.3 b). The rolling lines were found to be almost completely dissolved, leaving a generally smooth surface significantly different from AR2024 and AD2024.

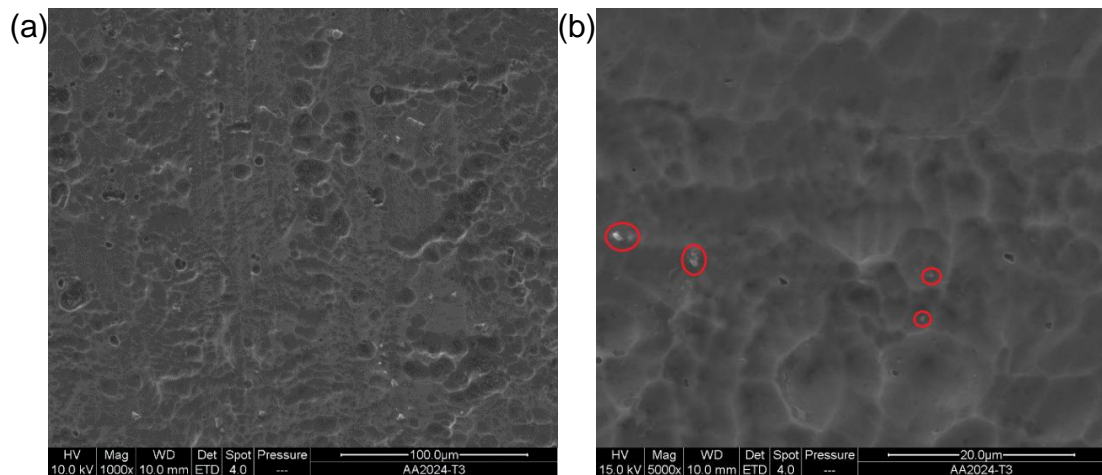


Fig 4.3 SEM images of AE2024 surface.

The surface condition of AA2024 alloy with different cleaning processes was in consist with those reported by others [150, 158].

#### 4.1.2 Morphology of polyaniline

Nanostructured polyaniline (PANI) in emeraldine salt (ES) form was prepared in aqueous nitric acid by conventional polymerization and rapid-mixing methods. Typical SEM images of the obtained PANI ES green powders were shown in Fig 4.4 and Fig 4.5, respectively. Commercial product of PANI ES (20wt%) on carbon black was obtained from Sigma Aldrich UK and characterized by SEM (Fig 4.6).

#### 4.1.2.1 PANI agglomerated particles

PANI ES agglomerated particles (AP) produced from traditional polymerization route were observed from the SEM images in Fig 4.4. The irregular shaped agglomerates of PANI particles produced from this method was due mainly to the heterogeneous nucleation and growth of the PANI polymer chain when the oxidising solution was added drop wise into the aniline solution [95, 133]. However, apart from agglomerated particles, a few short fibres of PANI were also observed due to the intrinsic nanofibrillar morphology of PANI produced in aqueous environment [159]. These short PANI nanofibers were formed from the partial homogeneous polymerization throughout the reaction. However, most of these short nanofibers then acted as nuclei and subjected to heterogeneous nucleation induced overgrowth and agglomeration of PANI, because PANI molecules prefer to grow on previously formed particles [95]. The diameter of the individual unit of the PANI particles was 150~200nm and the length ranged from 400nm to 600nm (Fig 4.4 b). However, the agglomerated particles were significantly larger with a diameter between 5 $\mu$ m to 10 $\mu$ m (Fig 4.4 a).

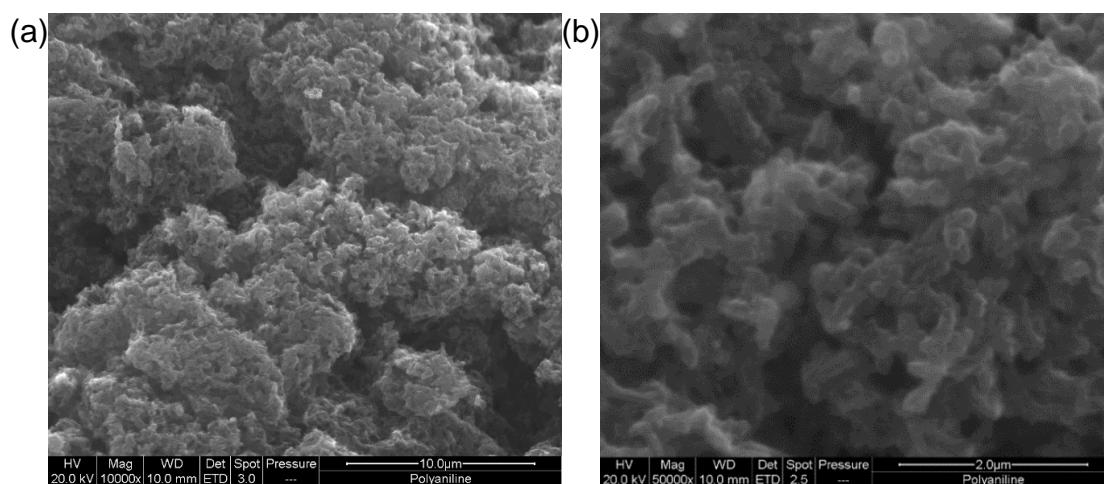


Fig 4.4 SEM images of PANI ES agglomerated particles



#### 4.1.2.2 PANI nanofibers

In Fig 4.5, SEM images reveal that uniform PANI ES nanofibers were produced from rapid-mixing method. The diameter of these nanofibers were around 100nm, which is half of those individual particles produced by traditional polymerization, and the length was between 600nm to 1µm (Fig 4.5 b). Moreover, the nanofibers prepared tend to grow and develop into an interconnected network. The morphology of the as-synthesised nitric acid doped PANI nanofibers were similar to those reported by Huang & Kaner [102, 103]. It is also clear from Fig 4.5 b that the nanofibers obtained were pure, uniform and smooth. This was due to the homogeneous polymerization of aniline monomers and suppression of secondary growth of PANI. As the oxidant was added into the monomer solution all at once followed by stirring to distributed both reactants evenly before the start of the reaction, local high concentration of aniline or oxidant was avoided and almost all the reactants were consumed instantaneously to produce nanofibers through a homogenous reaction [133]. The process is briefly illustrated in Fig 2.13 in Chapter 2. In the lower magnification SEM image of Fig 4.5 a, the PANI nanofibers can be more specifically described as agglomerations of nanofibers, due to the high pressure generated during the filtration process [159].

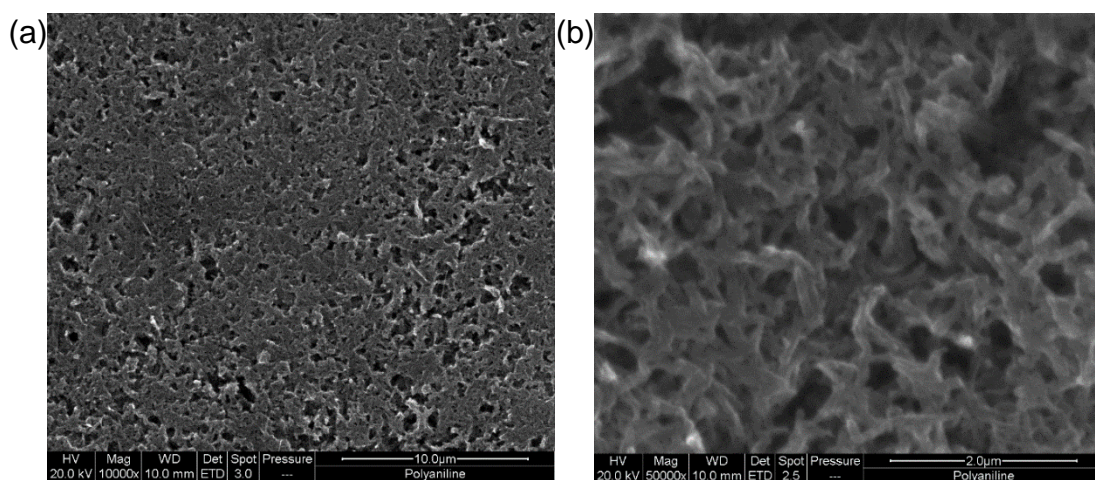


Fig 4.5 SEM images of PANI ES nanofibers.

#### 4.1.2.3 Commercial PANI on carbon black

The commercial product of PANI revealed that the nanoparticle phase was the dominant state of the PANI, see SEM image Fig 4.6 b. Moreover, these

nanoparticles were not individually separated, but bonded on the surface of carbon black and agglomerated to form large spheres of PANI-carbon black composites up to a diameter of 5 $\mu$ m, Fig 4.6 a.

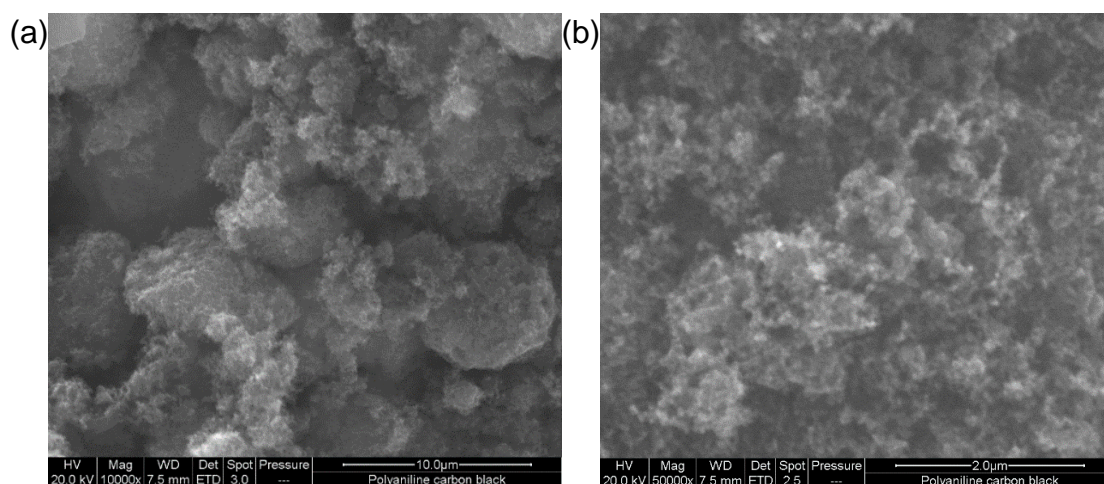


Fig 4.6 SEM images of PANI ES on carbon black.

### 4.1.3 Morphology of glass flake

The GF001 glass flake used in this study was obtained from CorroCoat UK. Prior to use, the size and morphology were characterized with SEM, as presented in Fig 4.7. It is clear from the SEM images that the dominant diameter of the glass flake was below 50 $\mu$ m, corresponded with the properties given in Table 3.3. A small portion of larger glass flake was also present with a diameter between 50 and 200 $\mu$ m. No glass flake was found to have a greater diameter than 200 $\mu$ m.

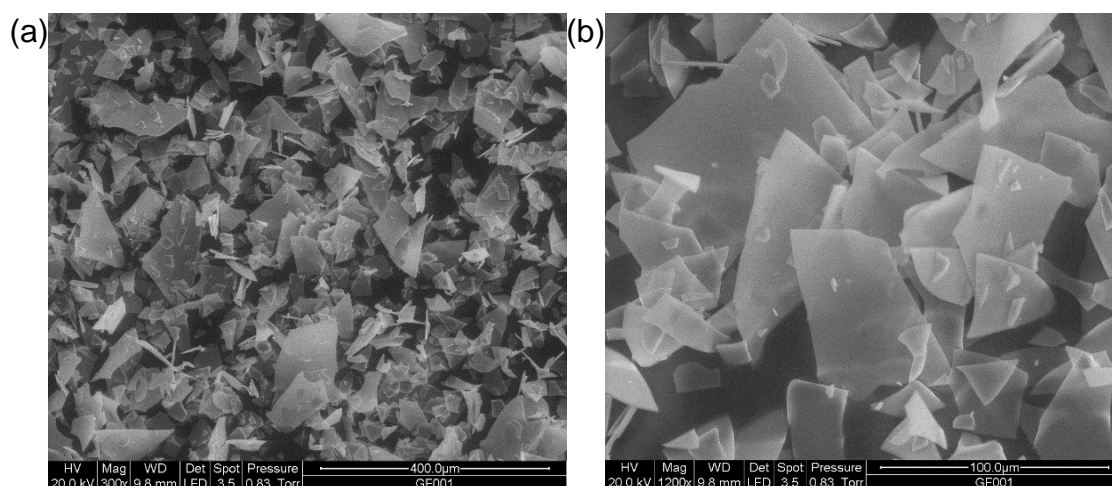


Fig 4.7 SEM images of GF001 glass flake.

## 4.2 Corrosion performance

To assess the corrosion performance of the as prepared sol-gel coatings, EIS was used to study the corrosion behaviour of both coated and bare AA2024 alloy in 3.5% NaCl solution. EIS characteristics were presented in terms of Bode and phase angle plots. Generally, these two plots provide information on the evolution of both resistance (e.g., coating resistance and charge transfer resistance) and capacitance (e.g., pore capacitance and double layer capacitance) components during the corrosion processes.

#### 4.2.1 Bare AA2024

To select suitable cleaning procedures for the AA2024 alloy when applying sol-gel coatings, the corrosion behaviour of both bare and standard sol-gel coated coupons of AR2024, AD2024 and AE2024 in 3.5% NaCl solution were characterized by EIS measurements. Relevant optical microscope, digital and SEM images are also presented.

Bode and phase angle plots of bare AA2024 subject to three cleaning procedures were shown in Fig 4.8. The immersion test results of bare substrates in 3.5% NaCl solution showed that the corrosion behaviour between AR2024 and AD2024 were quite similar. The impedance magnitude ( $|Z|$ ) at all frequency ranges were close to each other, especially at low frequencies (between 0.05Hz and 0.1Hz). This is indicative of active corrosion on the surface [51, 160], over the immersion period, 1 hour to 8 days. However, for AE2024, an obvious decrease in the value of  $|Z|$  at low frequencies was observed compared to the value of  $1.0 \times 10^4 \Omega \cdot \text{cm}^2$  for both AR2024 and AD2024. The impedance magnitude ( $|Z|$ ) at 0.05 Hz for AE2024 fell from  $1.1 \times 10^4 \Omega \cdot \text{cm}^2$  at 1 hour to  $4.0 \times 10^3 \Omega \cdot \text{cm}^2$  at 24 hours and finally to  $2 \times 10^3 \Omega \cdot \text{cm}^2$  at 8 days, indicating greater corrosion attack than the other two substrates.

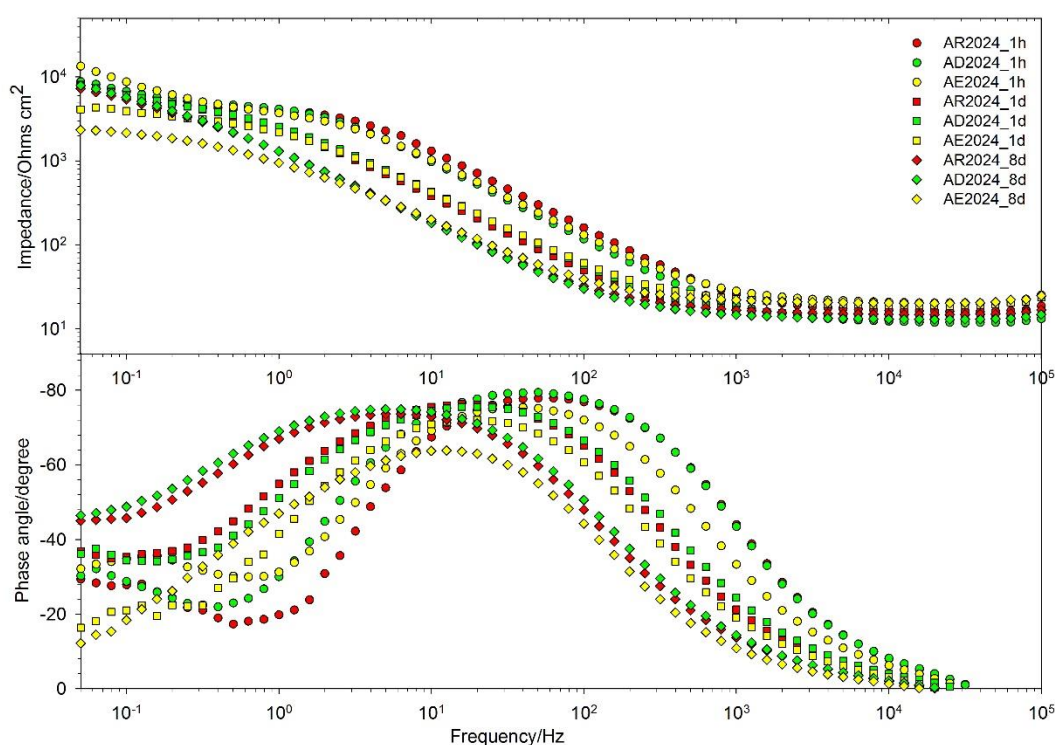


Fig 4.8 Bode (upper) and phase angle (bottom) plots of bare AR2024, AD2024 and AE2024 in 3.5% NaCl solution at 1h, 1 day and 8 days immersion.

The phase angle plots in Fig 4.8 showed a single time constant at medium frequencies (1~100Hz) for almost all the phase angle plots, except for the second time constant of AE2024 at 0.1Hz, which indicating “general corrosion” [161], during 1 hour and 24 hours immersion. A shift of the time constant to lower frequencies was also observed, which may be related to an increase of the double layer capacitance [162], indicating continuous corrosion. This is also seen from the decrease in impedance over time, at medium frequencies in the corresponding Bode plots.

The three substrates all suffered from heavy pitting corrosion, based on optical micrographs, when comparing the images before (Fig 4.9 a) and after (Fig 4.9 b) immersion for 8 days in 3.5% NaCl solution. A great number of pits (diameter around 10 $\mu$ m) were observed after corrosion on all surfaces, although larger pits up to a diameter of 50 $\mu$ m were found on the surface of AE2024. Digital images are also shown in Fig 4.9 c for samples after immersion in 3.5% NaCl solution for 8 days showing large pits on AE2024 and small pits on both AR2024 and AD224.



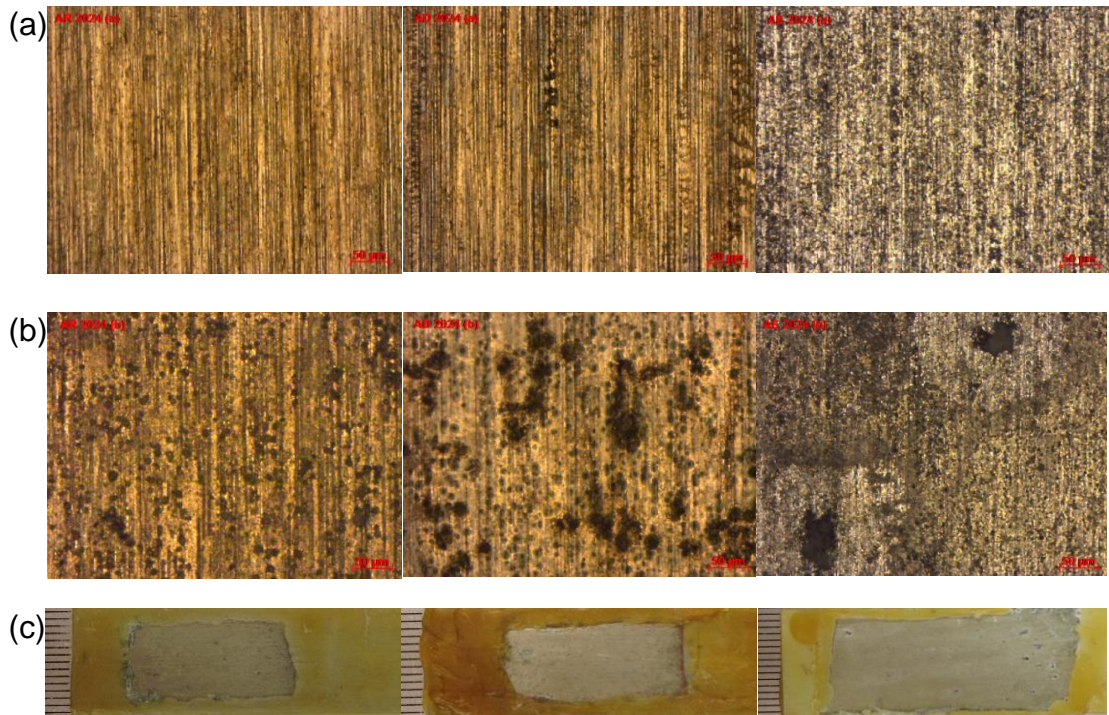


Fig 4.9 Optical microscopy images of bare AR2024 (left), AD2024 (middle) and AE2024 (right) (a) before and (b) after 8 days immersion in 3.5% NaCl solution; (c) Digital images after 8 days immersion.

#### 4.2.2 Standard sol-gel coatings

For standard sol-gel coated AA2024 samples, EIS results were presented for 1 hour, 8 and 24 hours immersion in 3.5% NaCl solution. Bode and phase angle plots are presented in Fig 4.10.

Due to the barrier properties of the hybrid titania-containing sol-gel coatings on AA2024 alloy, the value of  $|Z|_{0.05\text{Hz}}$  was generally two orders higher than bare AA2024 alloys at initial 1 hour immersion, despite the cleaning procedures applied, evidencing the barrier properties of the sol-gel coating. Although the fact that, AR2024 and AD2024 have similar corrosion behaviour in 3.5% NaCl solution, their sol-gel coated counterparts showed large differences. During initial immersion, the value of  $|Z|_{0.05\text{Hz}}$  for AD2024\_SG was  $1 \times 10^6 \Omega \cdot \text{cm}^2$ , being half of the value for that of AR2024\_SG. However, AD2024\_SG suffered from a large decrease in impedance during 8 hours immersion and the value of  $|Z|_{0.05\text{Hz}}$  fell from  $1 \times 10^6 \Omega \cdot \text{cm}^2$  to  $1 \times 10^4 \Omega \cdot \text{cm}^2$ , the same as that of uncoated AA2024 samples,

indicating breakdown of the sol-gel coating on AD2024. However, for AR2024\_SG, the impedance magnitude at 0.05Hz only decreased by about one order of magnitude to  $1 \times 10^5 \Omega \cdot \text{cm}^2$  during 8 hours and fell to  $3 \times 10^4 \Omega \cdot \text{cm}^2$  at 24 hours, which was three times than that of AD2024\_SG at 8 and 24 hours immersion.

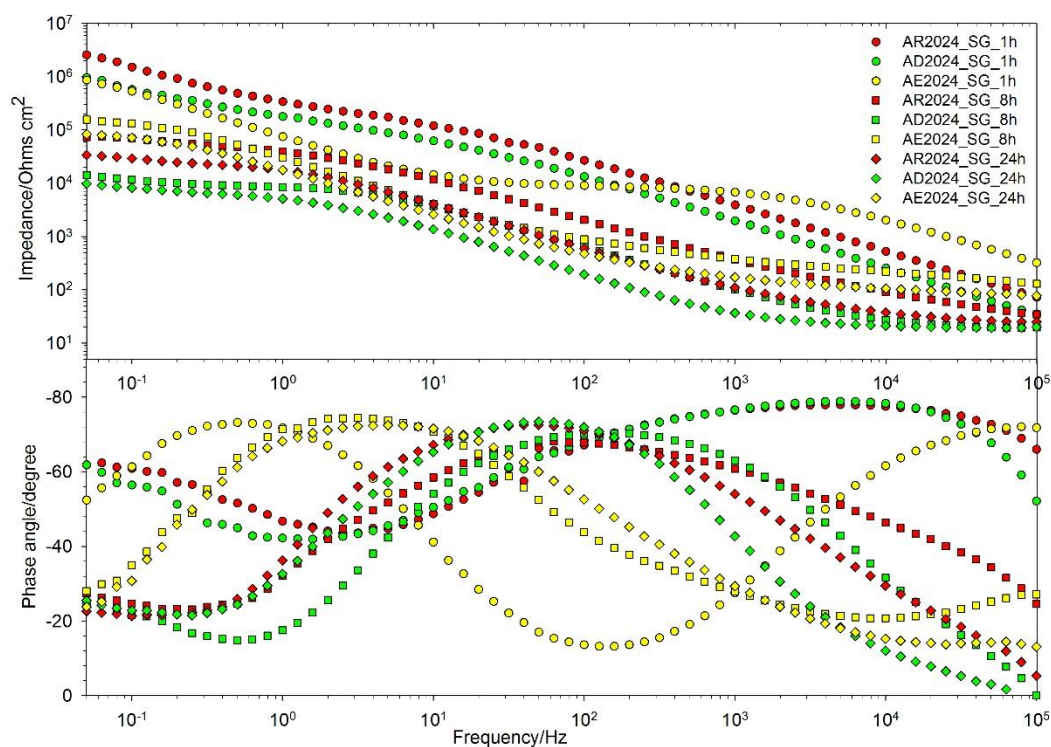


Fig 4.10 Bode (upper) and phase angle (bottom) plots of standard sol-gel coated AR2024 (AR2024\_SG), AD2024 (AD2024\_SG) and AE2024 (AE2024\_SG) in 3.5% NaCl solution at 1 hour, 8 and 24 hours immersion.

For AE2024\_SG, the value of  $|Z|_{0.05\text{Hz}}$  at 1 hour immersion was the same as that of AD2024, namely  $1 \times 10^6 \Omega \cdot \text{cm}^2$ . However, the impedance magnitude at 0.05Hz of sol-gel coated AE2024 decreased to  $2 \times 10^5 \Omega \cdot \text{cm}^2$  and  $1 \times 10^5 \Omega \cdot \text{cm}^2$  at 8 and 24 hours immersion, respectively. After 24 hours, all the three coatings were subjected to continuous decrease in the impedance at low frequencies. The Bode plots reveal that standard sol-gel coating on AE2024 surface retains its barrier properties and provides higher corrosion resistance than the other two coatings. This may be related to activation of the alloy surface after removal of the oxide film and the availability of free hydroxyl ions [163], which result in the formation

of Al-O-Si or Al-O-Ti bonds leading to better adhesion between the surface and the sol-gel coating [77].

The differences in the evolution of phase angle over time also showed that the sol-gel coating on AE2024 behaved differently from the other two systems. Two well-defined time constants were found for sol-gel coatings on AE2024. The first, at high frequency ( $\sim 10^5$ Hz), can be ascribed to the capacitance of the sol-gel coating, which can be correlated with the hydrophobicity of the sol-gel coating [164]. The second time constant at ( $\sim 0.5$ Hz) may be related to the capacitance of the intermediate conversion layer between the coating and substrate formed by Al-O-Si or Al-O-Ti bonds [51, 79, 165]. However, the second time constant was not clearly observed with the AR2024\_SG and AD2024\_SG. According to P. Álvarez et al [158], a second time constant has been observed on a hybrid sol-gel coated AA2024 alloy having an oxide layer on the surface. A possible reason for this might be that the second time constant was shifted to lower frequencies beyond the frequency range used in the current tests, being attributed to the diffusion of electrolyte to the intermediate layer [166]. For AE2024\_SG, two time constants were observed during 24 hours immersion. However, the phase angle for the first one, at high frequencies, significantly decreased over time, due to the porous nature of sol-gel network, water uptake into coatings and hydrolysis of sol-gel [67]. Although the sol-gel coatings on all the substrates suffered from electrolyte attack, their barrier properties still provide the alloy with additional resistance. From the phase angle plots, the remaining time constant for sol-gel coatings on AE2024 is at about 3Hz, which may be attributed to the barrier properties from the intermediate layer between the coating and substrate. However, for AR2024 and AD2024, the time constant are observed at 50Hz, which may be related to the pore resistance of the sol-gel coating.

The thickness of the coatings on the different substrates was characterized by SEM and displayed in Fig 4.11. Results revealed that the thickness of sol-gel

coatings on AR2024, AD2024 and AE2024 were 2.2 $\mu$ m, 2.6 $\mu$ m and 3.2 $\mu$ m, respectively.

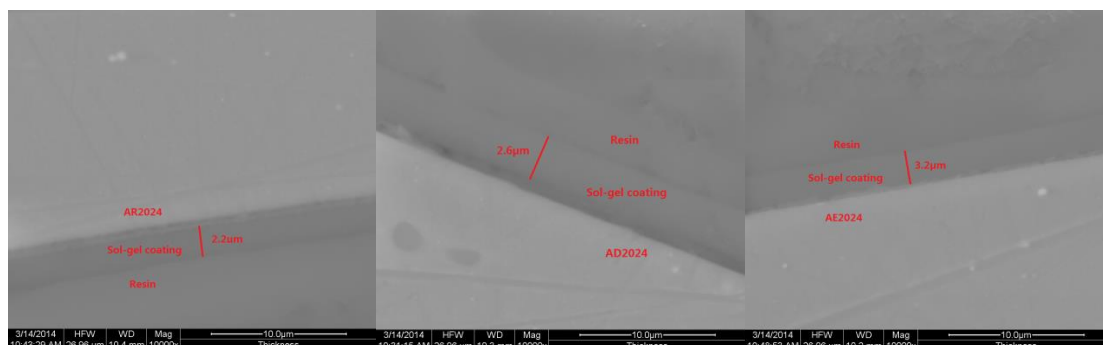


Fig 4.11 Cross-section SEM images of standard sol-gel coatings on AR2024 (left), AD2024 (middle) and AE2024 (right).

From comparison with optical images (Fig 4.12 a, b) of sol-gel coated samples before and after immersion in 3.5% NaCl solution for 8 days, difference in corrosion behaviour among the three substrate was also obvious. Both AR2024\_SG and AD2024\_SG suffered from intense corrosion attack, especially at the weakest area around rolling marks. This may stem from the shrinkage of the sol-gel coating during the curing process. Although the coating thickness on three substrates were all between 2.2-3.2 $\mu$ m and able to cover the whole surface from SEM observations, narrow gaps between rolling lines may still lead to thinner coating sites in these regions.

For AE2024, due to the complete dissolution of rolling lines, less preferential corrosion attack was observed, being replaced instead with many small pits. This was also generally clear from the digital image (Fig 4.12 c) when comparing the surface of the coatings after 8 days immersion in 3.5% NaCl solution. Moreover, delamination of the sol-gel coatings was also observed on AR2024\_SG and AD2024\_SG, due to the poor adhesion between the coating and substrates.

To summarize, although the bare AE2024 coupons have poor corrosion resistance than AR2024 and AD2024, the sol-gel coatings on this substrate showed better corrosion protection for AA2024 alloy. Therefore, the traditional alkaline etching and acid desmutting process were used to clean the surface of AA2024 alloy and applied as substrates for other modified sol-gel coatings.



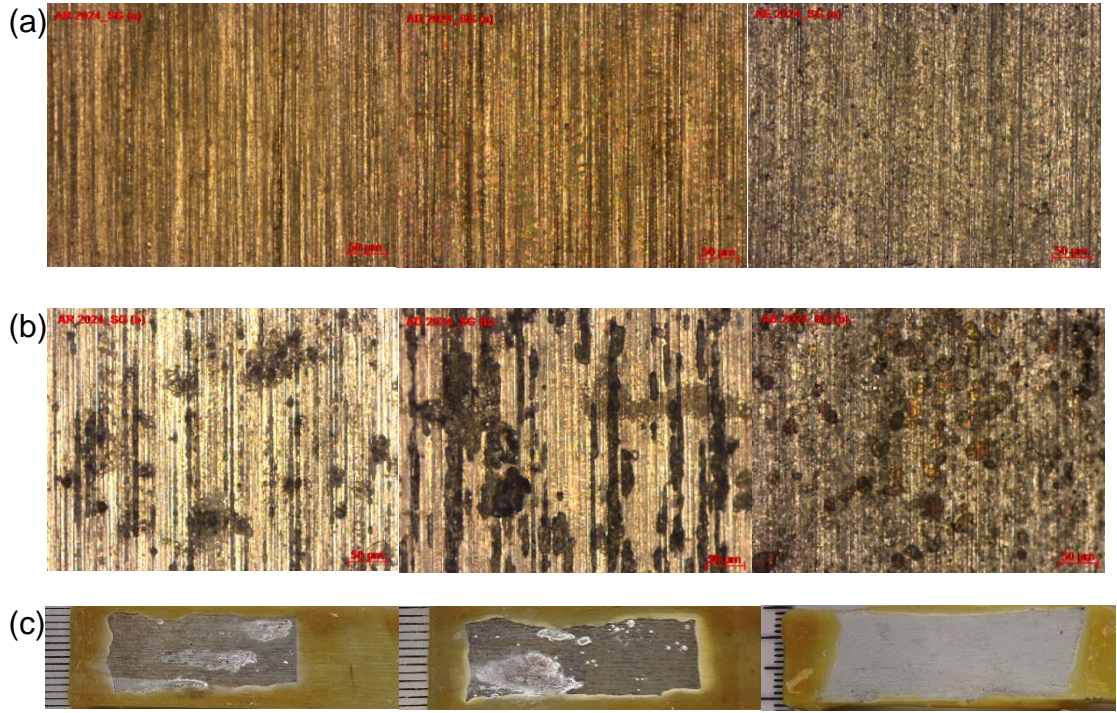


Fig 4.12 Optical microscopies(a),(b) of bare AR2024\_SG (left), AD2024\_SG (middle) and AE2024\_SG (right) (a) before and (b) after 8 days immersion in 3.5% NaCl solution and (c) digital images after 8 days immersion.

### 4.2.3 Co-polymer modified sol-gel coatings

Polyvinyl butyral (PVB) as a chelating agent, binder and co-polymer, has been proved to be effective in enabling hybrid sol-gel system to produce thicker and crack-free thin films as well as improve corrosion performance for aluminium alloys [80]. PVB has also been proved to be superior in improving coating adhesion to the surface of AA2024 alloy [167] as well as increasing the cross-linking properties of the sol-gel network via Si-O-C bonds [168]; hence is promising in the formation of a denser sol-gel coating. Moreover, the addition of PVB to the silica sol-gel coatings is considered to also reduce the permeability to water and moisture [169]. Herein, PVB was added in the hybrid sol-gel system in this study for the improvement of corrosion protection of AA2024.

Two volume ratios of PVB (10wt% solution in ethanol) were added in the standard sol-gel to produce two new coatings, namely sol-gel/PVB=8 (SG\_PVB\_8) and sol-gel/PVB=4 (SG\_PVB\_4). Bode and phase angle plots, presented in Fig 4.13,

were obtained for the coatings immersed in 3.5% NaCl solution for 1 hour, 1 day and 4 days.

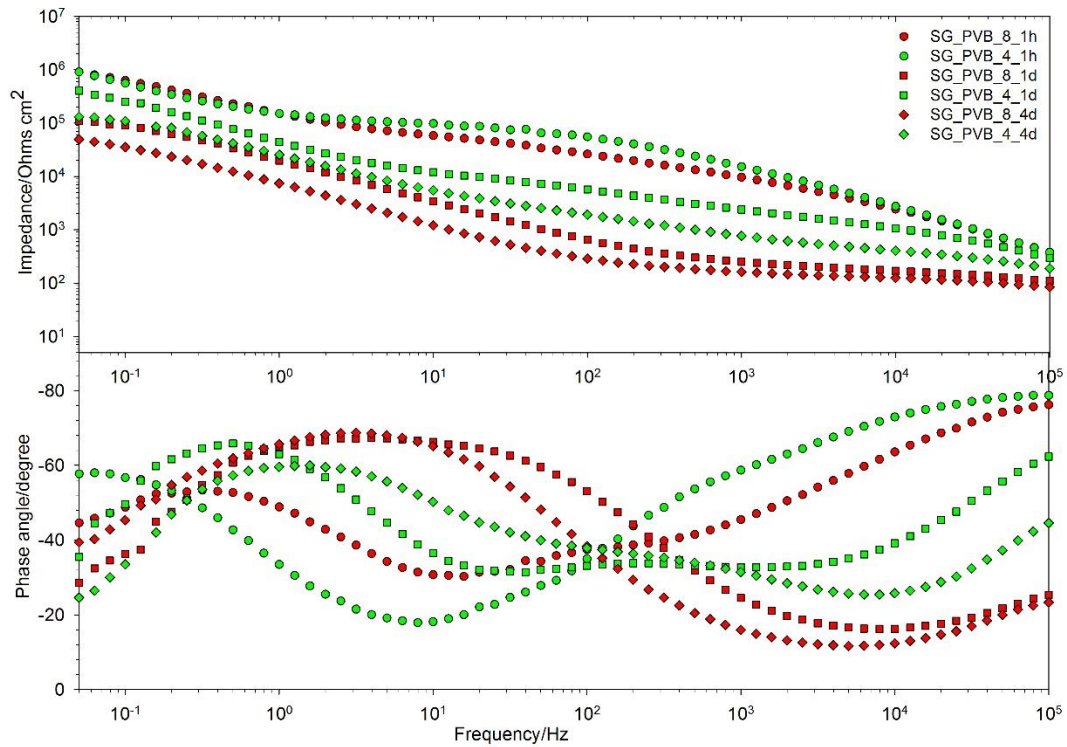


Fig 4.13 Bode (upper) and phase angle (bottom) plots of PVB modified sol-gel coatings on AE2024 in 3.5% NaCl solution at 1 hour, 1 day and 4 days immersion. Volume ratios of PVB (10wt% solution in ethanol) versus the standard sol-gel were SG\_PVB\_4 and SG\_PVB\_8.

From the Bode plots for SG\_PVB\_4 and SG\_PVB\_8, it is clear that the initial 1 hour value of  $|Z|_{0.05\text{Hz}}$ , whilst not surpassing the  $1 \times 10^6 \Omega \cdot \text{cm}^2$  value achieved from the control sol-gel coating, barrier properties of the sol-gel coatings, were maintained at a reasonable level of  $5 \times 10^5 \Omega \cdot \text{cm}^2$  and  $1 \times 10^5 \Omega \cdot \text{cm}^2$  for SG\_PVB\_4 and SG\_PVB\_8 respectively during 1 day immersion and then dropped slightly to  $1 \times 10^5 \Omega \cdot \text{cm}^2$  and  $5 \times 10^4 \Omega \cdot \text{cm}^2$  after 4 days immersion. The results from both the PVB coatings were superior to those of standard sol-gel coatings on AE2024 as shown in Fig 4.10. However, this improvement in corrosion resistance may not be from an increase in the coating thickness, from about  $3.2 \mu\text{m}$  of standard sol-gel coatings to  $4.0 \sim 5.0 \mu\text{m}$  of PVB sol-gel coatings, as shown in SEM cross-section images in Fig 4.11 and Fig 4.14. The best corrosion performance between

the standard and PVB modified sol-gel coatings was from SG\_PVB\_4, which may directly ascribed to the optimum ratio of PVB added, as there were big differences in the corrosion performance of PVB modified coatings with different ratio of PVB, but similar thickness. Moreover, it was observed that SG\_PVB\_2, with a higher ratio of PVB and a thickness of 5.3 $\mu$ m, causes a loss of the protection for AA2024 on initial immersion (results not shown).

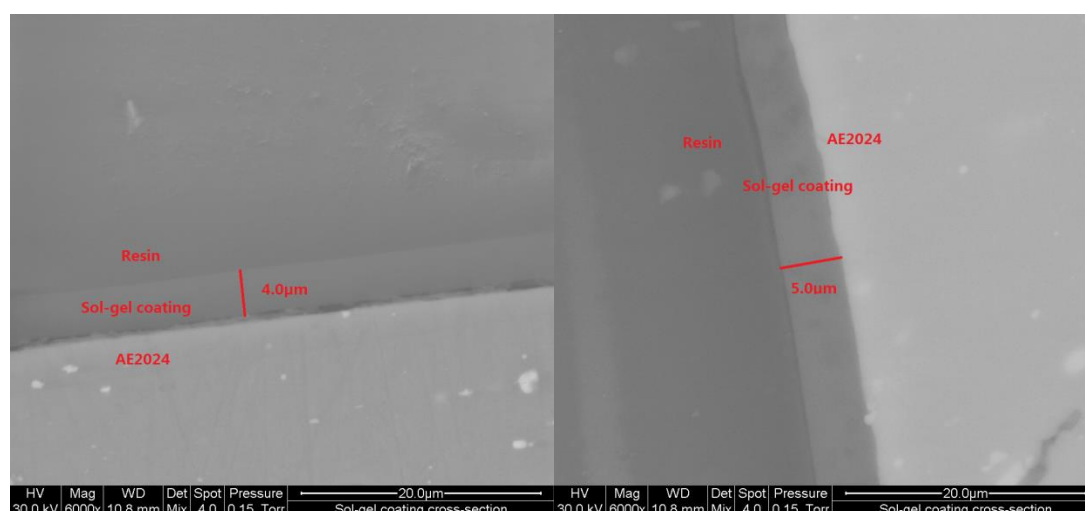


Fig 4.14 Cross-section SEM images of PVB containing sol-gel coatings, SG\_PVB\_8 (left), SG\_PVB\_4 (right).

This can be concluded that the optimum ratio of PVB addition to the sol-gel was SG\_PVB\_4. If the PVB ratio is low as for SG\_PVB\_8, only limited cross-linking and permeability to water may be provided. However, if the PVB ratio is too high, for example as for SG\_PVB\_2, adverse effects could be introduced to the integrity of the sol-gel coating, due to the increasing shrinkage and resulting defects [170]. This behaviour has also been observed during the testing on SG\_PVB\_2 sol-gel coatings (results not shown), which failed at the beginning of immersion, indicating cracks formed during drying procedures [67]. After 4 days immersion, both coatings were subject to following decrease in impedance, indicating continuous loss of corrosion protection by PVB modified sol-gel coatings.

In the phase angle diagrams, it was observed that two time constants were present for both coatings over 4 days immersion. However, the sol-gel coatings



with higher ratio of PVB clearly indicate much better resistance to water uptake, as the phase angle at  $10^5\text{Hz}$  after 4 day immersion for SG\_PVB\_4 remained at -40 degrees, while this was reduced to -20 degrees for SG\_PVB\_8 after one day. Note both coatings had phase angle values of -80 degrees on initial immersion. The improved behaviour of SG\_PVB\_4 over that of SG\_PVB\_8 may be ascribed to better additional cross-linking and pore-blocking properties provided by SG\_PVB\_4.

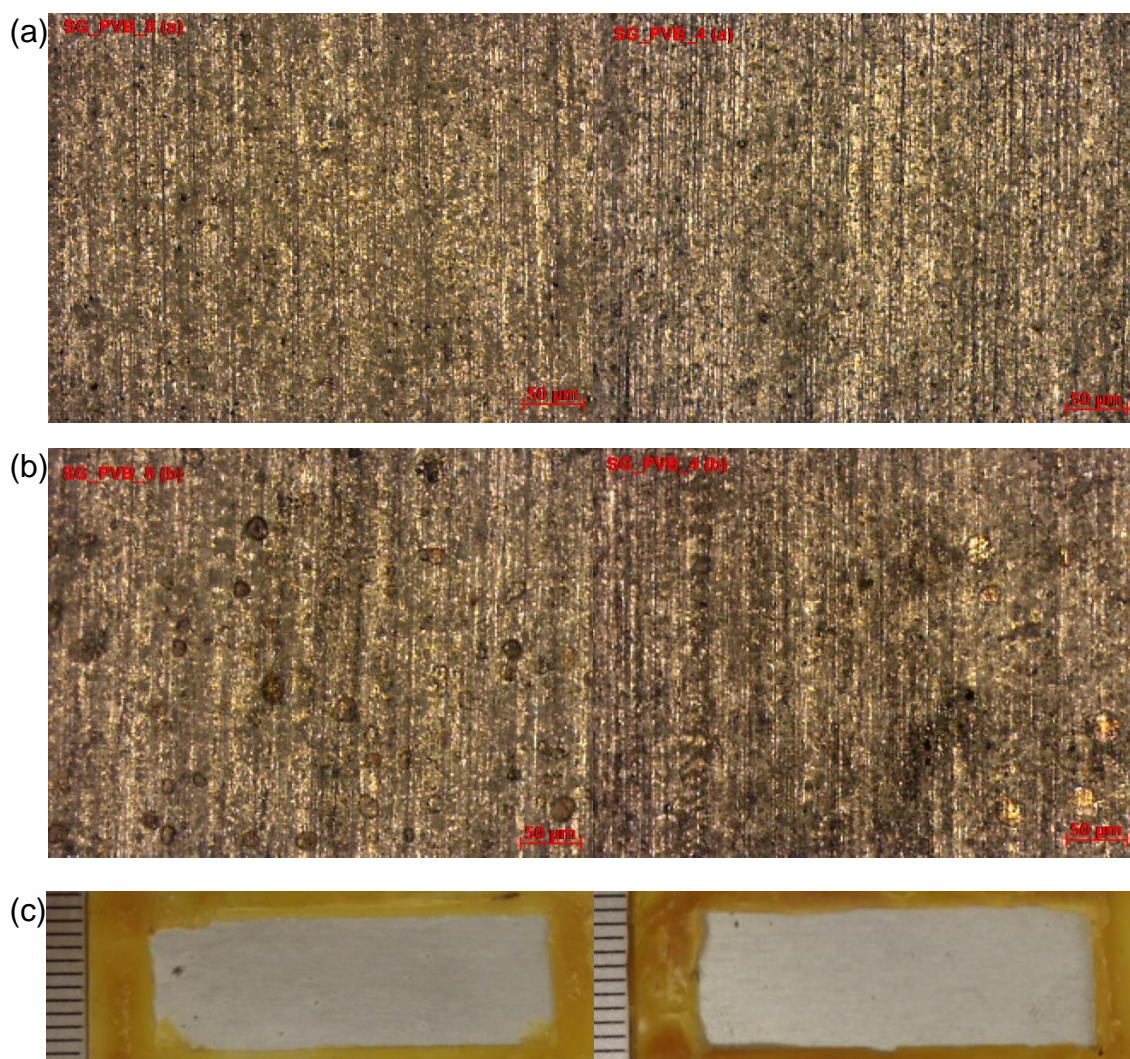


Fig 4.15 Optical micrographs of SG\_PVB\_8 (left) and SG\_PVB\_4 (right) (a) before and (b) after 8 days immersion in 3.5% NaCl solution and (c) digital images after 8 days immersion.

Moreover, from the optical micrographs and digital images (Fig 4.15) before and after immersion for 8 days in 3.5% NaCl solution, it was also clear that fewer pits



were formed on the SG\_PVB\_4 coatings than SG\_PVB\_8, indicating that the former system could provide better corrosion protection for AA2024 alloy.

It may be concluded that suitable addition of PVB in the sol-gel coating is useful in improving the anticorrosive properties and the optimal volume ratio in this system appears to be SG\_PVB\_4. Therefore, PVB were added to the sol-gels in a ratio of SG\_PVB\_4 for following coatings.

#### 4.2.4 Polyaniline modified sol-gel coatings

In this section, studies were focused on the addition of PANI in the SG\_PVB\_4 coating. The as synthesised emeraldine salt (ES) form of PANI agglomerated particles (AP), nanofibers (NF) and commercial product of PANI ES (20wt%) on carbon black (CB) were dispersed in NMP to form 2wt% dispersion before being added into the SG\_PVB\_4 sol-gels. The thickness of PANI containing sol-gel coatings was measured from cross-section SEM images as typically displayed in Fig 4.16 with PANI\_NF added, at a value of  $4.8\mu\text{m}$  as well as those for PANI\_AP and PANI\_CB modified coatings. Bode plots and phase angle diagrams were displayed in Fig 4.17 during the 1 hour, 4 and 8 days immersion in 3.5% NaCl solution for PANI\_AP and PANI\_NF modified sol-gel coatings and 1 hour and 4 hours immersion for PANI\_CB ones.

From the Bode plots, it was clear that improved corrosion protection was obtained by the addition of as synthesised PANI than bare PVB sol-gel coatings, but not for commercial PANI\_CB, which was detrimental for the sol-gel coatings producing a low initial value of impedance at low frequencies ( $1 \times 10^5 \Omega \cdot \text{cm}^2$ ) along with a rapid decrease to  $1 \times 10^4 \Omega \cdot \text{cm}^2$  within 4 hours, indicating early failure of the coating. For PANI\_AP/NMP\_PVB and PANI\_NF/NMP\_PVB, the value of  $|Z|_{0.05\text{Hz}}$ , although both similar at the start of the experiment ( $2 \times 10^6 \Omega \cdot \text{cm}^2$ ) and twice the value of the PVB sol-gel coatings, both coatings maintained a relatively high impedance, above  $1 \times 10^5 \Omega \cdot \text{cm}^2$  for over 4 days immersion; which then slowly

decreased during the following 8 days. Although PANI\_AP/NMP\_PVB had slightly higher values of impedance than PANI\_NF/NMP\_PVB, no major differences were observed between them.

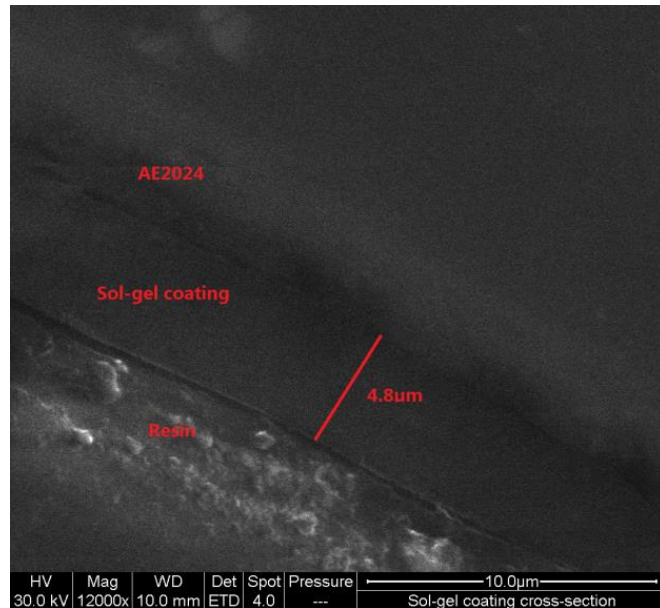


Fig 4.16 Cross-section SEM images of PANI\_NF modified PVB sol-gel coatings.

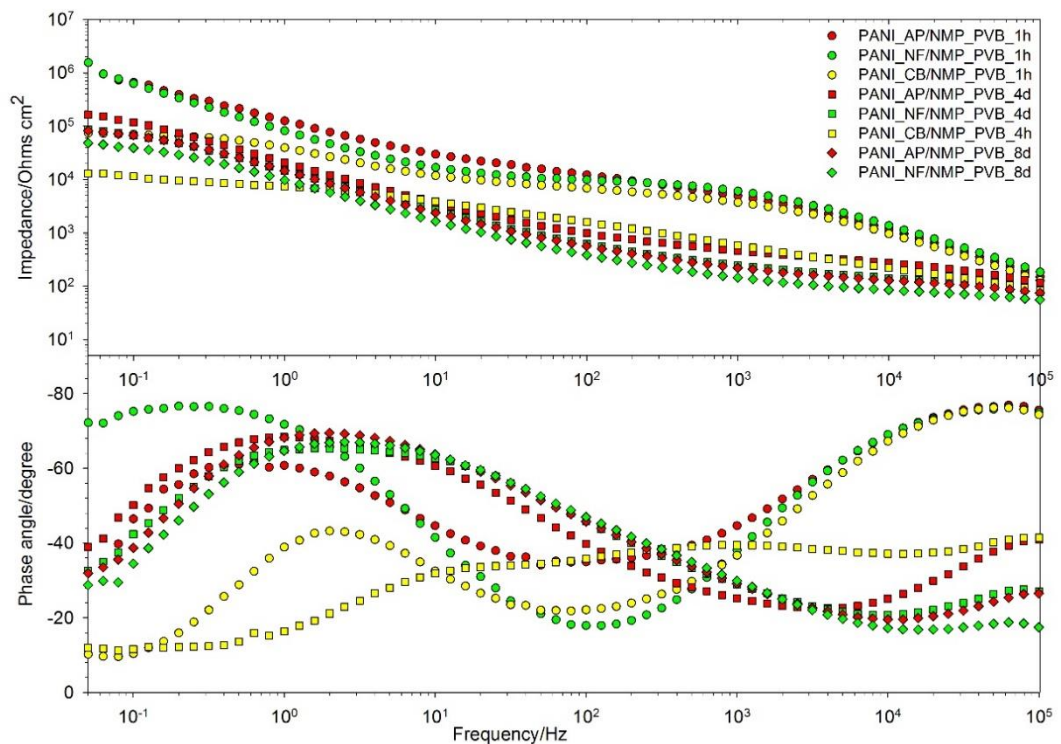


Fig 4.17 Bode(upper) and phase angle (bottom) plots of PANI containing PVB sol-gel coatings on AE2024 in 3.5% NaCl solution at 1 hour, 4 days and 8 days immersion. (PANI\_AP/NMP\_PVB, PANI\_NF/NMP\_PVB and PANI\_CB/NMP\_PVB refers to the addition of PANI ES agglomerated particles, nanofibers and carbon black composites into SG\_PVB\_4 sol-gels, respectively.)

The phase angle diagrams shown in Fig 4.17 present two time constants for all three coating systems. However, for PANI\_CB/NMP\_PVB, with the exception of initial hydrophobicity, indicated by high value of phase angle at high frequencies, this coating showed the least resistance, falling quickly within the first 4 hours. It should be noted that a complication arises with carrying out impedance measurements on coatings that contain conducting polymers. By its nature, EIS assess the resistance offered by a coating, with high impedance indicative of a good coating. Introduction of a component that is conducting can give artificially low resistance, which is not attributed to coating breakdown. This low resistance may be ascribed to the existence of a high ratio of conducting carbon black together with conductive PANI, both of which increase the conductivity of the electrolyte in the pores of the coatings [40]. Further, carbon black did not bond within the sol-gel, but adversely affected the existing polymeric network, leading to large pores, defects or cracks. The loose bonding properties of carbon black in the sol-gel were observed from the fact that the carbon black was easily removed from the coating after 8 days of immersion. The slower decrease of the phase angle at  $10^5\text{Hz}$  through time of PANI\_AP/NMP\_PVB over that of the PANI\_NF/NMP\_PVB indicated that the sol-gel coatings with agglomerated particles seem to be denser with lower permeability to water than nanofibers. This may be due to the higher solubility of PANI AP in NMP could help the particles to be evenly distributed in the sol-gel network. Moreover, time constant at around 3Hz did not shift, indicating a stable intermediate layer between the coating and substrate with high resistance to electrolyte attack.

During the observation from both the optical micrographs and digital images in Fig 4.18, it was found that PANI\_CB/NMP\_PVB coated AA2024 exhibited, significant pitting after immersion for 8 days. This is in comparison to the PANI\_AP/NMP\_PVB and PANI\_NF/NMP\_PVB coatings, where no obvious pits were observed for both coatings after 8 days immersion (Fig 4.18 b). It was also noted that the PANI was well dispersed. Moreover, it can be seen from the optical

images that large PANI AP (1-2 $\mu$ m) was well distributed in the coating, where smaller size (<1 $\mu$ m) of PANI NF was dispersed. This may be explained by the differences in both particle size and solubility of the agglomerate and nanofiber forms of PANI. As PANI agglomerated particles were hard to separate individually, the size of these particles was bigger than that of the uniform and individually separated nanofibers. Moreover, as the agglomerated particles have short polymer chains, they have better solubility in NMP than that of the longer chain nanofibers which are individually separated. Digital images of the three coatings after 8 days immersion (Fig 4.18 c) also shows that PANI\_CB coatings suffered from severe pitting corrosion, whilst the synthesised PANI agglomerated particles and nanofibers coating systems provided greater corrosion protection with no evidence of pitting. Note, the black sites in the images were actually dark green PANI particles in the sol-gel coatings.

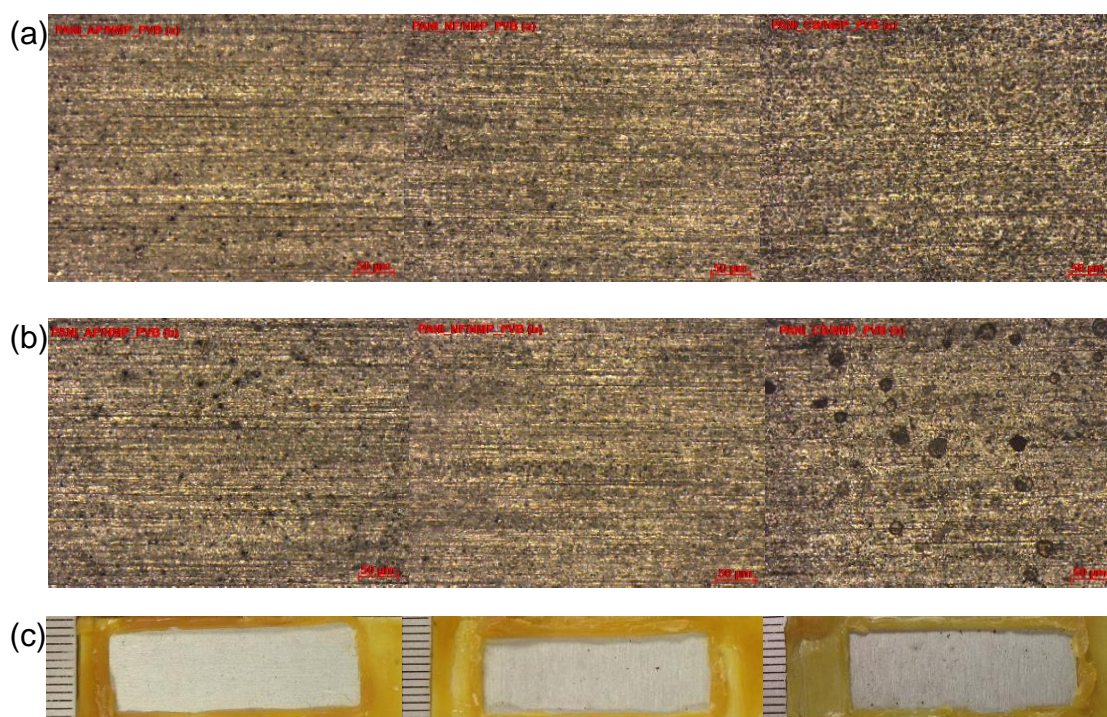


Fig 4.18 Optical micrographs of PANI\_AP/NMP\_PVB (left), PANI\_NF/NMP\_PVB (middle) and PANI\_CB/NMP\_PVB (right) (a) before and (b) after 8 days immersion in 3.5% NaCl solution and (c) Digital images after 8 days immersion. In summary, NMP dispersion of the PANI ES form of agglomerated particles or nanofibers within the PVB sol-gel improved the corrosion protection performance

of coating system on AA2024. Conversely, commercial PANI ES on carbon black had severe adverse effects on the corrosion protection on sol-gel coatings. Compared with bare PVB sol-gel, it was clear that the protection mechanism of PANI should not due to the barrier properties of PANI, from the sharp drop of phase angle at low frequencies with time of PANI modified sol-gel coatings than bare PVB modified ones.

#### 4.2.5 Glass flake modified sol-gel coatings

Following on in the development of the coating systems from the previous section, a further addition was made to the selected PANI-nanofiber/PVB coating in the form of glass flake, notably GF001 (2.5wt% slurry in PVB solution). Here a combination of PANI nanofibers (2% dispersion in NMP) with GF001 in PVB sol-gel were produced and investigated for the corrosion protection of AA2024. For comparison, a control coating consisting of the SG\_PVB\_4 with GF001 glass flake was prepared and tested. Bode plots and phase angle diagrams are presented in Fig 4.19 for immersion in 3.5% NaCl solution for 1 hour, 1 day and 4 days for bare GF001 coatings and 1 hour, 4 and 8 days for GF001\_PANI coatings. The thicknesses for both coatings were similar to the SG\_PVB\_4 coatings at 5.0 $\mu$ m.

From the Bode plots, it can be seen that for both coatings at initial immersion, a value of  $|Z|_{0.05\text{Hz}}$  of  $1 \times 10^6 \Omega \cdot \text{cm}^2$  was obtained, similar to that of the bare sol-gel coatings, regardless of the presence of glass flake or a combination with PANI. However, the value of  $|Z|_{0.05\text{Hz}}$  of GF001\_PVB coatings did undergo a rapid decrease to  $3 \times 10^5 \Omega \cdot \text{cm}^2$  during 1 day immersion, which was similar to the GF001\_PANI\_NF/NMP\_PVB coating at 4 days immersion. Unlike previous system of SG\_PVB\_4, where an impedance values stabilised, the value of  $|Z|_{0.05\text{Hz}}$  for GF001\_PVB coatings was subject to a further decrease to  $6 \times 10^4 \Omega \cdot \text{cm}^2$  over the next 4 days immersion. This response is considerably worse than



that of bare PVB sol-gel coatings, indicating adverse effects of bare GF001 added in the sol-gel coatings. However, after addition of PANI NF in the GF001\_PVB coatings, the resistance was almost totally preserved from 4 days immersion to 8 days.

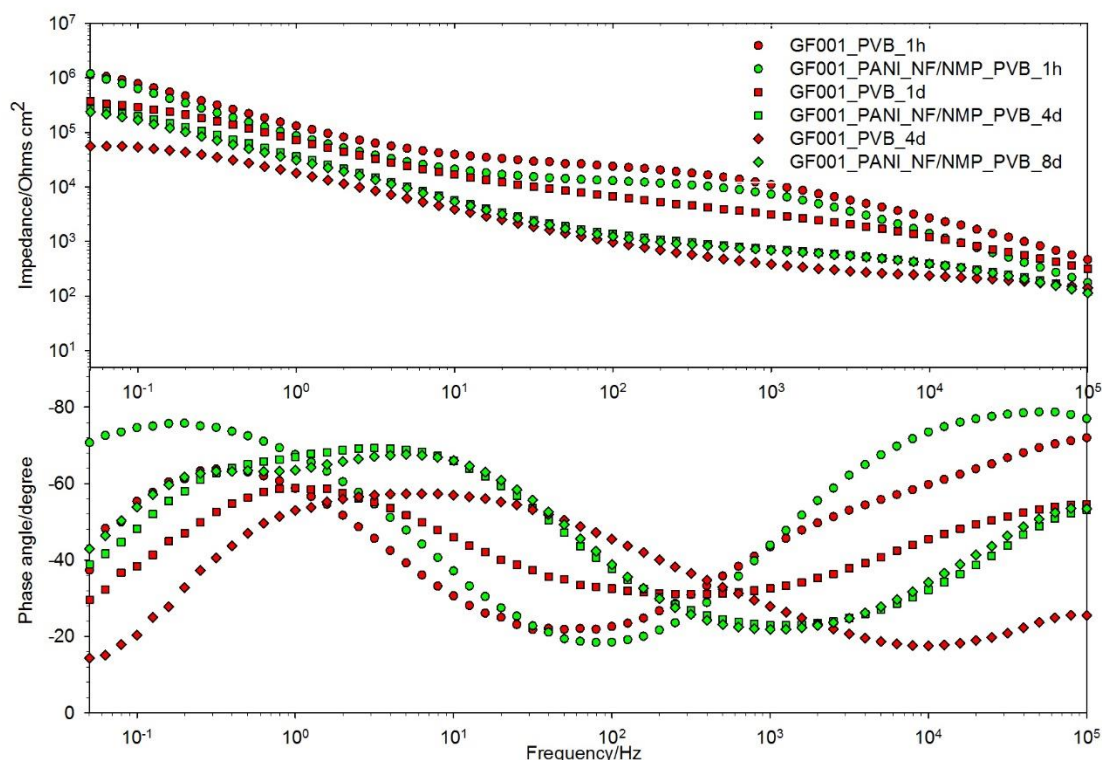


Fig 4.19 Bode(upper) and phase angle (bottom) plots of glass flake containing PVB sol-gel coatings(GF001\_PVB) on AE2024 in 3.5% NaCl solution at 1 hour, 1 days, 4 days immersion and combination of GF001 and PANI ES nanofibers (GF001\_PANI\_NF/NMP\_PVB) at 1 hour, 4 days and 8 days immersion.

In the phase angle diagrams shown in Fig 4.19, two time constants were observed for all curves. However, as the phase angle at high frequencies were maintained for GF001\_PANI\_NF/NMP\_PVB coatings during 4 days and 8 days immersion, it was evident that the addition of PANI was useful in conserving the dielectric characteristics of the sol-gel coating causing a decrease in electrolyte diffusion into the coating. When bare glass flake was added, a comparison of the phase angle evolution at high frequencies of the bare PVB sol-gel coating suggests more pores or defects are present following the introduction of the glass flake. This in turn leads to a more rapid decrease in phase angle at high

frequencies over time. A third time constant at 0.5Hz started to appear for GF001\_PANI\_NF/NMP\_PVB coating during 8 days immersion, indicating corrosion activity for the substrate. However, as both the phase angle curves and Bode plots for this coating was almost the same during 4 days and 8 days immersion, it is suggested that the combination of GF001 and PANI NF was superior in providing the PVB sol-gel coating with lower water permeability, longer and higher effective corrosion resistance, unlike the addition of glass flake alone, which has adverse effects on the PVB sol-gel coatings.

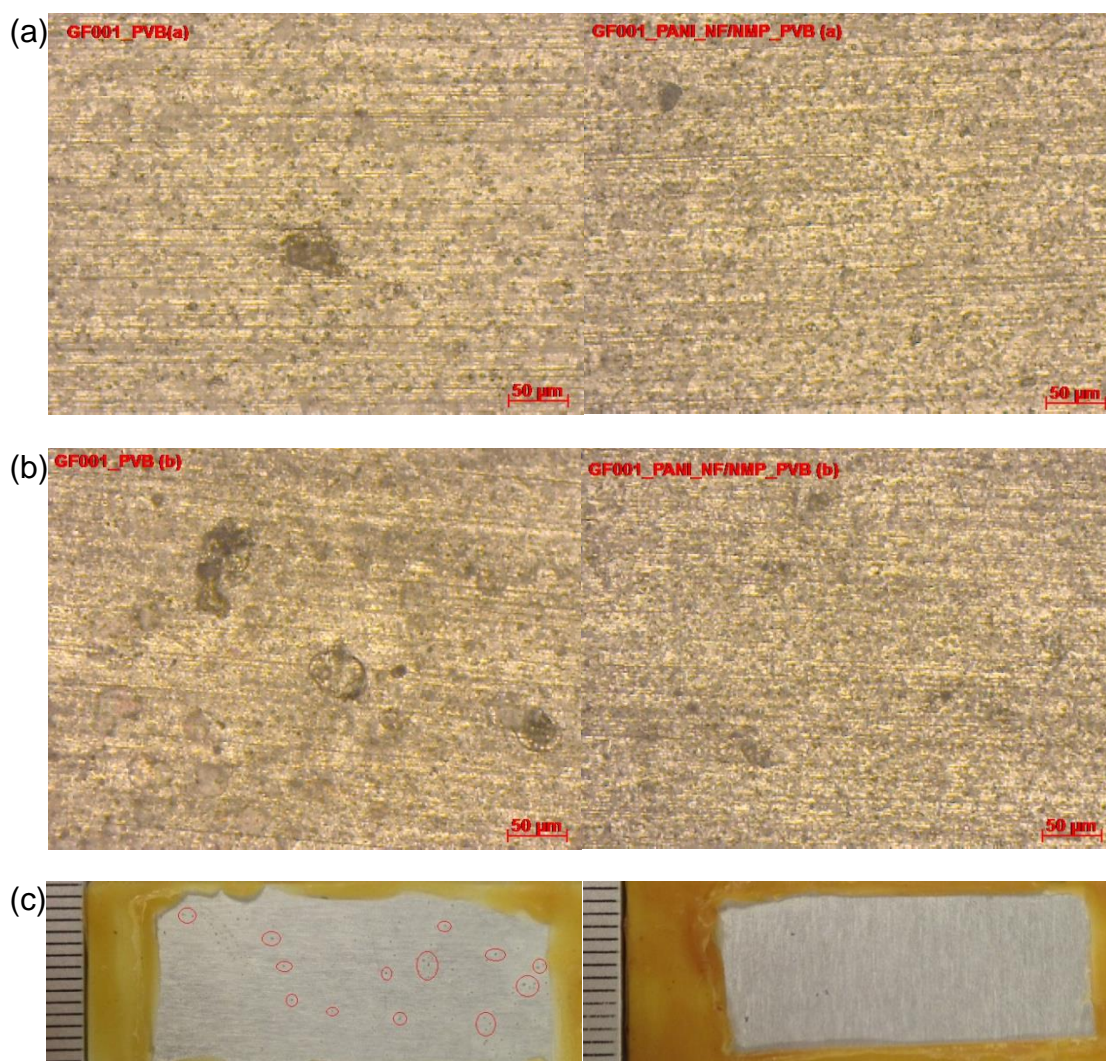


Fig 4.20 Optical micrographs of GF001\_PVB (left) and GF001\_PANI\_NF/NMP\_PVB (right) (a) before and (b) after 8 days immersion in 3.5% NaCl solution and (c) Digital images after 8 days immersion.

From the optical and digital images of bare GF001 modified PVB sol-gel coatings before (Fig 4.20 a) and after (Fig 4.20 b) 8 days immersion in 3.5% NaCl solution,

it can be seen that pits were introduced by the presence of glass flake, which was more obvious from the corresponding digital images in Fig 4.20 c (most pits were labelled in the red circles). There was almost no change in the GF001\_PANI\_NF/NMP\_PVB coating after immersion from the images (note, black points on digital image were PANI particles). Small glass flake (diameter<50 $\mu$ m) was observed in the sol-gel coatings, however, bare addition of GF001 did lead to adverse effects on bare PVB coatings. This may be due to the destructive properties of glass flake to the sol-gel network, leading to direct attack of electrolyte on the substrate, through the formation of a weaker network in the coatings. However, the introduction of PANI NF did bring a level of stability through the formation of an intermediate layer, working in combination with the glass flake that provided a barrier to the electrolyte, giving the resulting good anticorrosive properties of the sol-gel coating.

## 4.3 Properties of the sol-gel coatings

### 4.3.1 Contact angle measurements

The hydrophobicity of the surface of both bare AA2024 and various prepared sol-gel coatings were assessed using water contact angle measurements. Average results of ten measurements on each sample are displayed in Fig 4.21.

It can be seen from the results that the surface of bare AA2024 was increased by conducting surface pre-treatments, especially for AE2024. The rough and smooth surface as well as the residual hydroxyl ions, obtained by alkaline etching and acid desmutting can be seen in the SEM images (Fig 4.3), which were reasonable for a hydrophobic surface with the highest contact angle of 92.3° among all the samples. The surface of the as-received and acid desmuted bare AA2024 showed low contact angles of 67° and 74°, respectively, which were more hydrophilic and may due to the roughness of their surface and the native oxide layer. Although the contact angle for AE2024\_SG was the highest among the



three SG-only coatings, they were all hydrophilic with contact angle lower than  $90^\circ$  [171].

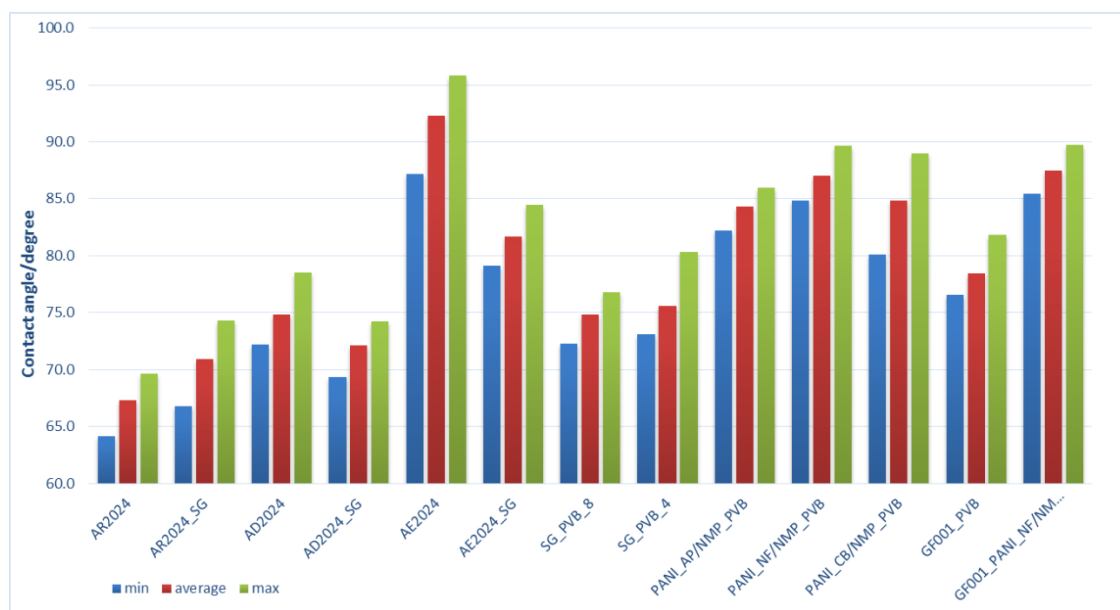


Fig 4.21 Contact angle for the surface of bare AA2024 and various sol-gel coatings.

After the addition of PVB in the sol-gel, the contact angles were all decreased to  $75^\circ$  by the two ratios. This may stems from the hydrophilic properties of the PVB, whose pure thin film has a value of  $60^\circ$  for contact angle [172]. When PANI was added in the sol-gel, the values for contact angle were all increased by about 10 degrees compared with SG\_PVB coatings, especially for PANI nanofibers, which are known to be superhydrophobic with a water contact angle up to  $164.5^\circ$  [173]. The influence of PANI in increasing the hydrophobicity of the sol-gel coatings was also shown when comparing the results of the last two samples. If glass flake was added in the SG\_PVB\_4 coatings, very small increase (3 degrees from  $75^\circ$  to  $78^\circ$ ) was obtained. However, when PANI nanofibers were added together with glass flake, the hydrophobicity of the coating was similar to those without glass flake of PANI\_NF/NMP\_PVB coatings with the same value of  $87^\circ$ .

### 4.3.2 Cross-hatch adhesion tests

The adhesion strength between the sol-gel coatings and the substrate is vital for the performance of sol-gel coatings if they are to be used commercially as a pre-

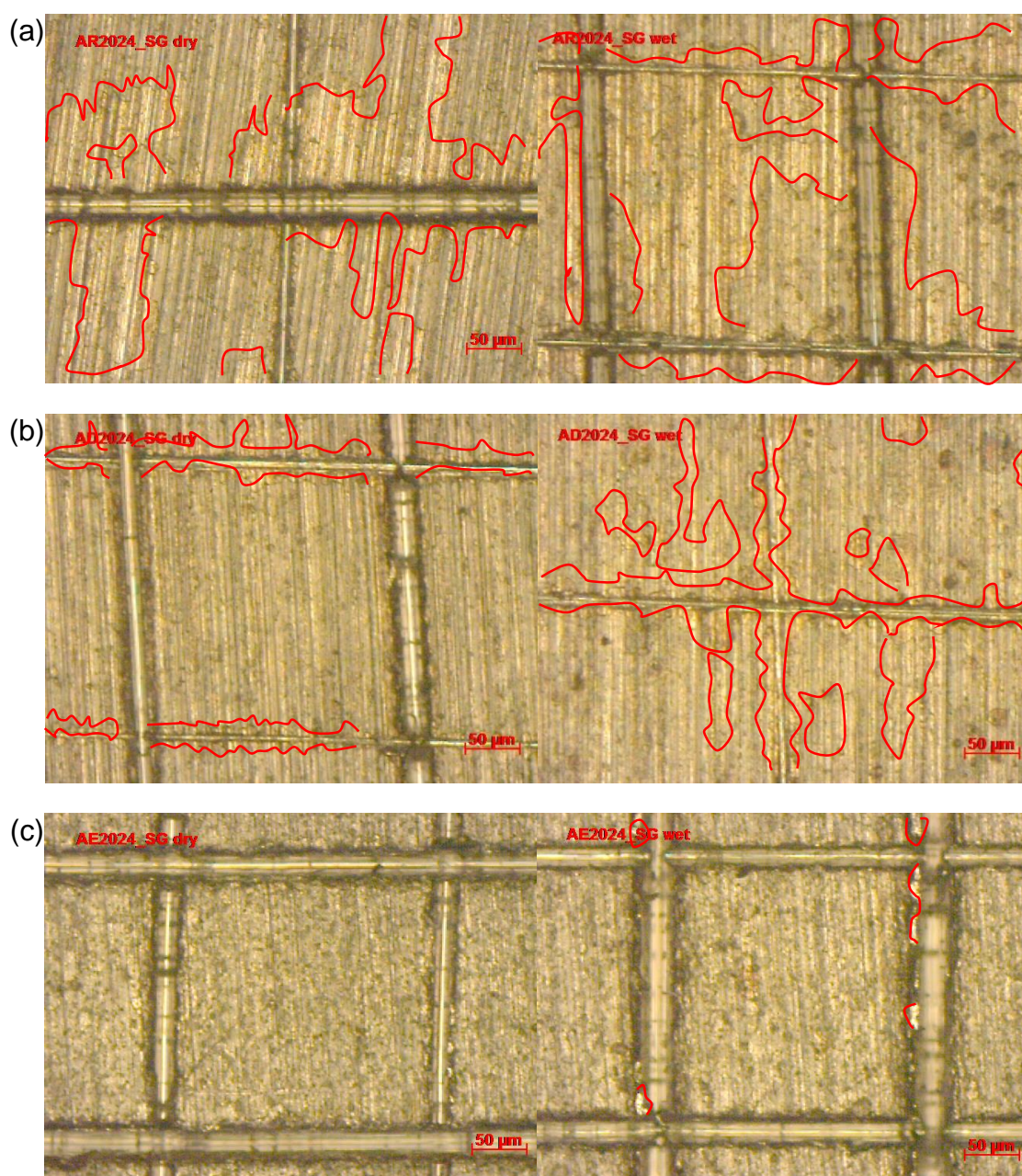
treatment layer. Cross-hatch test results are presented in Table 4.1 and related to the classifications in ASTM D3359 standard as given in Table 3.4. Dry samples were tested when sol-gel coatings were initially prepared, alongside wet samples which were examined on coatings after immersion in 3.5% NaCl solution for 24 hours. Typical optical micrographs on the condition of all the coatings after dry and wet tests were displayed in Fig 4.22.

Samples	Percentage of area removed (dry samples)	ASTM Classification (dry samples)	Percentage of area removed (wet samples)	ASTM Classification (wet samples)
AR2024_SG	20~30%	2B	30~50%	1B
AD2024_SG	10~15%	3B	20~30%	2B
AE2024_SG	0%	5B	<5%	4B
SG_PVB_8	0%	5B	0%	5B
SG_PVB_4	0%	5B	0%	5B
PANI_AP/NMP_PVB	0%	5B	0%	5B
PANI_NF/NMP_PVB	0%	5B	0%	5B
PANI_CB/NMP_PVB	0%	5B	0%	5B
GF001_PVB	0%	5B	0%	5B
GF001_PANI_NF/NMP_PVB	0%	5B	0%	5B

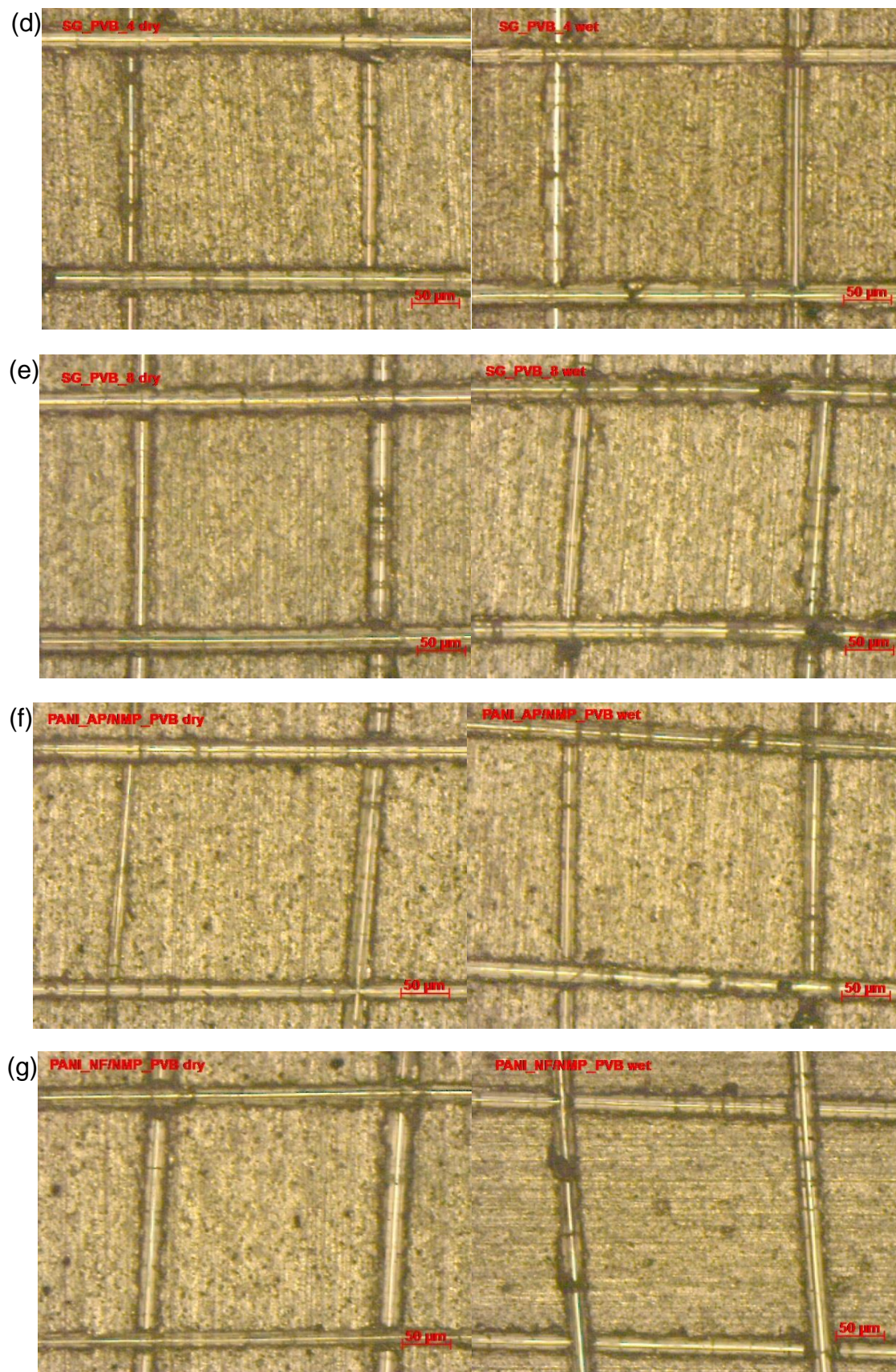
Table 4.1 Cross-hatch adhesion for the surface of bare AA2024 and various sol-gel coatings.

It can be seen from Table 4.1 that standard sol-gel coatings had poor adhesion on the surface of both AR2024 (Fig 4.22 a) and AD2024 (Fig 4.22 b) substrates at dry conditions, with 20~30% and 10~15% percent area removed (highlighted by the red curves in the yellow area), respectively. The sol-gel coatings on these two substrates exhibited further delamination after immersion with an additional 10~20% area been removed, which were evident from the optical images in Fig 4.22 (a, b). However, for sol-gel coatings on AE2024 (Fig 4.22 c), all areas showed good adhesion for dry samples and just less than 5% area was removed for wet samples. This result indicates that good adhesion can be obtained on the surface of AE2024 for sol-gel coatings and AR2024 and AD2024 may not be suitable surfaces from an adhesion point of view. The adhesive failure of AR2024 and AD2024 may stem from the fact that an oxide film remains on the surface of AR2024 or lack of hydroxyl groups in the case of AD2024. The adhesion of the

sol-gel coatings on AE2024 was further improved by the addition of PVB binder in both ratios, clearly shown in Table 4.1 and Fig 4.22 (d, e); as no coating was removed from the surface for both dry and wet samples. The addition of both synthesised PANI agglomerated particles (Fig 4.22 f), and nanofibers (Fig 4.22 g), showed no adverse effects on adhesion properties of the coating, as well as for commercial PANI on carbon black (Fig 4.22 h). Glass flake (Fig 4.22 i) or together with PANI nanofibers (Fig 4.22 j) added in the PVB sol-gel coatings were also showed good adhesion at dry and wet conditions. Fig4.22 (a-j) are displayed in the next three pages.









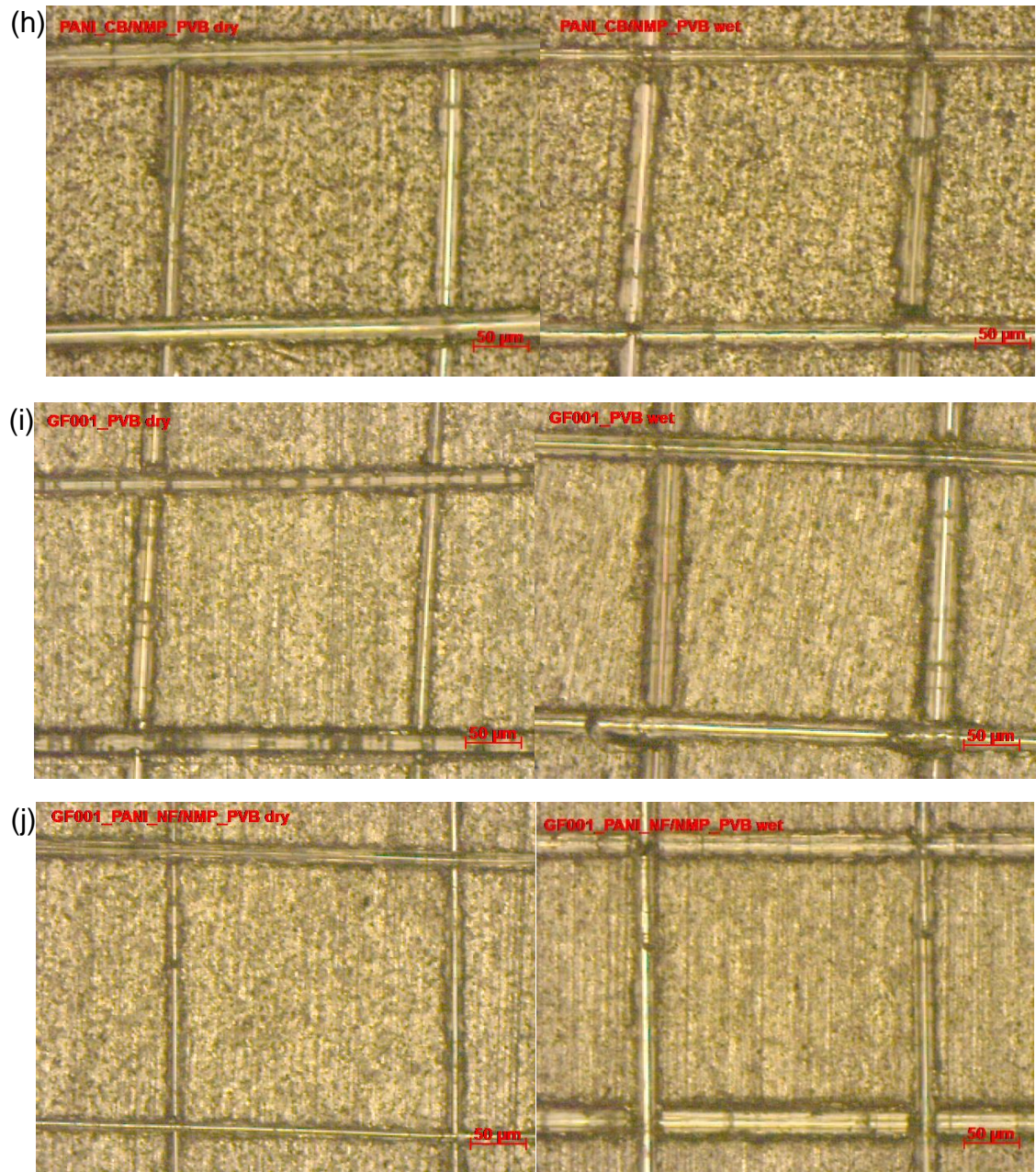


Fig 4.22 Typical optical micrographs showing the condition of all the coatings after cross-hatch adhesion tests at dry (left) and wet (right) environment.

(a) AR2024\_SG; (b) AD2024\_SG; (c) AE2024\_SG; (d) SG\_PVB\_8; (e) SG\_PVB\_4; (f) PANI\_AP/NMP\_PVB; (g) PANI\_NF/NMP\_PVB; (h) PANI\_CB/NMP\_PVB; (i) GF001\_PVB; (j) GF001\_PANI\_NF/NMP\_PVB.

# Chapter 5 Discussion

## 5.1 Preparation of materials

### 5.1.1 Surface pre-treatments of AA2024 alloy

The surface cleaning of AA2024 alloy is typically undertaken for the removal of organic contaminants, native oxide layer and any corrosion product to aid bonding between the deposited sol-gel coatings and the substrates [174]. Acetone degreasing was used for organic contaminants, such as oils and greases. However, the native oxide film still remained on the surface of the substrate. Whilst this is corrosion resistant, it has variable reactivity with the sol-gel, leading to variable adhesion of the applied coatings. Therefore, it is crucial to further treat the alloy with alkaline and/or acid solution to remove the oxide layer and any possible corrosion products.

For the application of AA2024 alloy in aerospace industry, alkaline etching and/or acid desmutting are usually applied for cleaning prior to the deposition of coatings. The native oxide film on the surface of AA2024 is mainly composed of  $\text{Al}_2\text{O}_3$  and  $\text{MgO}$  [175]. During alkaline etching, usually concentrated sodium hydroxide solution,  $\text{Al}_2\text{O}_3$  will dissolve according to equation (5.1), leaving a black 'smut' of loosely bound intermetallic material and magnesium rich oxide film, along with other alkali-insoluble components, such as copper.

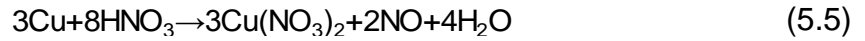
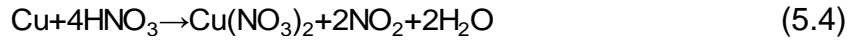


Therefore, it is essential to apply acid pickling, usually concentrated nitric acid, to remove the smut on the surface. The desmutting process will dissolve the  $\text{MgO}$  (equation (5.2)) and/or  $\text{Mg}(\text{OH})_2$  (equation (5.3)) on the surface.

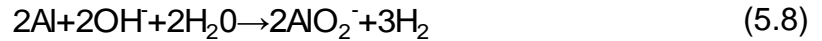


Moreover, the copper on the surface will also be partially removed in concentrated  $\text{HNO}_3$  (e.g. 3M and 50%) according to equation (5.4), (5.5), leaving

a blue solution and clean surface of AA2024. Residual Cu may still be kept after acidic treatment, due either to the replacement of dissolved Cu from alloy matrix by Al (equation (5.6)) or preferentially dissolution of Al matrix (equation (5.7)), which leaves undissolved solid Cu on the surface [171].



It is also important to note that the alloy matrix, typically aluminium, although underneath the oxide film, may still be dissolved during both alkaline etching (equation (5.8)) and acid desmutting (equation (5.7)).



The comprehensive action of all the above processes during traditional alkaline etching and acid desmutting produces a clean, uniform and chemically active surface of AA2024 alloy with suitable texture and smooth appearance, as seen in Fig 4.3 (a, b). If only acid desmutting is applied, the oxide film, being less active in the solution than copper-containing intermetallic particles (IMPs) on the surface, can cause dealloying of IMPs to be initiated followed by dissolution of copper [150]. The preferential dissolution of IMPs in this process would finally produce significant cavities in the surface, as shown in Fig 4.2 b.

### 5.1.2 Synthesis of nanostructured polyaniline

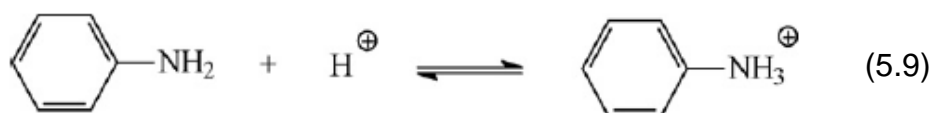
During the synthesis of PANI in this study, the chemical oxidative polymerization of aniline (ANI) in aqueous solution of 1M  $\text{HNO}_3$  with the presence of ammonium persulphate (APS) was successfully used to prepare PANI agglomerated particles and PANI nanofibers via slow-mixing and rapid-mixing methods, respectively.

### 5.1.2.1 Chemical processes during the polymerization of aniline

The behaviour of polyaniline during the oxidative polymerization is generally subject to the basic principles of the polymerization itself. Although it is still debatable for the mechanism of oxidative polymerization of aniline, three classical well defined stages generally describe the chemical process of the formation of PANI from aniline monomers [129, 176].

The polymerization of aniline consists mainly of three stages; initiation, chain propagation and chain termination, according to the mechanism proposed by Wei et al [177].

At initiation stage, nitrenium cations ( $\text{C}_6\text{H}_5\text{NH}^+$ ) or cation-radicals were formed when aniline monomers were dissolved in strong acid (e.g. 1M  $\text{HNO}_3$ ) according to equation (5.9) [6].



During the chain propagation stage, the nitrenium cations in Fig 5.1 (1) were firstly oxidised by the strong oxidant  $(\text{NH}_4)_2\text{S}_2\text{O}_8$  (APS) to produce dimeric oxidized oligomers of p-aminodiphenylamine (PADPA) in Fig 5.1 (5), which served as oxidant to oxidise aniline Fig 5.1 (2) and growing sites to add the monomers (Fig 5.1 path 1) to the chain end via an electrophilic aromatic substitution. The reduced trimers Fig 5.1 (6) were then subject to further oxidation and deprotonation to add aniline to the chain end (Fig 5.1 path 1) and produce tetramers Fig 5.1 (7). Another competitive path was also proposed by Wei et al [177], where the tetramer were directly produced by two dimers Fig 5.1 (3), (5). The redox process from both paths was repeated and leads to the formation of the final product, namely, green long-chain protonated PANI [176].

Termination of the chain growth occurs either by the hydrolysis of amino group at the end of the chain or reaction with some reaction intermediates or completed



chains [129]. One of the typical methods to stop the polymerization is dilute the reaction mixture with a large amount of water.

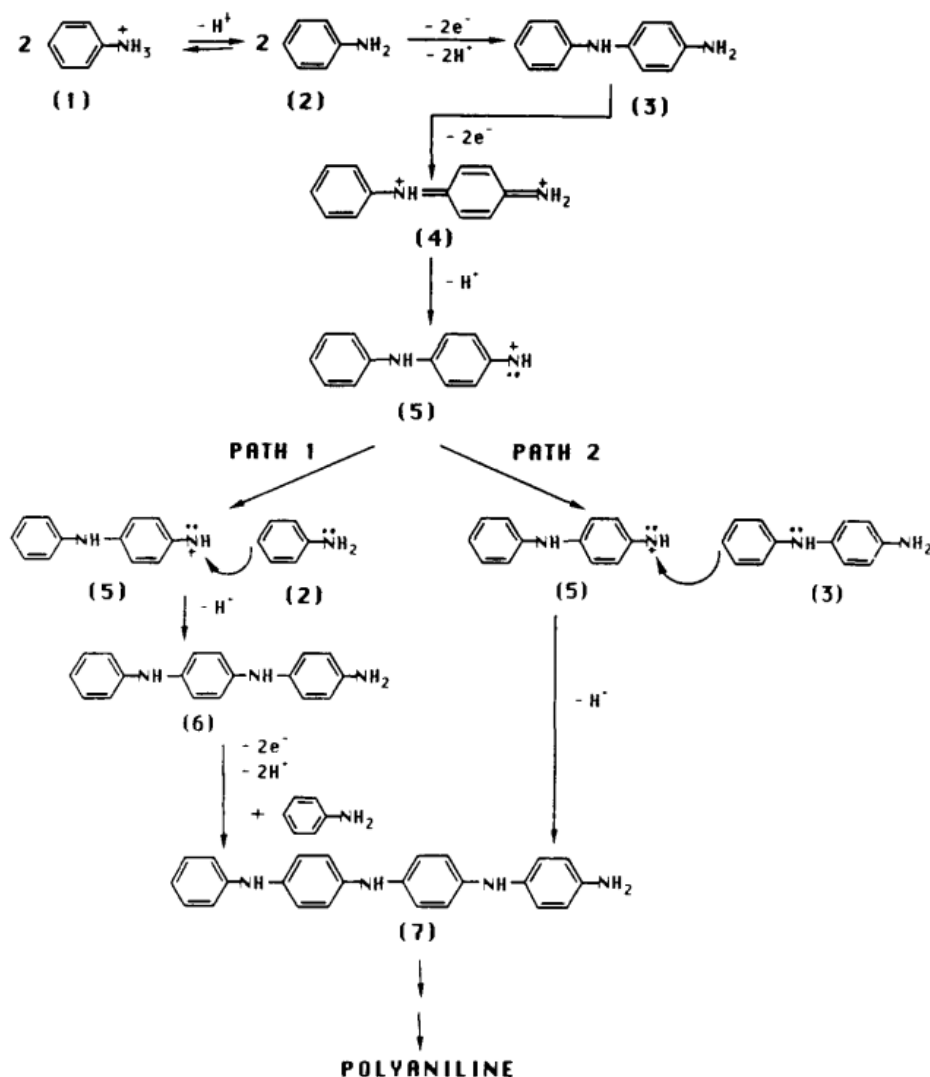


Fig 5.1 Proposed mechanism for polymerization of aniline by Wei et al [177].

#### 5.1.2.2 Formation of different PANI nanostructures

During the preparation of PANI agglomerated particles, the mechanism is attributed mainly to the second growth process of PANI on existing ones via heterogeneous polymerization. Due to the hydrophobic nature of nucleates for polymerization and their limited solubility in water, the nuclei prefer to absorb on the surface of completed PANI and start the growth of new PANI chains [129]. In this case, any further growth of PANI is via heterogeneous nucleation; differing from the PANI formed initially via homogeneous polymerization. These chains then further subject to stacking and agglomeration aided by mechanical stirring.

The agglomeration process is more typical with the presence of either general or local high ratio of aniline monomers to oxidant. Therefore, during the slow mixing method, a local high ratio of aniline to the oxidant cannot be avoided leading to the formation of PANI agglomerated particles as the major nanostructure [103]. However, for the rapid-mixing method, uniform concentration of both the aniline and oxidant was achieved prior to the propagation stage. Therefore, the aniline monomers and oxidant were all consumed at the same time and subject to homogeneous polymerization to form evenly distributed PANI nucleates. In this case, second growth of PANI via heterogeneous nucleation was largely suppressed. The specific conditions applied (monomer/oxidant ratio, temperature, solvent, etc.) then favoured the stacking of these nucleates via  $\pi$ - $\pi$  interactions between the oligomers, leading to perpendicularly growth of PANI chains and produce the body of nanofibers [129]. The uniformity and size of the nanofibers can be varied by many factors, including pH, dopant, temperature, reaction time, monomer/oxidant ratio, oxidant type etc. [95, 104, 178].

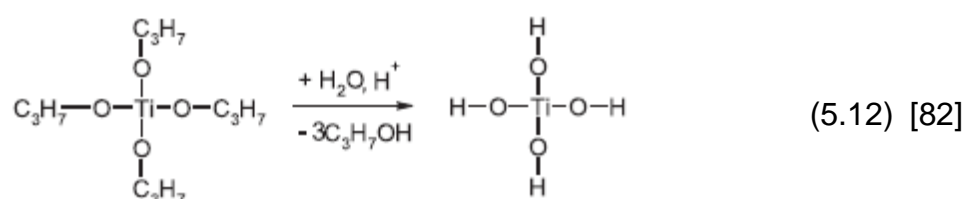
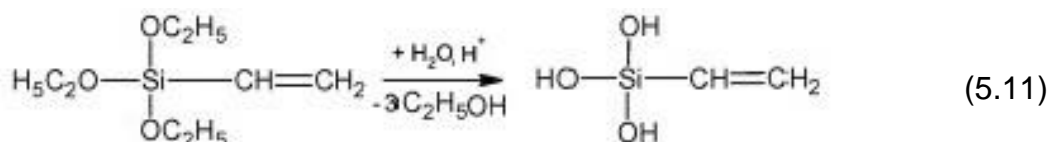
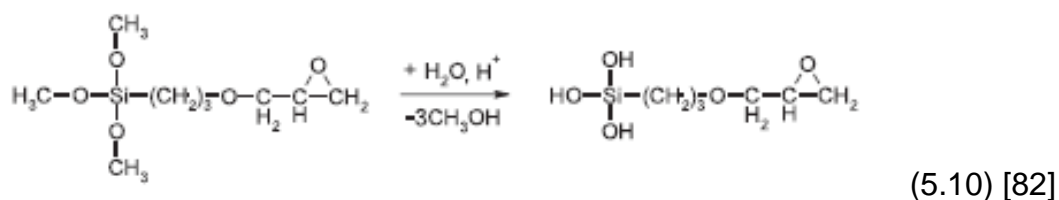
### 5.1.3 Preparation of sol-gel coatings on AA2024

A combination of organic precursor of 3-glycidoxypropyltrimethoxysilane (GPTMS) and vinyltriethoxysilane (VTES) along with inorganic precursor of Titanium (IV) isopropoxide (TIP) was successful in preparing a hybrid titania-containing sol-gel coating in this study. This system is denoted as the 'standard sol-gel' system with an atomic molar ratio of Si:Ti=4:1.

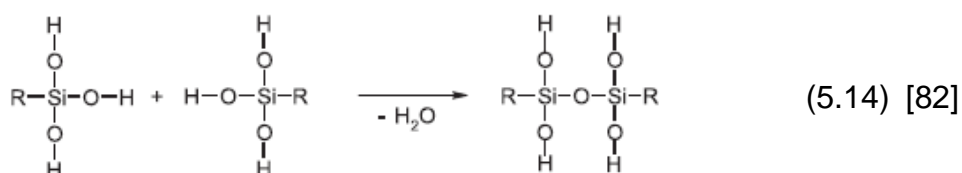
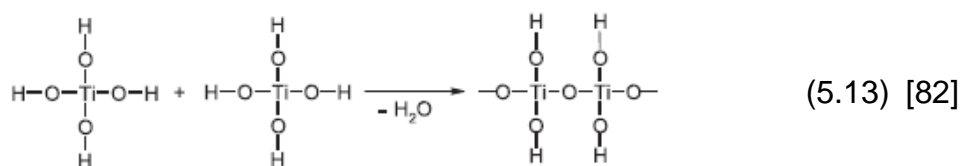
During the preparation of standard sol-gel coatings, four well-defined steps take place, including hydrolysis, condensation and aging during the preparation of sol-gels along with curing process in the deposition of coatings.

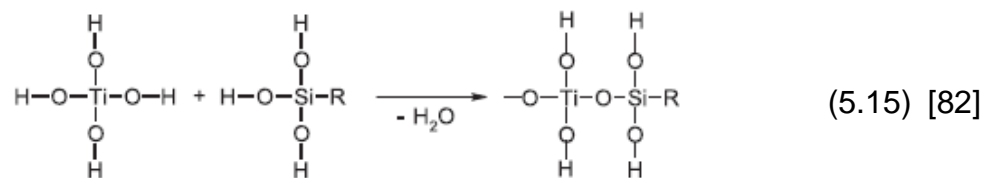
Upon the addition of water, the hydrolysis of organic precursors of GPTMS (equation (5.10)) and VTES (equation (5.11)), as well as inorganic precursor of TIP (equation (5.12)) will be initiated, accompanied by the removal of alcohol and

formation of hydroxyl groups. In the hydrolysis of both organic and inorganic precursors, acidified water was used as the catalyst and ethyl acetoacetate (AcEt) was added as a complexing agent to control the reactivity of TIP.

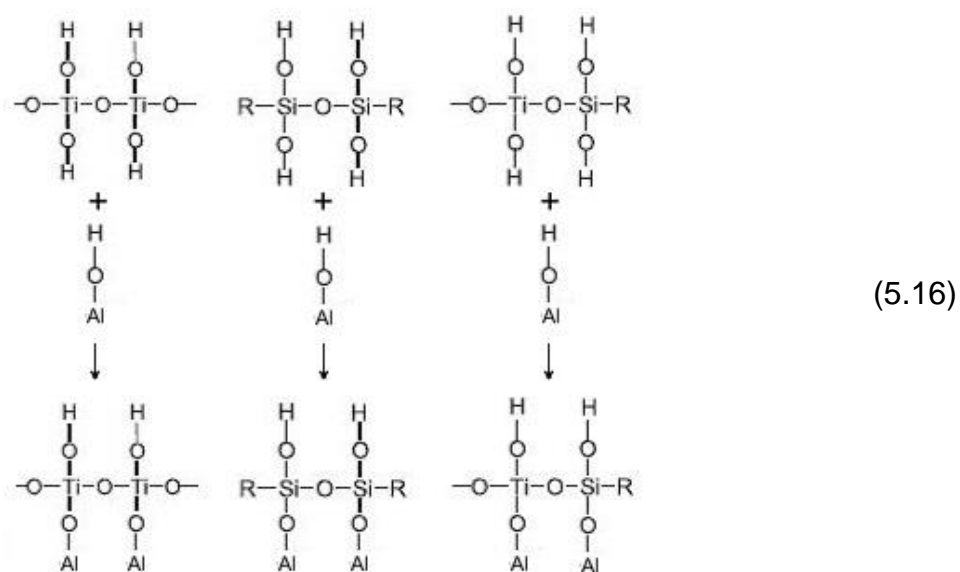


Two types of process were involved during the condensation stage, notably, homo-condensation between the same hydroxylated species (equation (5.13), (5.14)) and heter-condensation between the different ones (equation (5.15)). Moreover, the relatively slow condensation process of organic species would be accelerated by inorganic species [179]. Thus, with a combination of saline and metal alkoxides, a significant degree of condensation can be achieved within a short time for hybrid sol-gels.





During the deposition of sol-gel coatings on AA2024, a reaction usually occurs between the alloy surface and sols, due to the acidic nature of the sols. This results in the formation of an intermediate layer [39], according to equation (5.16). During the curing of the sol-gel coating, residual alcohol and water produced during the hydrolysis and condensation stages will evaporate, leading to the gelation and shrinkage of the sol-gel coating. It is important to note that the structure of the intermediate layer is dense and significant from the porous nature of the sol-gel coating body.



#### 5.1.4 Modification of the standard sol-gel coatings

The standard sol-gel coating has limited anticorrosive performance and were therefore modified by adding additional components, for example, a co-polymer of polyvinyl butyral (PVB), a conductive polymer of polyaniline (PANI) and/or corrosion resistance glass flake (GF) to obtain improved corrosion protection. However, the addition of these organic or inorganic components influences the

properties of the standard sol-gel coating, i.e., thermal and chemical properties. Thus, possible effects on the addition of these components are discussed.

#### 5.1.4.1 Influence on thermal properties

To study whether thermal stability was still achieved using a fixed curing temperature at 120°C for 2 hours, DSC/TG analysis was performed on xerogel samples, which were produced as described in section 3.2.3. Fig 5.2 showed the DSC/TG curves for a standard sol-gel, a PVB\_4 sol-gel, a PANI\_NF/NMP\_PVB sol-gel and a GF001\_PVB modified sol-gel.

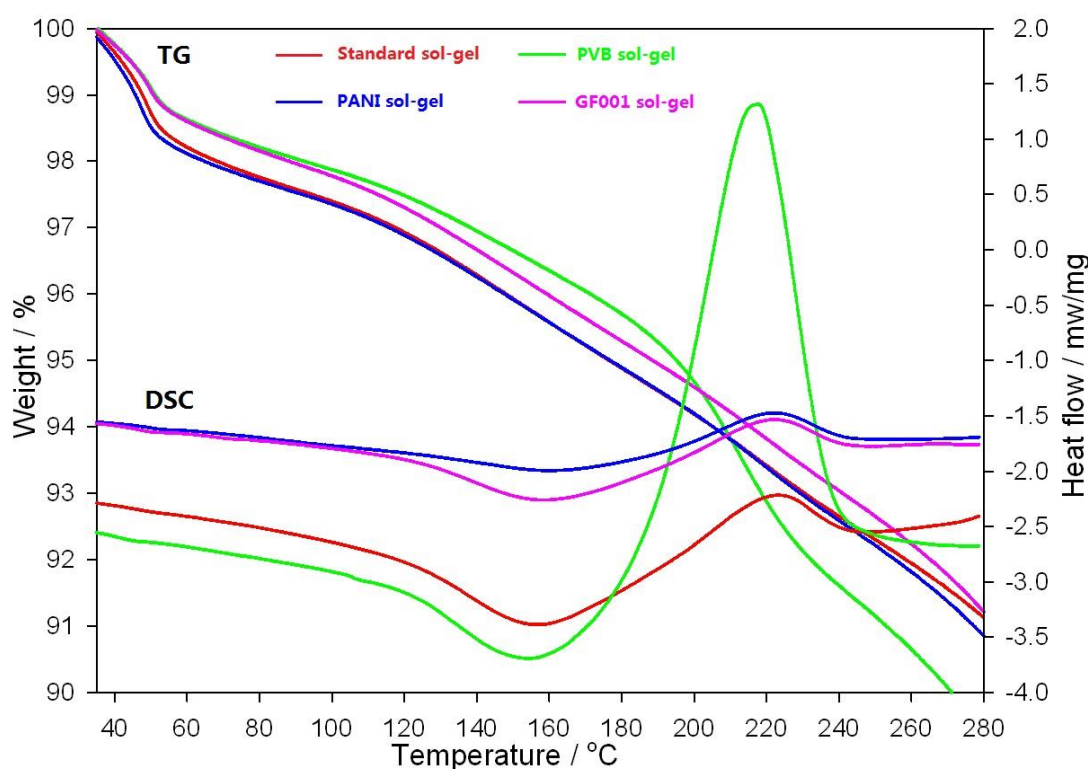


Fig 5.2 DSC/TG curves for standard sol-gel and PVB, PANI, GF001 modified sol-gel.

It was clear from TG curves that an initial steep weight loss occurred at 35~50°C, with similar glass transition points between 50~60°C for all four sol-gels. The weight loss during this stage may be due to the loss of residual alcohol within the sol-gels [180]. Four similar broad endothermic peaks were observed between 120 and 200°C for all sol-gels, with simultaneous small weight loss. These processes can be ascribed to the desorption of physically absorbed water molecules [181]. A sharp exothermic peak and increased weight loss was

observed for the PVB sol-gel coating between 180 to 240°C, in comparison to minor changes in the other three sol-gels. The exothermic reaction may be attributed to the elimination of chemically bonded water from the sol-gel network [182]. From the DSC/TG curves, it seems that PVB modified sol-gel are less thermally-stable than the standard sol-gel. However, when PANI or GF001 is added into the PVB modified sol-gel, the thermal stability improves over that of the standard and PVB modified sol-gels. This may due to the more complete hydrolysis and condensation reactions introduced to the PVB modified sol-gel coatings by PANI or GF001 [181]. Moreover, as the modified sol-gels were all thermally stable at 120°C, the chosen cure temperature is considered suitable for curing modified sol-gel coatings.

#### 5.1.4.2 Influence on chemical bonding

The modification using the various pigments, especially the PVB polymer, may affect the hydrolysis and condensation process for the standard sol-gels. This is mainly related to interaction with the bonds of Si-O-R, Si-OH and Si-O-Si, which were generated due to incomplete hydrolysis, incomplete condensation and complete condensation, respectively. The FTIR technique was therefore used to investigate the influence of pigments on the chemical bonding properties of the standard and modified sol-gel coatings. Typical FTIR spectra are presented in Fig 5.3, where characteristic peaks were highlighted. Four of the sol-gel coatings were the same as those tested during the TG/DSC measurements. An additional coating, GF001\_PANI\_NF/NMP\_PVB, was also tested.

Firstly, Si-OH bonds were characterized by the absorption band at 3269 cm<sup>-1</sup> and 904 cm<sup>-1</sup>, which were assigned to hydrogen-bonded Si-OH and Si-OH stretching vibration, respectively [183-192]. A shoulder of absorption peak at 2919 and 2853 cm<sup>-1</sup> were related to symmetric and asymmetric stretching vibrations of C-H [184, 193]. The absorption bands at 2358 and 2335 cm<sup>-1</sup> were ascribed to environmental noise of carbon dioxide [194, 195].

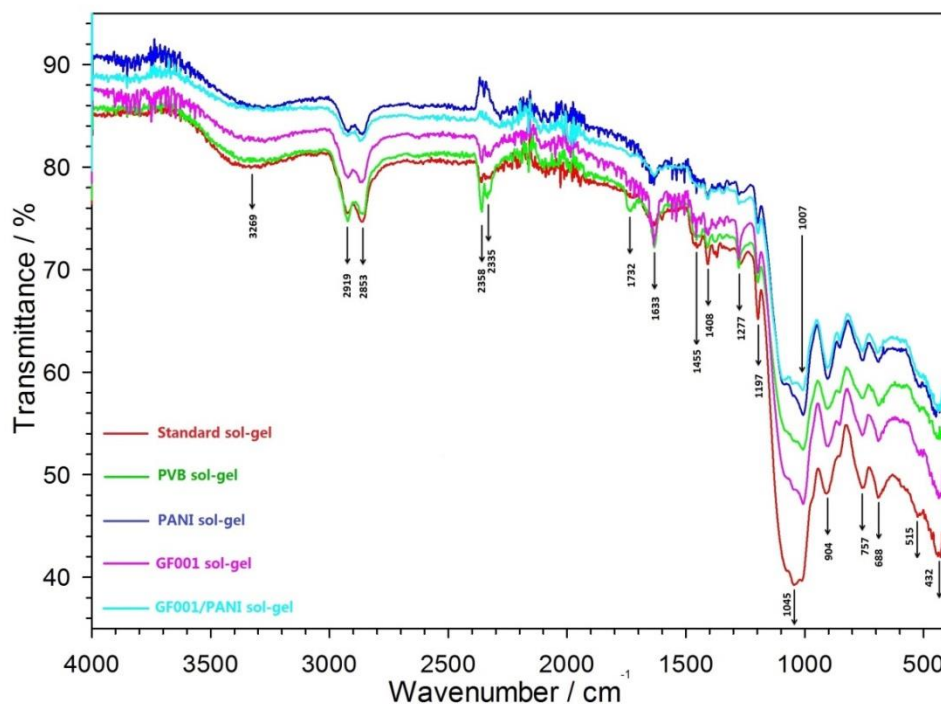


Fig 5.3 FTIR spectra of standard sol-gel coating and PVB, PANI, GF001, GF001/PANI modified sol-gel coatings

A relatively strong peak at  $1732\text{ cm}^{-1}$  indicated the appearance of the ester linkage, which was associated with the PVB coating [196-200]. The three weak bands at  $1455$ ,  $1408$  and  $1277\text{ cm}^{-1}$  were assigned to asymmetric bending of  $\text{CH}_3$ , symmetric and asymmetric stretching vibration of the  $\text{CH}_3$  group in  $\text{Si-CH}_3$ , respectively [201-208]. The strong peaks at approximately  $1045$  and  $1007\text{ cm}^{-1}$  were related to the asymmetric Si-O-Si bending [186, 187, 189, 209]. Symmetric Si-O-Si bending [43-46] and Si-O-Si rocking were characterized at the absorption bands of  $757$  and  $432\text{ cm}^{-1}$  [187, 188, 190, 210, 211], respectively. C-Si from Si-Me bands were located at the absorption of  $688\text{ cm}^{-1}$  [212, 213]. At  $1633\text{ cm}^{-1}$ , O-H bending vibrations of the hydroxyls, which may from absorbed water or alcohol, were observed [214, 215]. The absorption peak at  $1197\text{ cm}^{-1}$  was attributed Si-O- $\text{CH}_3$  groups, which may due to the incomplete hydrolysis of the silicon alkoxide precursors [183, 184]. The small peaks at around  $515\text{ cm}^{-1}$  were assigned to the presence of Titanium oxide [189, 216]. A summary of assignments for the peaks is listed in Table 5.1.

Wavenumber/cm <sup>-1</sup>	Assignments	References
3269, 904	Si–OH groups (hydrogen-bonded/stretching vibration)	[183-192]
2919, 2853	Stretching vibrations of C-H (symmetric/asymmetric)	[184, 193]
2358, 2335	Carbon dioxide	[194, 195]
1732	C=O stretching from the ester linkage	[196-200]
1633	O–H bending vibrations from water and hydroxyls	[214, 215]
1455	Asymmetric bending CH <sub>3</sub>	[201, 202]
1408, 1277	Stretching vibration of the CH <sub>3</sub> group in Si–CH <sub>3</sub> (symmetric/asymmetric)	[201-208]
1197	Si-O-CH <sub>3</sub> from silicon alkoxide precursors	[183, 184]
1045, 1007	Asymmetric Si-O-Si bending	[186, 187, 189, 209]
757	Symmetric Si-O-Si bending	[43-46]
688	Si-C from Si–Me	[212, 213]
515	Titanium oxide	[189, 216]
432	Si-O-Si rocking	[187, 188, 190, 210, 211]

Table 5.1 Assignments for the peaks highlighted in the FTIR spectra of sol-gel coatings.

Beer's law may be applied, qualitatively, to determine the relative concentration of the bands from the FTIR spectra obtained. When just taking the difference of samples into account, it can be concluded, to some extent, that the lower the transmittance, the higher the absorbance and concentration of the band or compound from equation (5.17).

$$A = - \log_{10} \frac{\%T}{100} = \epsilon bc \quad (5.17)$$

Where

A is absorbance;

%T is transmittance;

$\epsilon$  is absorptivity coefficient (L·mol<sup>-1</sup>·cm<sup>-1</sup>);

b is the path length of the sample (cm);

c is the concentration of the absorber (mol·L<sup>-1</sup>).

Applying equation (5.17) implies low concentrations of Si-O-Si at 1007 cm<sup>-1</sup> and Si-O-CH<sub>3</sub> at 1197 cm<sup>-1</sup> in all the modified coatings when compared to the standard coating. However, as both these bands were due to the complete



condensation and incomplete hydrolysis processes [184], respectively. The lower concentration of both bands within the modified coatings appears to be contradictory. A possible reason may arise from the red-shift of Si-O-Si band from 1045 to 1007  $\text{cm}^{-1}$ , which may indicate that the Si-O-Si band was weakened following modification of the standard coating [217]. If it was true as estimated, the weakening of Si-O-Si bands after modification should have been introduced by the hydroxyl groups in PVB due to the formation of Si-O-C. This explanation may be reasonable based upon the presence of red-shifted Si-O-Si bands in all the modified coatings, which were basically modified by the introduction of PVB. However, the application of FTIR alone is insufficient to obtain a precise and correct conclusion on whether or not the introduction of PVB would weaken the Si-O-Si bands or not. Advanced characterization techniques, such as X-ray photoelectron spectroscopy, would need to be applied to check the behaviour of Si-O-Si and Si-O-C as well as Si-O-Ti and Ti-O-Ti bonds within the modified coatings. Due to time limitations during the study, this aspect is considered as future work.

## 5.2 Corrosion performance

### 5.2.1 Bare AA2024

From a corrosion point of view, both bare AR2024 and AD2024 were more resistant to corrosion, having an oxide film providing effective barrier protection [158], compared with bare AE2024, whose original oxide film was removed during the cleaning processes. From the analysis of the EIS data obtained during the immersion of bare AA2024 in 3.5% NaCl solution, two typical equivalent electrical circuits (EEC) can be used for numerical fitting as depicted in Fig 5.4 [35, 161, 218].

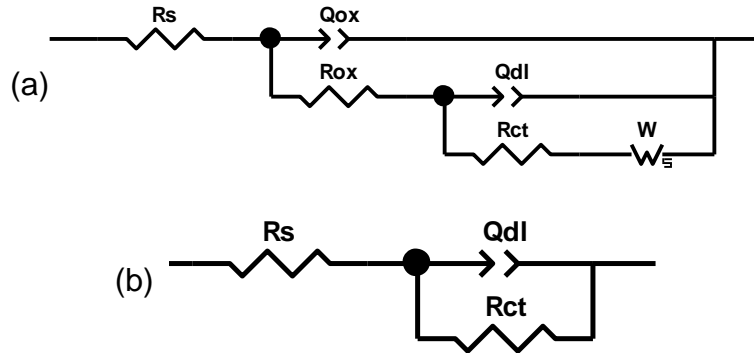


Fig 5.4 Two typical EECs used for the simulation of bare AA2024 immersed in 3.5% NaCl solution.

In both EECs,  $R_s$  is the resistance of the solution;  $R_{ox}$  is the resistance of the native oxide layer;  $R_{ct}$  is the charge transfer resistance and  $W$  is the finite length Warburg element. Constant phase elements (CPE) are used instead of pure capacitances.  $Q_{ox}$  is the capacitance of the oxide film and  $Q_{dl}$  is the capacitance of the double layer. The capacitance values can be calculated from the CPE capacitances using the following equation (5.18) [219]:

$$C = Q (\omega_{max})^{n-1} \quad (5.18)$$

Where

$Q$  is the parameter of fitting capacitance ( $\Omega^{-1} \cdot \text{cm}^{-2} \cdot \text{s}^n$ );

$\omega_{max}$  is the frequency where the imaginary impedance reaches a maximum for the respective time constant.

It is important to note that these proposed parameters in the EECs were related to the real components between the working electrode and reference electrode. Nyquist plots of bare AA2024 alloy in 3.5% NaCl solution are given in Fig 5.5 for 1 hour, 1 day and 8 days immersion. From the Nyquist plots, well-defined Warburg elements can be observed for the three substrates during the initial immersion, during which chloride ions attack the native oxide film and lead to its breakdown at the sites of intermetallic particles (IMPs) leading to dissolution of Al and Mg. Corrosion product of  $\text{Al}(\text{OH})_4^-$  complex ions were then produced (equation (5.19)) from the reaction between aluminium cations and hydroxyl ions, which were from anodic dissolution of aluminium (equation (5.20)) in IMPs and

hydroxyl ions from cathodic oxygen reduction (equation (5.21)), respectively. The diffusion of  $\text{Al}(\text{OH})_4^-$  from the surface of AA2024 to the bulk solution may be responsible for the presence of Warburg elements during the initial immersion of bare AA2024.

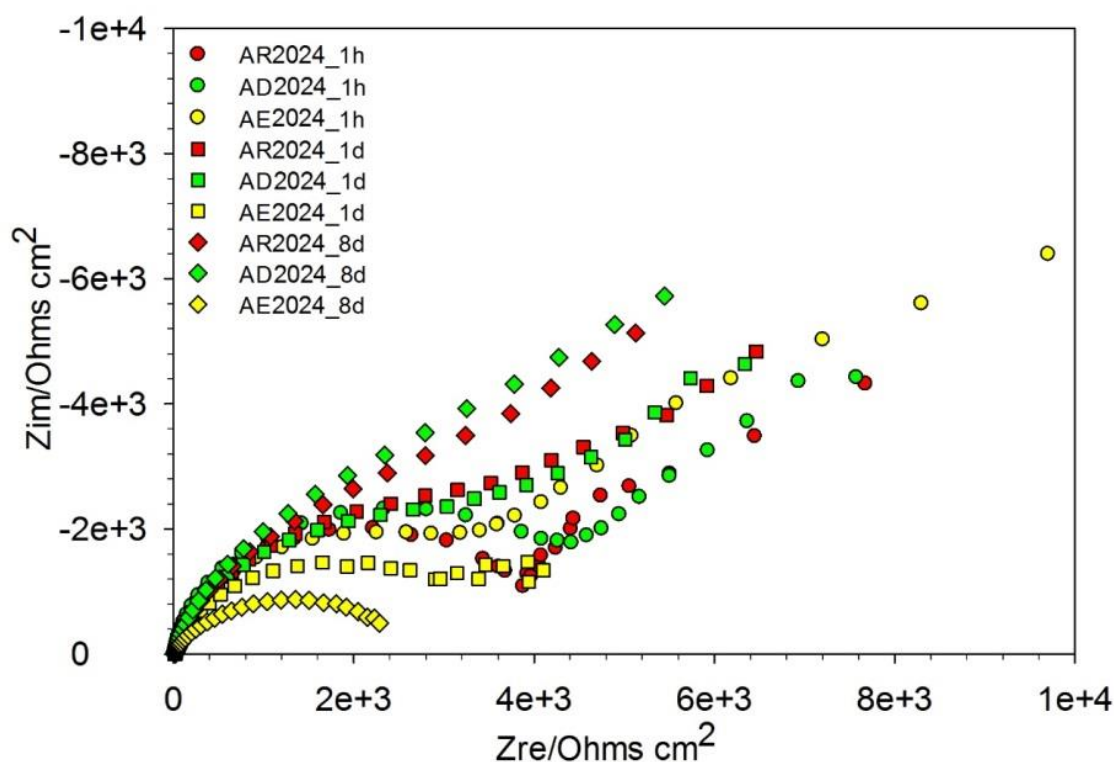


Fig 5.5 Nyquist plots of bare AA2024 alloy in 3.5% NaCl solution during 1 hour, 1 day and 8 days immersion for AR2024, AD2024 and AE2024.

The equivalent circuit displayed in Fig 5.4 (a) appears reasonable for fitting these EIS results.



However, the Warburg element begins to disappear after 1 day immersion and has completely disappeared after 8 days for the AE2024 substrate, in comparison to AR2024 and AD2024 where little change is observed. The EEC in Fig 5.4 (b)

is therefore appropriate for fitting the EIS data of AE2024 after 1 day immersion for AE2024 and Fig 5.4 (a) is appropriate for the other two substrates.

According to Zheludkevich et al [51], the presence of porous honeycomb-like structured copper-rich aggregates (Fig 5.6), which are formed during the dealloying process and redeposition of copper, may provide a diffusion pathway for electrolyte and corrosion products in pits. This explanation may be reasonable as the copper on the surface of AE2024 was partially dissolved during the second step of alkaline cleaning in 50% HNO<sub>3</sub>, whilst 30% HNO<sub>3</sub> may not be sufficiently concentrated for dissolving Cu during the acid desmutting applied to AD2024. Therefore, the presence of Warburg elements in the EECs of both the AR2024 and AD2024 may be directly ascribed to the formation of redeposited porous Cu remnants.

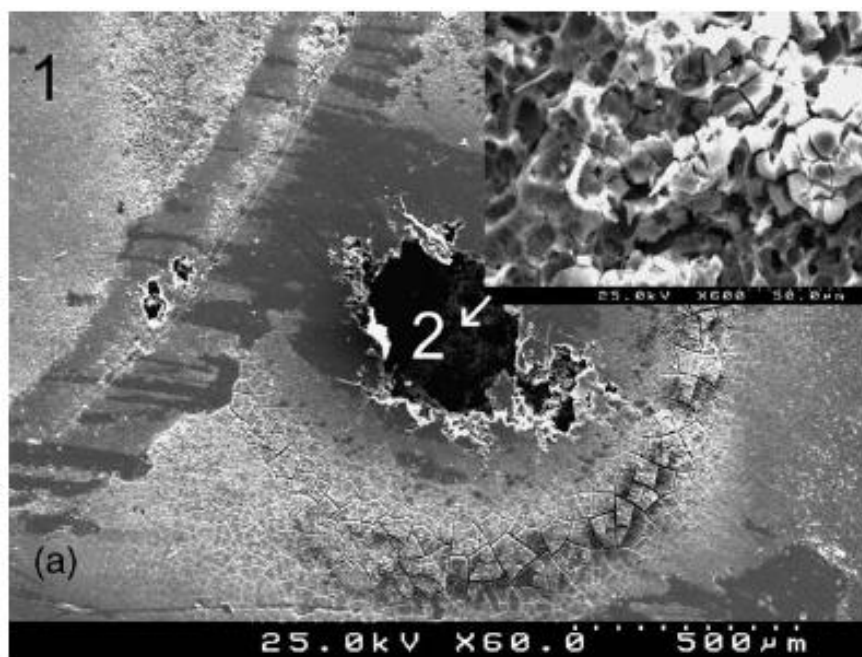


Fig 5.6 SEM image of pits on AA2024 (Insert is Cu-rich aggregate) [51].

To conclude, it is clear that the severe pitting corrosion (Fig 4.9) and low impedance magnitude (Fig 4.8) of bare AA2024 in 3.5% NaCl solution indicate that the material cannot be used without a protective coating. Due to the native oxide layer on the surface, AR2024 and AD2024 were more corrosion resistant in 3.5% NaCl solution than AE2024, whose oxide layer was reduced during the

cleaning process. Moreover, Cu-rich IMPs were still preserved on the surface of AR2024, AD2024 and AE2024.

## 5.2.2 Standard sol-gel coatings

To analyse the corrosion performance of the standard sol-gel coated AA2024 in 3.5% NaCl solution, Nyquist plots were obtained for 1, 8 and 24 hours immersion, as shown in Fig 5.7. It can be seen that a diffusion-induced Warburg element was no longer observed for AE2024\_SG at any time. Thus the suggested EEC for the AE2024\_SG is that shown in Fig 5.8 (a) [40, 51, 79]. For AR2024\_SG and AD2024\_SG, the Nyquist plots, on initial immersion, were similar to that of AE2024\_SG, indicating the same EEC could be used as shown in Fig 5.8 (a). However, Warburg elements started to appear at 8 hours for AD2024\_SG and AR2024\_SG, indicating the EEC in Fig 5.8 (b) was more appropriate to fit the EIS data [51, 220, 221].

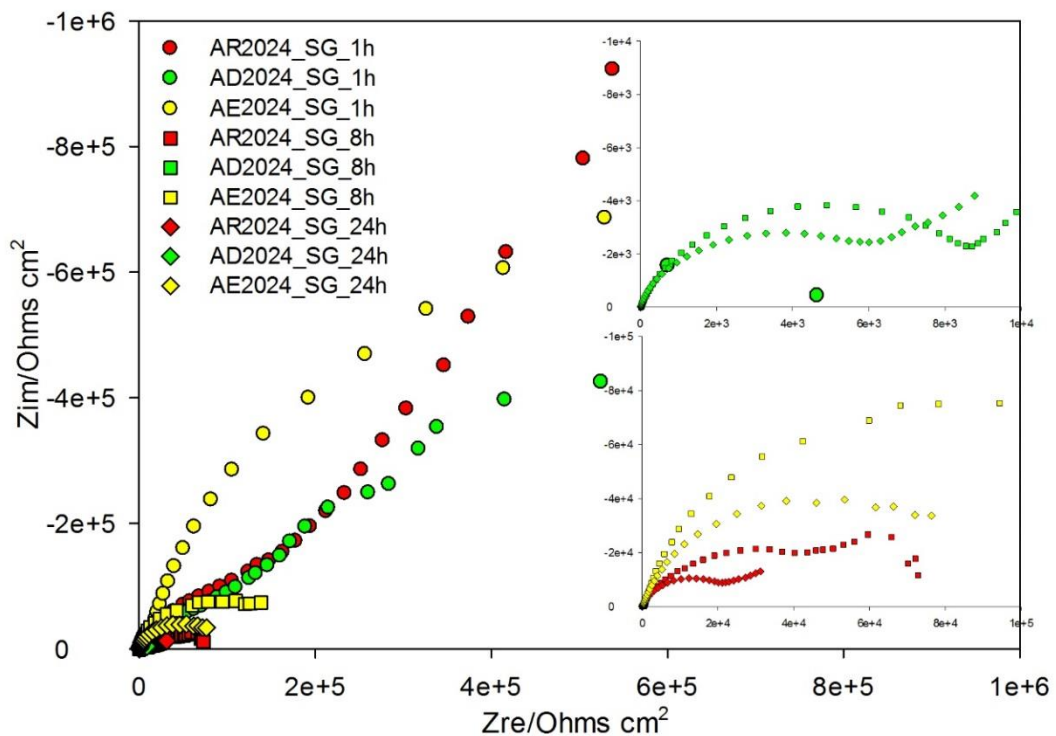


Fig 5.7 Nyquist plots of standard sol-gel coated AA2024 in 3.5%NaCl solution during 1, 8 and 24 hours immersion for AR2024\_SG, AD2024\_SG and AE2024\_SG.

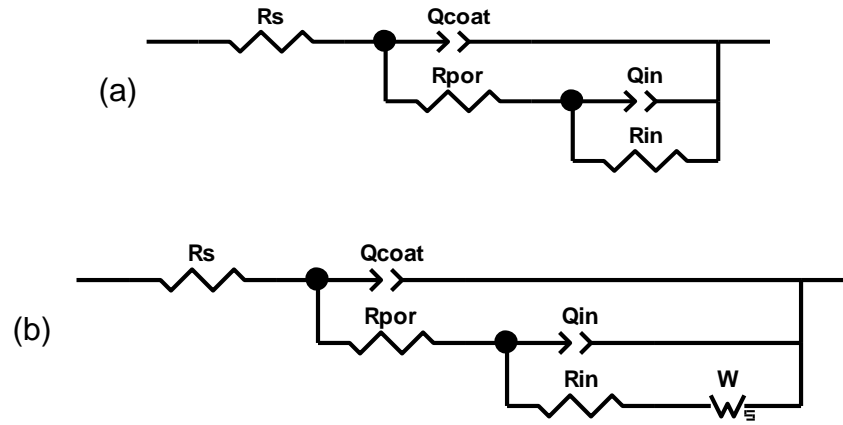


Fig 5.8 Two typical EECs used for the analysis of sol-gel coated AA2024 immersed in 3.5% NaCl solution.

In both EECs,  $Q_{coat}$  is the coating capacitance due to the dielectric nature of sol-gel coating;  $R_{por}$  is the pore resistance from the conductive electrolyte in the sol-gel network,  $C_{in}$  and  $R_{in}$  are capacitance and resistance of the intermediate layer formed by Al-O-Si and Al-O-Ti covalent bonds or with a combination of the native oxide layer on the alloy surface.  $W$  is the finite length Warburg element. The parameters of these components are listed in Table 5.2 after numerical fitting with the EIS data during 1, 8 and 24 hours immersion.

Sol-gel coating	AR2024_SG			AD2024_SG			AE2024_SG		
Immersion time (hour)	1	8	24	1	8	24	1	8	24
Goodness ( $10^{-3}$ )	3.03	0.39	0.93	4.37	3.08	1.84	0.62	2.73	5.25
$R_s$ ( $\Omega \cdot \text{cm}^2$ )	12.6	10.8	10.2	5.2	7.7	6.2	19.7	22.6	15.7
$Q_{coat}$ ( $\text{nS} \cdot \text{cm}^{-2}$ )	148	1668	3838	236	4472	6980	49	1974	4008
$n_{coat}$	0.87	0.80	0.86	0.89	0.87	0.95	0.83	0.81	0.80
$R_{por}$ ( $\Omega \cdot \text{cm}^2$ )	37435	174	83	34089	459	29	17660	345	148
$Q_{in}$ ( $\mu\text{S} \cdot \text{cm}^{-2}$ )	2.0	3.6	8.1	2.3	3.9	13.0	1.3	2.1	4.0
$n_{in}$	0.73	0.78	0.86	0.56	0.91	0.86	0.89	0.84	0.85
$R_{in}$ ( $\text{k}\Omega \cdot \text{cm}^2$ )	12380	42	19	11240	17	6	7252	234	103
$W_R$ ( $\text{k}\Omega \cdot \text{cm}^2$ )		22.8	11.8		40.8	28.1			
$W_Q$ ( $\mu\text{S} \cdot \text{cm}^{-2}$ )		6.1	12.5		342.3	377.7			
$W_n$		0.5	0.5		0.5	0.5			

Table 5.2 Parameters of standard sol-gel coated AA2024 system after fitting the EIS data with different EECs.

It can be seen from Table 5.2 that both EECs showed a good fit with the EIS data. The evolution of parameters related with sol-gel layer, namely  $Q_{coat}$  and  $R_{por}$ , were similar for the three systems. Due to its porous nature, the sol-gel layer has low resistance to electrolyte diffusion and become saturated by electrolyte almost

about 24 hours, as the close value of  $R_{por}$  to  $R_s$ . The differences between the three coatings were mainly from the parameters of intermediate layer. It is clear that the increase in values of capacitance ( $Q_{in}$ ) and decrease in resistance ( $R_{in}$ ) of the intermediate layer for AE2024\_SG were more mild, compared with those for AR2024 and AD2024, indicating the intermediate layer was more stable on AE2024, whilst was fast degraded on the other two substrates.

From the evolution of Nyquist plots together with corresponding evolution of fitting parameters at different immersion stages, it can be concluded that the reason why degradation of the sol-gel coatings on both AR2024 and AD2024 was much faster than AE2024 may be directly attributed to the intermediate layer between the coating and substrate, as the variation of sol-gel properties was small to take into account. The intermediate layer formed in AE2024\_SG, which was made of Al-O-Si and Al-O-Ti covalent bonds from chemical reactions and/or with partial native oxide layer of  $Al_2O_3 \cdot H_2O$  [222], was more stable than those on AR2024\_SG and AD2024\_SG, which mainly consist of native oxide of MgO and/or  $Al_2O_3$ .

It has also been shown from the adhesion tests (Table 4.1 and Fig 4.22) that good adhesion can be achieved for AE2024\_SG. This may be attributed to the chemically active surface of AE2024 with the presence of residual hydroxyl ions [163, 223] and/or the roughness [224, 225] achieved of the surface after alkaline cleaning process, both of which considerably and consistently improved the adhesion strength with the sol-gel coating. Conversely, the sol-gel coatings were very easily delaminated from the AR2024 and AD2024 substrates, which is adverse for the long term durability and integrity of the deposited sol-gel coatings [171].

More regular pitting corrosion was observed on AE2024\_SG than that observed on the other two systems, see Fig 4.12 (b). A Warburg element was also absence from the Nyquist plots (Fig 5.7) for AE2024\_SG. These two findings imply that

the intermediate layer formed in AE2024\_SG was more uniform and denser than the porous oxide layer on the other two substrates.

In summary, improved corrosion protection performance was achieved by the standard sol-gel coating on AE2024 rather than AR2024 and AD2024, due to the uniform, dense and effectively bonded intermediate layer between the coating and AE2024. Both the acetone degreasing and acid desmutting may not be suitable cleaning procedures prior to the deposition of the sol-gel coating, due to the fact that porous native oxide layer will introduce poor intermediate layer, quick delamination of patchy coating and subsequent limited corrosion protection.

### 5.2.3 PVB modified sol-gel coatings

As the porous nature of standard sol-gel coatings allows electrolyte to saturate the coatings within about 24 hours, PVB was added to increase the cross-linking properties and produce denser films. For discussion of the corrosion protection performances of these PVB modified coatings, numerical fitting of the EECs was conducted.

The Nyquist plots of both SG\_PVB\_8 and SG\_PVB\_4 coatings are given in Fig 5.9 for 1 hour, 1 day and 4 days immersion in 3.5% NaCl solution. As the absence of diffusion-induced Warburg element on standard sol-gel coatings, the EEC in Fig 5.8 (a) may still be used for fitting EIS data of PVB modified coatings, which is also clear from the Nyquist plots in Fig 5.9.

The EIS fitted parameters obtained from the PVB modified coatings are listed in Table 5.3. Using the EEC in Fig 5.8 (a) exhibited a good fit for both modified coatings. Compared with the parameters of standard sol-gel coating on AE2024, it is clear that after PVB modification, significant increases of pore resistance ( $R_{por}$ )



and decrease of coating capacitance ( $Q_{\text{coat}}$ ) were obtained for SG\_PVB\_4, indicating that this modified coating was more resistant to electrolyte attack.

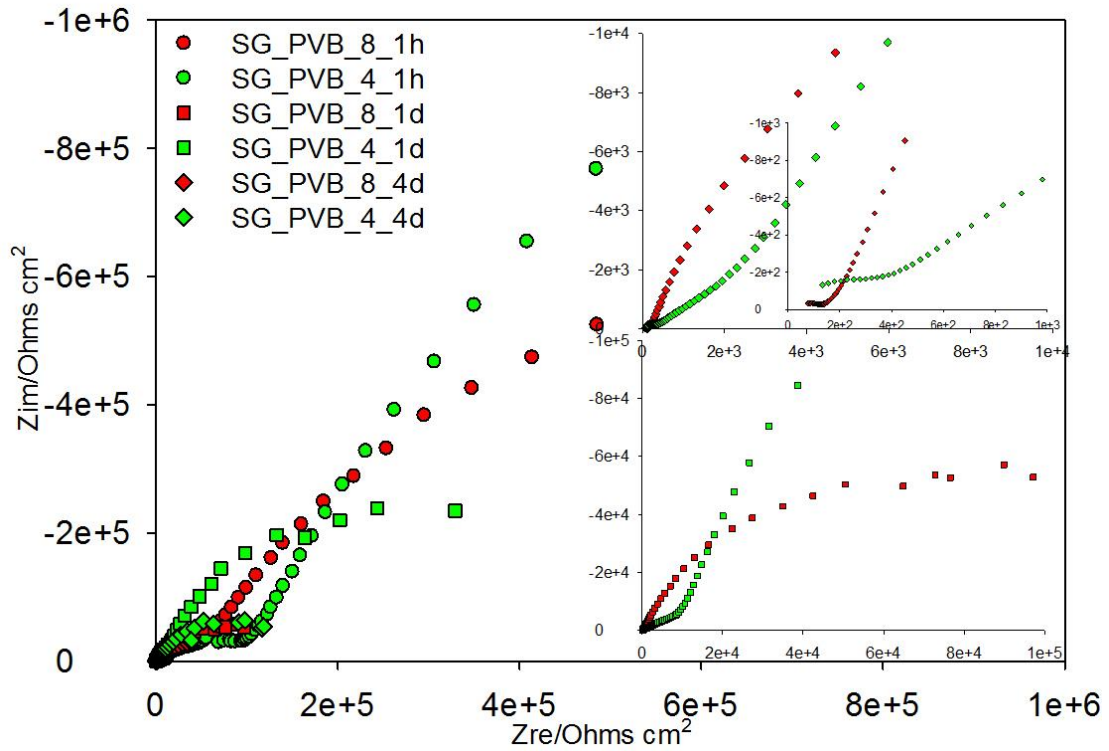


Fig 5.9 Nyquist plots of PVB modified sol-gel coated AA2024 in 3.5%NaCl solution for 1 hour, 1 day and 4 days immersion.

However, for low ratio of PVB in SG\_PVB\_8, no improvement in the coating capacitance were obtained and it seems that this coating was quickly saturated by electrolyte within 24 hours, whilst SG\_PVB\_4 was still not saturated after 96 hours. With regard to the parameters of intermediate layer capacitance ( $Q_{\text{in}}$ ) and resistance ( $R_{\text{in}}$ ), which are related to the stability of intermediate layer, it was found that no obvious improvement was achieved by SG\_PVB\_8, when comparing the parameters of standard sol-gel coating. However, the values of  $Q_{\text{in}}$  and  $R_{\text{in}}$  in SG\_PVB\_4 were preserved at lower and higher level than those in AE2024\_SG, indicating that some improvement may be achieved by the addition of PVB.

It may therefore be concluded that the improvement in corrosion protection performance of PVB modified sol-gel coatings can be associated with both denser sol-gel layers, which have higher resistance to the permeability of the

electrolyte than that of the unmodified coating. Also a more stable intermediate layer is formed between the sol-gel coating and substrate as reflected in an increase of adhesion strength after PVB modification (see adhesion test results in Table 4.1 and Fig 4.22).

Sol-gel coating	AE2024_SG			SG_PVB_8			SG_PVB_4		
Immersion time (hour)	1	8	24	1	24	96	1	24	96
Goodness ( $10^{-3}$ )	0.62	2.73	5.25	1.84	2.25	2.59	6.55	2.36	1.82
$R_s$ ( $\Omega \cdot \text{cm}^2$ )	19.7	22.6	15.7	32.3	21.9	27.8	25.8	48.1	46.7
$Q_{\text{coat}}$ ( $\text{nS} \cdot \text{cm}^{-2}$ )	49	1974	4008	137	1122	4541	48	975	1795
$n_{\text{coat}}$	0.83	0.81	0.80	0.72	0.70	0.58	0.80	0.69	0.64
$R_{\text{por}}$ ( $\Omega \cdot \text{cm}^2$ )	17660	345	148	43068	167	142	93867	9174	804
$Q_{\text{in}}$ ( $\mu\text{S} \cdot \text{cm}^{-2}$ )	1.3	2.1	4.0	1.5	8.3	22.7	2.3	2.8	7.7
$n_{\text{in}}$	0.89	0.84	0.85	0.81	0.80	0.78	0.83	0.72	0.66
$R_{\text{in}}$ ( $\text{k}\Omega \cdot \text{cm}^2$ )	7252	234	103	18260	188	104	19063	1836	356

Table 5.3 Parameters of standard and PVB modified sol-gel coated AA2024 system after fitting the EIS data with different EEC in Fig 5.8 (a).

## 5.2.4 PANI modified sol-gel coatings

The improved performance on addition of the PVB is mainly attributed to lowering the porosity of sol-gel layer. Therefore, further modification by the addition of different forms of PANI was explored. The behaviour of these coatings is discussed below.

Nyquist plots for PANI\_AP/NMP\_PVB and PANI\_NF/NMP\_PVB coatings are given in Fig 5.10 for 1 hour, 1, 4, 8 days immersion in 3.5% NaCl solution as well 1 and 4 hours immersion for PANI\_CB/NMP\_PVB. The EEC used for fitting the EIS data for PANI modified coatings, within 4 days immersion, was the same as that used for the PVB modified coatings as depicted in Fig 5.8 (a). However, a different EEC (Fig 5.11) was used for the EIS results obtained for 8 days immersion, which included a charge transfer resistance ( $R_{\text{ct}}$ ) and a parallel double layer capacitance ( $C_{\text{dl}}$ ) after the component of intermediate layer resistance ( $R_{\text{in}}$ ),

due to the corrosion activity on the alloy surface. The fitted EIS parameters are listed in Table 5.4 after numerical fitting.

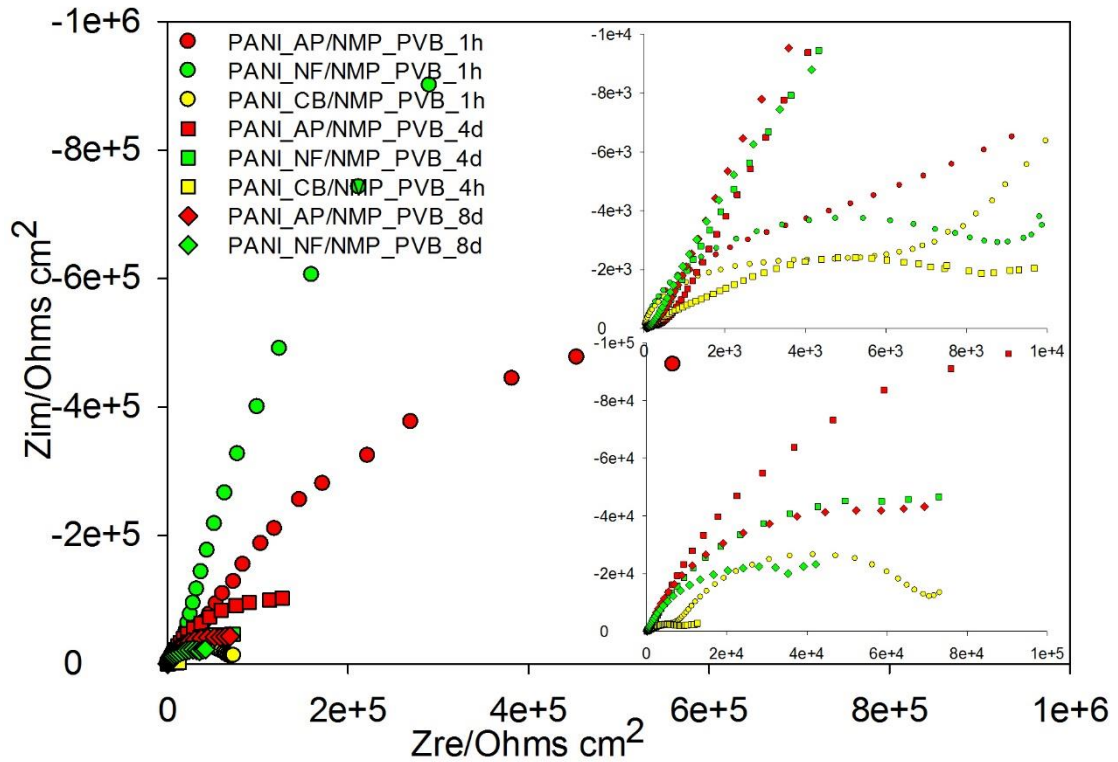


Fig 5.10 Nyquist plots of PANI AP and NF modified sol-gel coated AA2024 in 3.5%NaCl solution during 1 hour, 1 day, 4 days immersion and PANI CB modified coatings during 1 hour and 4 hours immersion.

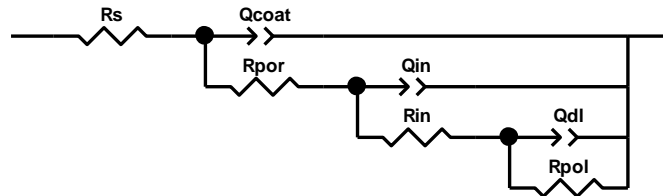


Fig 5.11 EEC used for the simulation of PANI AP and NF modified coatings in 3.5% NaCl solution during 8 days immersion.

From Table 5.4, it can be seen that all the data showed a good fit to the relevant EECs. With regard to the properties of the sol-gel layer, the value of pore resistance ( $R_{por}$ ) in all PANI modified coatings was lower than those in the unmodified PVB sol-gel coatings, which may due to the conductive properties of PANI ES. For a comparison in coating capacitance ( $Q_{coat}$ ), relative lower values of  $Q_{coat}$  were obtained in PANI\_AP/NMP\_PVB, but not in PANI\_NF/NMP\_PVB. This may stem from the addition of PANI agglomerated particles which produce

a more uniform and homogenous sol-gel coating than that of PANI nanofibers, thereby offering more resistance to water uptake. The images in Fig 5.12 taken for three PANI modified sol-gels on glass slides, clearly show that a more homogenous film may be obtained by the addition of PANI agglomerated particles (Fig 5.12 left) due to a shorter polymer chain and better solubility in the NMP than the nanofibers (Fig 5.12 middle).

Sol-gel coating	SG_PVB_4			PANI_AP/NMP_PVB				PANI_NF/NMP_PVB				PANI_CB/NMP_PVB	
Immersion time (hour)	1	24	96	1	24	96	192	1	24	96	192	1	4
Goodness ( $10^{-3}$ )	6.55	2.36	1.82	3.56	4.13	1.24	1.56	5.03	5.17	5.94	0.85	5.26	2.55
$R_s (\Omega \cdot \text{cm}^2)$	25.8	48.1	46.7	13.5	33.9	29.1	22.3	16.0	24.4	23.0	17.3	11.4	20.7
$Q_{\text{coat}} (\text{nS} \cdot \text{cm}^{-2})$	48	975	1795	7	94	654	1450	62	2116	2756	5042	115	556
$n_{\text{coat}}$	0.80	0.69	0.64	0.90	0.71	0.63	0.70	0.84	0.69	0.67	0.72	0.81	0.69
$R_{\text{por}} (\Omega \cdot \text{cm}^2)$	93867	9174	804	68415	2640	1387	127	31215	778	547	62	6507	93
$Q_{\text{in}} (\mu\text{S} \cdot \text{cm}^{-2})$	2.3	2.8	7.7	0.5	1.3	2.8	5.9	2.1	8.7	12.3	16.5	4.9	27.0
$n_{\text{in}}$	0.83	0.72	0.66	0.69	0.73	0.78	0.78	0.88	0.78	0.76	0.79	0.75	0.45
$R_{\text{in}} (\text{k}\Omega \cdot \text{cm}^2)$	19063	1836	356	16973	4041	1431	668	15683	514	416	213	83	15
$R_{\text{CT}} (\text{k}\Omega \cdot \text{cm}^2)$							119				64		
$Q_{\text{dl}} (\mu\text{S} \cdot \text{cm}^{-2})$							10.5				15.5		
$n_{\text{dl}}$							0.84				0.83		

Table 5.4 Parameters of PVB and PANI modified sol-gel system after fitting the EIS data with different EECs in Fig 5.8 (a) and Fig 5.11.

When considering the parameters of the intermediate layer, it can be seen that the value of  $R_{\text{in}}$  for PANI\_AP/NMP\_PVB at 192 hours immersion ( $688 \text{ k}\Omega \cdot \text{cm}^2$ ) was even higher than that of SG\_PVB\_4 at 96 hours immersion ( $356 \text{ k}\Omega \cdot \text{cm}^2$ ). From the comparison of other values in both resistance ( $R_{\text{in}}$ ) and capacitance ( $Q_{\text{in}}$ ) of PANI\_AP/NMP\_PVB and SG\_PVB\_4 coatings, it was evident that the modification using PANI agglomerated particles led to an improvement in stability of the intermediate layer.

However, it seems that the intermediate layer in PANI\_NF/NMP\_PVB was more unstable than either PANI\_AP/NMP\_PVB or SG\_PVB\_4 coating. It is suggested that the poorly dispersed blocks of PANI nanofibers provides more and bigger pores or defects in the coating, which lead to easier penetration of the electrolyte to the intermediate layer.

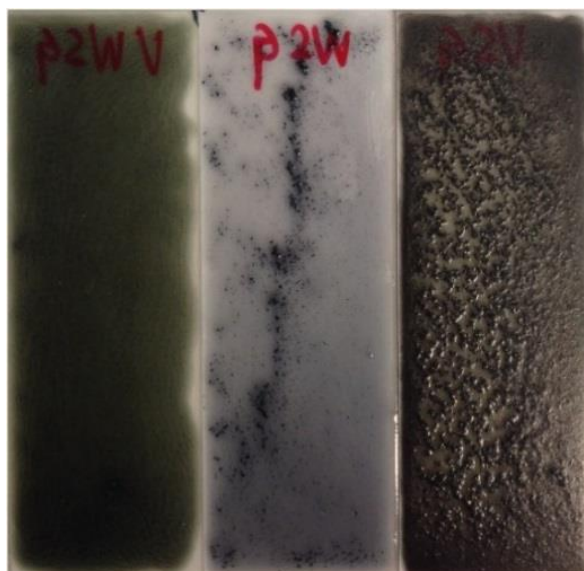


Fig 5.12 Images of three PANI modified sol-gels on glass slides; PANI\_AP/NMP\_PVB (left), PANI\_NF/NMP\_PVB (middle), PANI\_CB/NMP\_PVB (right)

For PANI\_CB/NMP\_PVB coating, as seen from Fig 5.12 (right), the sol-gel modified by PANI CB exhibited a very quick degradation of both the sol-gel layer and intermediate layer as seen from the parameters in Table 5.3. This is due to the introduction of many highly conductive, non-bonding and insoluble carbon black particles.

With respect to the mechanism of protection by PANI, it has been typically assumed by several researchers that the growth of  $\text{Al}_2\text{O}_3$  oxide layer initiated by PANI at the interface of the metal and the coating may be the possible mechanism [137, 139, 143]. According to a recent study by Gobara et al [142, 161], the formation of Al-O-N complex between PANI and AA2024 was responsible for the corrosion protection, rather than the oxide of  $\text{Al}_2\text{O}_3$ . Although various mechanisms have been proposed, the full protection process is still not clear. It is suggested that further studies on the corrosion protection mechanism on AA2024 by PANI are carried out in future work, due to the limited time of this research.

In summary, the corrosion performance of PANI modified sol-gel coatings largely depends on the type of PANI used. If a very uniform and homogeneous sol-gel

can be obtained, the PANI may act as an efficient inhibitor to either stabilise the intermediate layer or provide a denser sol-gel layer with low permeability to the electrolyte. The as-synthesised PANI agglomerated particles used in this study, due to its good solubility in NMP, can provide a dense, uniform and homogeneous sol-gel coating and therefore became efficient in producing an anticorrosive sol-gel coating. The modification by as prepared PANI nanofibers, due to its poor solubility in NMP and dispersion in the sol-gel, may not be a good additive to improve the corrosion protection properties of the sol-gel coating. Commercial product of PANI ES on carbon black did not improve the corrosion protection performance of the sol-gel coatings, due not only to the high ratio of highly conductive and bonding free carbon black, but also the rough sol-gel coating produced.

### 5.2.5 GF modified sol-gel coatings

Further modification by the addition of glass flake was made to the PVB modified coatings and PANI nanofibers modified PVB coatings in order to evaluate its effect on the corrosion protection performance. Nyquist plots of glass flake modified PVB sol-gel coating during 1 hour, 1 day and 4 days immersion, and PANI NF sol-gel coatings during 1 hour, 4 and 8 days immersion are shown in Fig 5.13. From the Nyquist plots, it can be seen that both the EECs used for fitting the EIS data of PANI modified coatings may also be applicable for glass flake modified coatings. Therefore, the model for immersion of glass flakes modified coatings within 4 days immersion can be related to the EEC in Fig 5.8 (a), whilst the model in Fig 5.11 was used for 8 days immersion.

Table 5.5 lists the fitted EIS parameters in relation to the EECs at 1 hour, 24 and 96 hours for glass flake modified PVB sol-gel coatings and additional 192 hours for glass flake modified PANI NF sol-gel coatings. Corresponding PVB and PANI NF modified sol-gel coatings without glass flake were also displayed for the

convenience of comparison.

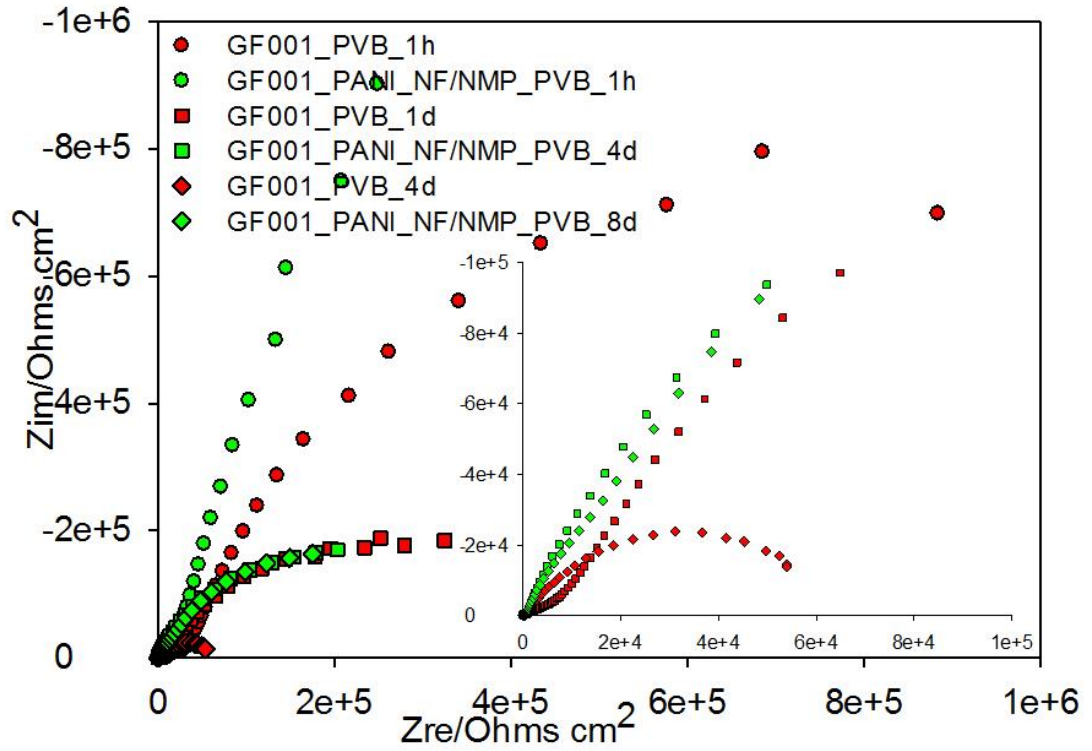


Fig 5.13 Nyquist plots of GF001 modified PVB and PANI NF sol-gel coatings on AA2024 in 3.5%NaCl solution during 1 hour, 1 day, 4 days immersion and additional 8 days for GF001\_PANI\_NF/NMP\_PVB coating.

Sol-gel coating	GF001_PVB			SG_PVB_4			GF001_PANI_NF/NMP_PVB				PANI_NF/NMP_PVB			
Immersion time (hour)	1	24	96	1	24	96	1	24	96	192	1	24	96	192
Goodness ( $10^{-3}$ )	5.54	4.09	3.93	6.55	2.36	1.82	2.91	1.14	3.11	0.86	5.03	5.17	5.94	0.85
$R_s$ ( $\Omega \cdot \text{cm}^2$ )	28.0	36.4	13.2	25.8	48.1	46.7	13.2	23.9	24.0	22.6	16.0	24.4	23.0	17.3
$Q_{\text{coat}}$ ( $\text{nS} \cdot \text{cm}^{-2}$ )	42	1352	2258	48	975	1795	43	1414	1644	1943	62	2116	2756	5042
$n_{\text{coat}}$	0.82	0.62	0.66	0.80	0.69	0.64	0.88	0.62	0.64	0.68	0.84	0.69	0.67	0.72
$R_{\text{por}}$ ( $\Omega \cdot \text{cm}^2$ )	35715	3837	146	93867	9174	804	33491	3861	953	786	31215	778	547	62
$C_{\text{in}}$ ( $\mu\text{S} \cdot \text{cm}^{-2}$ )	0.2	7.1	18.1	2.3	2.8	7.7	1.2	1.9	4.1	8.2	2.1	8.7	12.3	16.5
$n_{\text{in}}$	0.75	0.73	0.70	0.83	0.72	0.66	0.84	0.83	0.84	0.80	0.88	0.78	0.76	0.79
$R_{\text{in}}$ ( $\text{k}\Omega \cdot \text{cm}^2$ )	18330	466	51	19063	1836	356	18650	1641	614	526	15683	514	416	213
$R_{\text{CT}}$ ( $\text{k}\Omega \cdot \text{cm}^2$ )										586				64
$C_{\text{dl}}$ ( $\mu\text{S} \cdot \text{cm}^{-2}$ )										2.0				15.5
$n_{\text{dl}}$										0.90				0.83

Table 5.5 Parameters of GF001 modified and unmodified PVB and PANI sol-gel system after fitting the EIS data with different EECs in Fig 5.8 (a) and Fig 5.11. From Table 5.5, it can be seen that when bare glass flake was added into PVB sol-gel coatings, both the sol-gel layer and intermediate layer became worse as the values of capacitance ( $Q_{\text{coat}}$  and  $Q_{\text{in}}$ ) were higher and resistance ( $R_{\text{por}}$  and  $R_{\text{in}}$ ) were lower than those of PVB sol-gel coating without glass flake. This may indicate that the addition of GF001 may introduce a greater number of large pores

or defects in the sol-gel coatings, therefore both the sol-gel layer and intermediate layer suffered more from corrosion attack than those of uniform PVB sol-gel coating.

However, the influence of glass flake on the PANI NF sol-gel coatings seemed to be opposite to that added in the PVB sol-gel coating. Both a relative stable sol-gel layer and intermediate layer were obtained in the ternary systems of GF001\_PANI\_NF/NMP\_PVB coating compared with all the other three coatings. Although it seems that the sol-gel layer of GF001\_PANI\_NF/NMP\_PVB coatings was not as stable as that of SG\_PVB\_4, due to some higher values of pore resistance ( $R_{por}$ ) and lower coating capacitance ( $Q_{coat}$ ) in the SG\_PVB\_4 coating (e.g.  $R_{por}$  at 1 hour of  $93867 \Omega \cdot \text{cm}^2$  and 24 hours of  $9174 \Omega \cdot \text{cm}^2$ ,  $Q_{coat}$  at 24 hours of  $97 \text{ nS} \cdot \text{cm}^{-2}$ ), the values for these at 192 hours immersion were  $64 \Omega \cdot \text{cm}^2$  for  $R_{por}$  and  $2679 \text{ nS} \cdot \text{cm}^{-2}$  for SG\_PVB\_4 coating. The sol-gel layer of this coating was therefore nearly saturated with electrolyte during 192 hours immersion, whilst the relative long term resistant to electrolyte attack of sol-gel layer was preserved in GF001\_PANI\_NF/NMP\_PVB coatings. Following the long term resistance of glass flake to water uptake, the intermediate layer, which suffered less from corrosion attack and maybe also “protected” by PANI, became more stable than other three coatings. Compared with bare PANI NF modified coatings, the addition of glass flake exhibited some positive effects in the sol-gel layer and intermediate layer. However, when taking the performance of PANI\_AP/NMP\_PVB into consideration, no obvious improvement can be seen with the addition of glass flake. Due to limited time of research, future work is required to reveal the significant difference in the corrosion performance of GF001\_PVB and GF001\_PANI\_NF/NMP\_PVB coatings.

It appears that the introduction of the GF001 in the sol-gel coating may have both positive and negative effects. With regard to the thickness, the coating is about  $5 \mu\text{m}$ , whilst is about  $1 \mu\text{m}$  for GF001. From the optical image of GF001 modified PANI sol-gel coating in Fig 5.14, it can be seen that GF001 can be either buried



in the coating or protrude out of the coating. This was further confirmed by the interferometry images in Fig 5.15. The buried GF001 is highlighted in the black circle in Fig 5.15 (left) and protruded flakes are observed in Fig 5.15 (right).

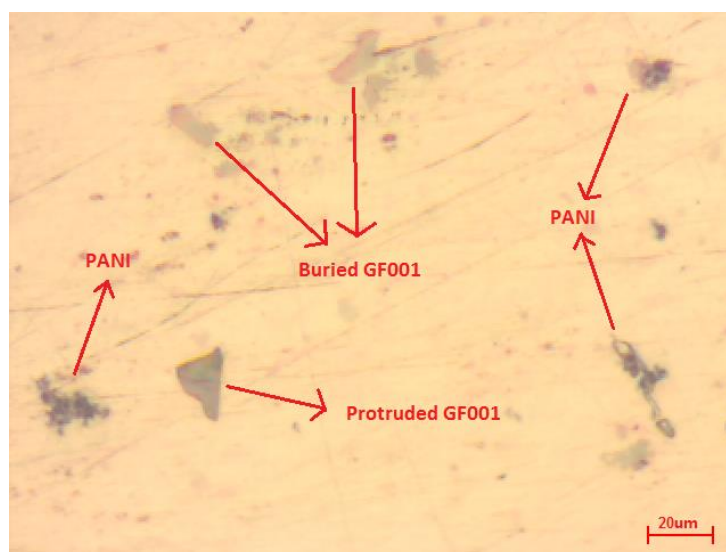


Fig 5.14 Optical image of GF001 modified PANI sol-gel coating on 1μm mirror finished AA2024.

It is suggested that, if the GF001 were all uniformly buried in the coating, as those glass flakes applied in the thick epoxy resin based coatings (e.g. 50-200μm), the well distributed and stacked glass flake may be able to act as superior physical barrier pigments to electrolyte or other aggressive species. However, if the GF001 was half buried and protruded out of the coating surface, especially of the large ones with a diameter over 50μm, the adverse effects may be introduced by the glass flake, due to the formation of weakened interfacial sites within the sol-gel coating, leading to preferential pathways for the electrolyte.

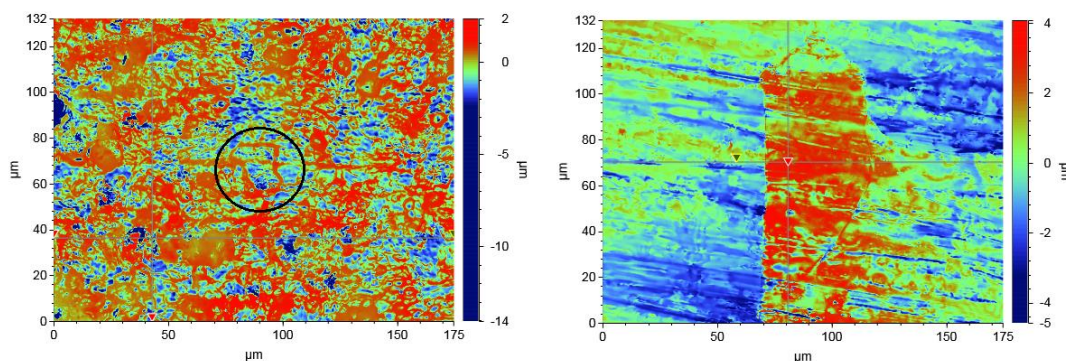


Fig 5.15 Interferometry images of GF001 modified sol-gel coatings showing buried (left) and protruded (right) GF001.

It may therefore be concluded that, the modification of the sol-gel coating by glass flake may not be able to efficiently improve the anticorrosive performance of the coating. Due to the lack of bonding of the GF001 surface, small thickness ratio of sol-gel coating: GF001 (5:1) and variations of the diameter of GF001 (10~200 $\mu$ m), the properties of bare glass flake modified PVB sol-gel coatings lead to poor corrosion protection performance. When glass flake was used together with PANI, only limited improvement was obtained due to both the positive and negative effects introduced by GF001 to the sol-gel coating. Thus, unless uniform sol-gel coatings can be produced with glass flake buried, distributed or evenly stacked within the sol-gel matrix, improvement of corrosion protection performance may not be possible to obtain with coatings of this thickness.

# Chapter 6 Conclusions and future work

## 6.1 Conclusions

This dissertation has reported on the corrosion protection of AA2024-T3 alloy by various modified hybrid titania-containing sol-gel coatings. The modifications were made by the addition of commercial products of polyvinyl butyral (PVB) and glass flake (GF001) as well as the as-synthesised polyaniline (PANI) emeraldine salt of agglomerated particles and nanofibers, along with commercial product of PANI ES on carbon black. The corrosion protection performance of AA2024 alloy coated with standard and modified sol-gel coatings were evaluated by electrochemical impedance spectroscopy during immersion in 3.5% NaCl solution. Important properties of the coatings, such as adhesion strength, surface hydrophobicity, thermal stability and chemical bonding, were all assessed by different techniques.

Based on the work in this study, the following conclusions may be drawn:

### 6.1.1 Preparation of materials

1. Alkaline etching followed by acid desmutting is effective in removing the native oxide layer and Cu-rich intermetallic particles to produce a clean, uniform, hydrophobic and chemical active surface of AA2024.
2. Pure, uniform PANI nanofibers can be synthesised via the chemical oxidative polymerization of aniline by ammonia persulphate in aqueous 1M HNO<sub>3</sub> solution via rapid-mixing method, whilst agglomerated particles of PANI can be produced through a slow-mixing route.
3. A temperature of 120 °C for curing the standard sol-gel coating is also a suitable cure temperature for all the modified coatings.
4. Modification of the sol-gel through addition of all the pigments influences the hydrolysis and condensation processes of the standard sol-gels.

### 6.1.2 Properties of the sol-gel coatings

1. Modification by PANI increases the hydrophobicity of the sol-gel coating, whereas PVB and GF001 cause the surface of the coating to be more hydrophilic.
2. Excellent adhesion can be achieved between the alkaline cleaned AA2024 substrate and all sol-gel coating systems, whereas the coatings are poorly bonded on the surface of acetone degreased or acid desmuted AA2024 substrates.
3. Standard PVB modified coatings are thermally unstable in comparison to a standard sol-gel coating. However, modification by PANI or glass flake on PVB coatings improves the thermal stability in comparison to the standard sol-gel coating.

### 6.1.3 Corrosion performance

1. Increased corrosion protection performance of the coating can be directly related to increased adhesion strength.
2. The standard sol-gel coating can only provide limited corrosion protection for AA2024 alloy in 3.5% NaCl solution, due to the porous nature of the sol-gel network.
3. Modification of the sol-gel by PVB is effective in improving the corrosion protection. The optimum volume ratio of PVB (10% ethanol solution) versus the standard sol was found to be 1:4.
4. The addition of PANI ES agglomerated particles is effective for the production of a homogeneous, dense and uniform sol-gel coating providing a stable intermediate layer and better corrosion protection performance. In comparison PANI nanofibers offer no obvious improvement. The commercial product of PANI ES on carbon black is not suitable for corrosion protection in the sol-gel coatings, due to the high ratio of bond-free and conductive carbon

black, which leads to larger pores and defects in the sol-gel network.

5. Modification of the sol-gel by GF001 is not suitable for the production of thin sol-gel coatings as more defects are introduced and poor corrosion resistance results. However, when glass flake is used in combination with PANI, improved corrosion protection performance can be achieved, but with greater variations on the properties as the glass flake can be either buried in the sol-gel matrix or protrude out of the coating surface.

## 6.2 Future work

Based on the results of the present study, the following suggestions for future work are proposed below:

1. The influence of PVB on the degree of hydrolysis and condensation of the standard sol-gel may be clarified from an XPS study.
2. Further improvement in corrosion protection performance of PANI modified sol-gel coatings may be achieved by increasing the ratio of PANI ES AP or using well dispersed PANI nanoparticles (e.g. using dodecylbenzene sulphonic acid as a dopant).
3. To explore the mechanism of corrosion protection by PANI, the surface oxide of AA2024 and oxidation state of PANI may need to be studied when both materials directly interact with each other and are immersed in wet conditions. A scratch corrosion test on PANI (EB and ES) only film on AA2024 may also be possible to reveal the nature of the protection mechanism.
4. Modification of GF001 prior to the addition in sol-gel, typically surface cleaning or salinization, may be possible to enhance the chemical interactions between the sol-gel and glass flake. The glass flake may also be modified by PANI to produce GF-PANI composites before applied in the sol-gel. Smaller (diameter less than 10 $\mu$ m) and thinner (thickness of 100 nm) glass flake may also provide uniform, dense thin films.
5. Use different ratios of PANI and GF001 to explore the interaction between them and its influence on the corrosion performance of prepared coatings.
6. In-situ synthesized PANI-TiO<sub>2</sub> nanoplate in the sol-gel may be a promising pigment to improve the corrosion protection performance of the coatings.

# References

1. Ahmad, Z., *Principles of corrosion engineering and corrosion control*. 2006: Butterworth-Heinemann.
2. Revie, R.W., *Corrosion and corrosion control*. 2008: John Wiley & Sons.
3. Marcus, P., *Corrosion mechanisms in theory and practice*. 2011: CRC Press.
4. Uhlig, H.H. and R.W. Revie, *Uhlig's corrosion handbook*. Vol. 51. 2011: John Wiley & Sons.
5. Schweitzer, P.A., *Fundamentals of metallic corrosion: atmospheric and media corrosion of metals*. 2006: CRC press.
6. Kaesche, H., *Corrosion of metals: physicochemical principles and current problems*. 2003: Springer.
7. Schweitzer, P.A., *Fundamentals of corrosion: mechanisms, causes, and preventative methods*. 2009: CRC Press.
8. McCafferty, E., *Introduction to corrosion science*. 2010: Springer.
9. Wessel, J.K., *The handbook of advanced materials: enabling new designs*. 2004: John Wiley & Sons.
10. Cottis, R., *Shreir's Corrosion*. 2010: Elsevier Amsterdam.
11. Bardal, E., *Corrosion and protection*. 2004: Springer.
12. Cicek, V., *Cathodic Protection: Industrial Solutions for Protecting Against Corrosion*. 2013: John Wiley & Sons.
13. Ghali, E., V.S. Sastri, and M. Elboudjaini, *Corrosion prevention and protection: practical solutions*. 2007: John Wiley & Sons.
14. von Baekmann, W., W. Schwenk, and W. Prinz, *Handbook of Cathodic Corrosion Protection*. 1997: Gulf Professional Publishing.
15. Schweitzer, P.A., *Corrosion of Linings & Coatings: Cathodic and Inhibitor Protection and Corrosion Monitoring*. 2006: CRC press.
16. Sastri, V.S., *Green corrosion inhibitors: Theory and practice*. Vol. 10. 2012: John Wiley & Sons.

17. Sørensen, P.A., et al., *Anticorrosive coatings: a review*. Journal of Coatings Technology and Research, 2009. **6**(2): p. 135-176.
18. Wicks Jr, Z.W., et al., *Organic coatings: science and technology*. 2007: John Wiley & Sons.
19. Forsgren, A., *Corrosion control through organic coatings*. 2006: CRC Press.
20. Vargel, C., *Corrosion of aluminium*. 2004: Elsevier.
21. Kaufman, J.G., *Introduction to aluminum alloys and tempers*. 2000: ASM International.
22. Davis, J.R. and J.R. Davis, *Aluminum and aluminum alloys*. 1993: ASM international.
23. Chen, G., M. Gao, and R. Wei, *Microconstituent-induced pitting corrosion in aluminum alloy 2024-T3*. Corrosion, 1996. **52**(1): p. 8-15.
24. Buchheit, R., et al., *Local Dissolution Phenomena Associated with S Phase (Al<sub>2</sub>CuMg) Particles in Aluminum Alloy 2024 - T3*. Journal of the Electrochemical Society, 1997. **144**(8): p. 2621-2628.
25. Yasakau, K.A., et al., *Mechanism of Corrosion Inhibition of AA2024 by Rare-Earth Compounds*. The Journal of Physical Chemistry B, 2006. **110**(11): p. 5515-5528.
26. Davis, J.R., *Corrosion of aluminum and aluminum alloys*. 1999: ASM International.
27. Buchheit, R.G., M.A. Martinez, and L.P. Montes, *Evidence for Cu Ion Formation by Dissolution and Dealloying the Al<sub>2</sub>CuMg Intermetallic Compound in Rotating Ring - Disk Collection Experiments*. Journal of The Electrochemical Society, 2000. **147**(1): p. 119-124.
28. Buchheit, R., et al., *The Electrochemical Characteristics of Bulk - Synthesized Al<sub>2</sub>CuMg*. Journal of The Electrochemical Society, 1999. **146**(12): p. 4424-4428.
29. Bocher, F., H.M. Flower, and M.P. Ryan, *The Effect of Microstructure on Localized Corrosion in Creep Age-Formable Aluminum Alloys: Identification of Intermetallic Particles and Pit Initiation Sites*. Journal of The Electrochemical Society, 2006. **153**(12): p. B551-B554.
30. Twite, R. and G. Bierwagen, *Review of alternatives to chromate for corrosion protection of aluminum aerospace alloys*. Progress in organic coatings, 1998. **33**(2): p. 91-100.



31. Schmutz, P. and G.S. Frankel, *Characterization of AA2024 - T3 by Scanning Kelvin Probe Force Microscopy*. Journal of The Electrochemical Society, 1998. **145**(7): p. 2285-2295.
32. Campestrini, P., et al., *Relation between microstructural aspects of AA2024 and its corrosion behaviour investigated using AFM scanning potential technique*. Corrosion Science, 2000. **42**(11): p. 1853-1861.
33. Zhang, W. and G.S. Frankel, *Transitions between pitting and intergranular corrosion in AA2024*. Electrochimica Acta, 2003. **48**(9): p. 1193-1210.
34. MacQueen, R., R. Miron, and R. Granata, *Method for corrosion inhibitor mechanism studies in epoxy coated aluminium*. JCT, Journal of coatings technology, 1996. **68**(857): p. 75-82.
35. Lamaka, S.V., et al., *High effective organic corrosion inhibitors for 2024 aluminium alloy*. Electrochimica Acta, 2007. **52**(25): p. 7231-7247.
36. Birbilis, N., et al., *Inhibition of AA2024-T3 on a Phase-by-Phase Basis Using an Environmentally Benign Inhibitor, Cerium Dibutyl Phosphate*. Electrochemical and Solid-State Letters, 2005. **8**(11): p. C180-C183.
37. Domingues, L., et al., *EIS on plasma-polymerised coatings used as pre-treatment for aluminium alloys*. Electrochimica Acta, 2002. **47**(13-14): p. 2253-2258.
38. Fernandes, J.C.S., et al., *Plasma-polymerised coatings used as pre-treatment for aluminium alloys*. Surface and Coatings Technology, 2002. **154**(1): p. 8-13.
39. Wang, H. and R. Akid, *A room temperature cured sol-gel anticorrosion pre-treatment for Al 2024-T3 alloys*. Corrosion Science, 2007. **49**(12): p. 4491-4503.
40. Zheludkevich, M.L., et al., *Corrosion protective properties of nanostructured sol-gel hybrid coatings to AA2024-T3*. Surface and Coatings Technology, 2006. **200**(9): p. 3084-3094.
41. Shchukin, D.G., et al., *Layer - by - Layer Assembled Nanocontainers for Self - Healing Corrosion Protection*. Advanced Materials, 2006. **18**(13): p. 1672-1678.
42. Green, W.J. and C.R. Hegedus, *Combination primer/topcoat coating*. 1989, Google Patents.
43. Hu, J.-M., et al., *Electrodeposition of silane films on aluminum alloys for corrosion protection*. Progress in Organic Coatings, 2007. **58**(4): p. 265-271.
44. Arenas, M., et al., *Synthesis and electrochemical evaluation of polypyrrole coatings electrodeposited onto AA-2024 alloy*. Progress in Organic Coatings, 2008. **62**(1): p. 79-86.

45. Tallman, D.E., et al., *Electroactive conducting polymers for corrosion control*. Journal of Solid State Electrochemistry, 2001. **6**(2): p. 73-84.
46. Tallman, D., Y. Pae, and G. Bierwagen, *Conducting polymers and corrosion: part 2-polyaniline on aluminum alloys*. Corrosion, 2000. **56**(4): p. 401-410.
47. He, J., et al., *Conducting Polymers and Corrosion III. A Scanning Vibrating Electrode Study of Poly(3 - octyl pyrrole) on Steel and Aluminum*. Journal of The Electrochemical Society, 2000. **147**(10): p. 3667-3672.
48. Mansfeld, F. and M.W. Kendig, *Evaluation of Anodized Aluminum Surfaces with Electrochemical Impedance Spectroscopy*. Journal of The Electrochemical Society, 1988. **135**(4): p. 828-833.
49. Liu, Z., et al., *Fundamental understanding of the corrosion performance of laser-melted metallic alloys*. Surface and Coatings Technology, 2006. **200**(18-19): p. 5514-5525.
50. Raps, D., et al., *Electrochemical study of inhibitor-containing organic-inorganic hybrid coatings on AA2024*. Corrosion Science, 2009. **51**(5): p. 1012-1021.
51. Zheludkevich, M., et al., *Nanostructured sol-gel coatings doped with cerium nitrate as pre-treatments for AA2024-T3: Corrosion protection performance*. Electrochimica Acta, 2005. **51**(2): p. 208-217.
52. Schem, M., et al., *CeO<sub>2</sub>-filled sol-gel coatings for corrosion protection of AA2024-T3 aluminium alloy*. Corrosion Science, 2009. **51**(10): p. 2304-2315.
53. Gonzalez, E., et al., *A silanol-based nanocomposite coating for protection of AA-2024 aluminium alloy*. Electrochimica Acta, 2011. **56**(22): p. 7586-7595.
54. Vreugdenhil, A., V. Balbyshev, and M. Donley, *Nanostructured silicon sol-gel surface treatments for Al 2024-T3 protection*. Journal of Coatings Technology, 2001. **73**(915): p. 35-43.
55. Voevodin, N., et al., *An organically modified zirconate film as a corrosion-resistant treatment for aluminum 2024-T3*. Progress in Organic Coatings, 2001. **41**(4): p. 287-293.
56. Wen, J. and G.L. Wilkes, *Organic/Inorganic Hybrid Network Materials by the Sol-Gel Approach*. Chemistry of Materials, 1996. **8**(8): p. 1667-1681.
57. Hench, L.L. and J.K. West, *The sol-gel process*. Chemical Reviews, 1990. **90**(1): p. 33-72.

58. Brinker, C.J. and G.W. Scherer, *Sol-gel science: the physics and chemistry of sol-gel processing*. 1990: Gulf Professional Publishing.
59. Graham, T., XXXV.-*On the properties of silicic acid and other analogous colloidal substances*. Journal of the Chemical Society, 1864. **17**(0): p. 318-327.
60. ROY, R., *Ceramics by the Solution-Sol-Gel Route*. Science, 1987. **238**(4834): p. 1664-1669.
61. Wang, D. and G.P. Bierwagen, *Sol-gel coatings on metals for corrosion protection*. Progress in Organic Coatings, 2009. **64**(4): p. 327-338.
62. Pierre, A.C., *Introduction to sol-gel processing*. Vol. 1. 1998: Springer.
63. Lerouge, F., G. Cerveau, and R.J. Corriu, *Supramolecular self-organization in non-crystalline hybrid organic-inorganic nanomaterials induced by van der Waals interactions*. New journal of chemistry, 2006. **30**(10): p. 1364-1376.
64. Znaidi, L., *Sol-gel-deposited ZnO thin films: A review*. Materials Science and Engineering: B, 2010. **174**(1-3): p. 18-30.
65. Ciriminna, R., et al., *The sol-gel route to advanced silica-based materials and recent applications*. Chem Rev, 2013. **113**(8): p. 6592-620.
66. Wright, J.D. and N.A. Sommerdijk, *Sol-gel materials: chemistry and applications*. Vol. 4. 2000: CRC press.
67. Zheludkevich, M.L., I.M. Salvado, and M.G.S. Ferreira, *Sol-gel coatings for corrosion protection of metals*. Journal of Materials Chemistry, 2005. **15**(48): p. 5099.
68. Wang, H. and R. Akid, *Encapsulated cerium nitrate inhibitors to provide high-performance anti-corrosion sol-gel coatings on mild steel*. Corrosion Science, 2008. **50**(4): p. 1142-1148.
69. Wang, H., R. Akid, and M. Gobara, *Scratch-resistant anticorrosion sol-gel coating for the protection of AZ31 magnesium alloy via a low temperature sol-gel route*. Corrosion Science, 2010. **52**(8): p. 2565-2570.
70. Yuan, J. and S. Tsujikawa, *Characterization of Sol - Gel - Derived TiO<sub>2</sub> Coatings and Their Photoeffects on Copper Substrates*. Journal of the Electrochemical Society, 1995. **142**(10): p. 3444-3450.
71. Atik, M., et al., *Sol-gel thin films for corrosion protection*. Ceramics International, 1995. **21**(6): p. 403-406.
72. Guglielmi, M., *Sol-gel coatings on metals*. Journal of sol-gel science and technology, 1997. **8**(1-3): p. 443-449.

73. Chou, T., C. Chandrasekaran, and G. Cao, *Sol-gel-derived hybrid coatings for corrosion protection*. Journal of Sol-Gel Science and Technology, 2003. **26**(1-3): p. 321-327.
74. Fedrizzi, L., et al., *The use of electrochemical techniques to study the corrosion behaviour of organic coatings on steel pretreated with sol-gel zirconia films*. Electrochimica Acta, 2001. **46**(24): p. 3715-3724.
75. Masalski, J., et al., *Improvement in corrosion resistance of the 316l stainless steel by means of  $Al_2O_3$  coatings deposited by the sol-gel method*. Thin Solid Films, 1999. **349**(1): p. 186-190.
76. Shen, G., Y. Chen, and C. Lin, *Corrosion protection of 316 L stainless steel by a  $TiO_2$  nanoparticle coating prepared by sol-gel method*. Thin Solid Films, 2005. **489**(1): p. 130-136.
77. Zheludkevich, M., et al., *Corrosion protective properties of nanostructured sol-gel hybrid coatings to AA2024-T3*. Surface and Coatings Technology, 2006. **200**(9): p. 3084-3094.
78. Lamaka, S., et al., *Novel hybrid sol-gel coatings for corrosion protection of AZ31B magnesium alloy*. Electrochimica Acta, 2008. **53**(14): p. 4773-4783.
79. Poznyak, S.K., et al., *Preparation and corrosion protective properties of nanostructured titania-containing hybrid sol-gel coatings on AA2024*. Progress in Organic Coatings, 2008. **62**(2): p. 226-235.
80. Ono, S., et al., *Improvement of Corrosion Resistance of Metals by an Environmentally Friendly Silica Coating Method*. Journal of Sol-Gel Science and Technology, 2004. **29**(3): p. 147-153.
81. Lamaka, S.V., et al., *Nanoporous titania interlayer as reservoir of corrosion inhibitors for coatings with self-healing ability*. Progress in Organic Coatings, 2007. **58**(2-3): p. 127-135.
82. Yasakau, K.A., et al., *Influence of sol-gel process parameters on the protection properties of sol-gel coatings applied on AA2024*. Surface and Coatings Technology, 2014. **246**: p. 6-16.
83. Sánchez Majado, S., et al., *Recubrimiento sol-gel con nanopartículas cerámicas para la protección de un sustrato y procedimiento para su obtención*. 2010.
84. Jiménez-Morales, A., et al., *Organic-Inorganic Sol-Gel Coatings Modified with  $TiO_2$  Nanoparticles for Corrosion Protection of a Powder Metallurgical Aluminum Alloy*. Meeting Abstracts, 2012. **MA2012-02**(25): p. 2352.

85. Phillips, J., *Bonds and bands in semiconductors*. 2012: Elsevier.
86. Shirakawa, H., et al., *Synthesis of electrically conducting organic polymers: halogen derivatives of polyacetylene, (CH)<sub>x</sub>*. J. Chem. Soc., Chem. Commun., 1977(16): p. 578-580.
87. MacDiarmid, A.G., "*Synthetic metals*": *A novel role for organic polymers (Nobel lecture)*. Angewandte Chemie International Edition, 2001. **40**(14): p. 2581-2590.
88. Wan, M., *Conducting polymers with micro or nanometer structure*. 2008: Springer.
89. MacDiarmid, A.G., *Synthetic metals: a novel role for organic polymers*. Synthetic Metals, 2001. **125**(1): p. 11-22.
90. Leroux, F., et al., *In Encyclopedia of Nanoscience and Nanotechnology; Nalwa, HS, Ed.* 2011, American Scientific Publishers: Stevenson Ranch, CA.
91. Letheby, H., XXIX.—*On the production of a blue substance by the electrolysis of sulphate of aniline*. J. Chem. Soc., 1862. **15**: p. 161-163.
92. Chiang, J.-C. and A.G. MacDiarmid, '*Polyaniline*': *protonic acid doping of the emeraldine form to the metallic regime*. Synthetic Metals, 1986. **13**(1): p. 193-205.
93. MacDiarmid, A., et al., *Polyaniline: a new concept in conducting polymers*. Synthetic Metals, 1987. **18**(1): p. 285-290.
94. Epstein, A., et al., *Insulator-to-metal transition in polyaniline*. Synthetic Metals, 1987. **18**(1): p. 303-309.
95. Li, D., J. Huang, and R.B. Kaner, *Polyaniline nanofibers: a unique polymer nanostructure for versatile applications*. Accounts of chemical research, 2008. **42**(1): p. 135-145.
96. Carenza, M. and G. Palma, *Radiation-induced heterophase polymerizations. Particle morphology of as-polymerized polyacrylonitrile*. European Polymer Journal, 1985. **21**(1): p. 41-47.
97. Marie, E., et al., *Synthesis of polyaniline particles via inverse and direct miniemulsion*. Macromolecules, 2003. **36**(11): p. 3967-3973.
98. Kuramoto, N. and A. Tomita, *Chemical oxidative polymerization of dodecylbenzenesulfonic acid aniline salt in chloroform*. Synthetic Metals, 1997. **88**(2): p. 147-151.
99. Miras, M.C., C. Barbero, and O. Haas, *Preparation of polyaniline by electrochemical polymerization of aniline in acetonitrile solution*. Synthetic Metals, 1991. **43**(1-2): p. 3081-3084.

100. Dallas, P., et al., *Characterization, magnetic and transport properties of polyaniline synthesized through interfacial polymerization*. Polymer, 2007. **48**(11): p. 3162-3169.
101. Chen, J., et al., *Novel interfacial polymerization for radially oriented polyaniline nanofibers*. Materials Letters, 2007. **61**(6): p. 1419-1423.
102. Huang, J. and R.B. Kaner, *A general chemical route to polyaniline nanofibers*. Journal of the American Chemical Society, 2004. **126**(3): p. 851-855.
103. Huang, J. and R.B. Kaner, *Nanofiber formation in the chemical polymerization of aniline: a mechanistic study*. Angew Chem Int Ed Engl, 2004. **43**(43): p. 5817-21.
104. Qiang, J., et al., *Polyaniline nanofibers synthesized by rapid mixing polymerization*. Synthetic Metals, 2008. **158**(13): p. 544-547.
105. Zhang, X., W.J. Goux, and S.K. Manohar, *Synthesis of polyaniline nanofibers by "nanofiber seeding"*. Journal of the American Chemical Society, 2004. **126**(14): p. 4502-4503.
106. Xing, S., et al., *Morphology and conductivity of polyaniline nanofibers prepared by 'seeding' polymerization*. Polymer, 2006. **47**(7): p. 2305-2313.
107. Guo, Q., et al., *Chemical synthesis of cross-linked polyaniline by a novel solvothermal metathesis reaction of p-dichlorobenzene with sodium amide*. Polymer, 2005. **46**(9): p. 3185-3189.
108. Zhang, L. and M. Wan, *Self - Assembly of Polyaniline—From Nanotubes to Hollow Microspheres*. Advanced Functional Materials, 2003. **13**(10): p. 815-820.
109. Yang, C.H., et al., *Molecular assembled self-doped polyaniline copolymer ultra-thin films*. Polymer, 2007. **48**(11): p. 3237-3247.
110. Zhang, L. and M. Wan, *Chiral polyaniline nanotubes synthesized via a self-assembly process*. Thin Solid Films, 2005. **477**(1-2): p. 24-31.
111. Jing, X., et al., *Polyaniline nanofibers prepared with ultrasonic irradiation*. Journal of Polymer Science Part A: Polymer Chemistry, 2006. **44**(2): p. 1014-1019.
112. Jing, X., et al., *Sonochemical synthesis of polyaniline nanofibers*. Ultrasonics Sonochemistry, 2007. **14**(1): p. 75-80.
113. Delvaux, M., et al., *Chemical and electrochemical synthesis of polyaniline micro-and nano-tubules*. Synthetic Metals, 2000. **113**(3): p. 275-280.
114. Tang, Z., et al., *Electrochemical synthesis of polyaniline nanoparticles*. Electrochemistry communications, 2000. **2**(1): p. 32-35.

115. Bhadra, S., N.K. Singha, and D. Khastgir, *Electrochemical synthesis of polyaniline and its comparison with chemically synthesized polyaniline*. Journal of Applied Polymer Science, 2007. **104**(3): p. 1900-1904.
116. Huang, J., et al., *Mechanochemical route to the conducting polymer polyaniline*. Macromolecules, 2005. **38**(2): p. 317-321.
117. Martin, C.R., *Template synthesis of electronically conductive polymer nanostructures*. Accounts of Chemical Research, 1995. **28**(2): p. 61-68.
118. Nickels, P., et al., *Polyaniline nanowire synthesis templated by DNA*. Nanotechnology, 2004. **15**(11): p. 1524.
119. Zhang, Z., et al., *Synthesis of polyaniline with a hollow, octahedral morphology by using a cuprous oxide template*. Advanced Materials, 2005. **17**(23): p. 2854-2857.
120. Pan, L., et al., *Synthesis of polyaniline nanotubes with a reactive template of manganese oxide*. Advanced Materials, 2007. **19**(3): p. 461-464.
121. Liu, W., et al., *Enzymatically synthesized conducting polyaniline*. Journal of the American Chemical Society, 1999. **121**(1): p. 71-78.
122. Liu, W., et al., *Enzymatic synthesis of conducting polyaniline in micelle solutions*. Langmuir, 2002. **18**(25): p. 9696-9704.
123. Cruz-Silva, R., et al., *Enzymatic synthesis of colloidal polyaniline particles*. Polymer, 2006. **47**(5): p. 1563-1568.
124. Cruz, G., et al., *Synthesis of polyaniline films by plasma polymerization*. Synthetic metals, 1997. **88**(3): p. 213-218.
125. Gong, X., et al., *Plasma - polymerized polyaniline films: Synthesis and characterization*. Journal of Polymer Science Part A: Polymer Chemistry, 1998. **36**(4): p. 633-643.
126. De Barros, R., W. De Azevedo, and F. De Aguiar, *Photo-induced polymerization of polyaniline*. Materials characterization, 2003. **50**(2): p. 131-134.
127. Khanna, P., et al., *Synthesis of Ag/polyaniline nanocomposite via an in situ photo-redox mechanism*. Materials Chemistry and Physics, 2005. **92**(1): p. 214-219.
128. Ćirić-Marjanović, G., *Recent advances in polyaniline research: Polymerization mechanisms, structural aspects, properties and applications*. Synthetic Metals, 2013. **177**: p. 1-47.



129. Stejskal, J., I. Sapurina, and M. Trchová, *Polyaniline nanostructures and the role of aniline oligomers in their formation*. Progress in Polymer Science, 2010. **35**(12): p. 1420-1481.
130. Stejskal, J., P. Kratochvíl, and A.D. Jenkins, *The formation of polyaniline and the nature of its structures*. Polymer, 1996. **37**(2): p. 367-369.
131. Tran, H.D., et al., *The oxidation of aniline to produce "polyaniline": a process yielding many different nanoscale structures*. Journal of Materials Chemistry, 2011. **21**(11): p. 3534.
132. Huang, J. and R.B. Kaner, *Nanofiber formation in the chemical polymerization of aniline: a mechanistic study*. Angewandte Chemie, 2004. **116**(43): p. 5941-5945.
133. Li, D. and R.B. Kaner, *Shape and aggregation control of nanoparticles: not shaken, not stirred*. Journal of the American Chemical Society, 2006. **128**(3): p. 968-975.
134. DeBerry, D.W., *Modification of the electrochemical and corrosion behavior of stainless steels with an electroactive coating*. Journal of the Electrochemical society, 1985. **132**(5): p. 1022-1026.
135. Tallman, D., Y. Pae, and G. Bierwagen, *Conducting polymers and corrosion: polyaniline on steel*. Corrosion, 1999. **55**(8): p. 779-786.
136. Racicot, R., R. Brown, and S.C. Yang, *Corrosion protection of aluminum alloys by double-strand polyaniline*. Synthetic Metals, 1997. **85**(1-3): p. 1263-1264.
137. Epstein, A.J., et al., *Corrosion protection of aluminum and aluminum alloys by polyanilines: A potentiodynamic and photoelectron spectroscopy study*. Synthetic Metals, 1999. **102**(1-3): p. 1374-1376.
138. Jing, X., et al., *Synthesis, structure, properties and applications of conducting polyaniline*. Acta Polymerica Sinica, 2005. **5**: p. 655.
139. Williams, G. and H.N. McMurray, *Polyaniline inhibition of filiform corrosion on organic coated AA2024-T3*. Electrochimica Acta, 2009. **54**(17): p. 4245-4252.
140. Gupta, G., et al., *Polyaniline-lignosulfonate/epoxy coating for corrosion protection of AA2024-T3*. Corrosion Science, 2013. **67**: p. 256-267.
141. Kamaraj, K., et al., *Electropolymerised polyaniline films as effective replacement of carcinogenic chromate treatments for corrosion protection of aluminium alloys*. Synthetic Metals, 2012. **162**(5-6): p. 536-542.

142. Akid, R., M. Gobara, and H. Wang, *Corrosion protection performance of novel hybrid polyaniline/sol-gel coatings on an aluminium 2024 alloy in neutral, alkaline and acidic solutions*. *Electrochimica Acta*, 2011. **56**(5): p. 2483-2492.
143. Seegmiller, J.C., et al., *Mechanism of action of corrosion protection coating for AA2024-T3 based on poly (aniline)-poly (methylmethacrylate) blend*. *Journal of The Electrochemical Society*, 2005. **152**(2): p. B45-B53.
144. Khanna, A.S., *High-performance organic coatings*. 2008: Elsevier.
145. Ghaffari, M., M. Ehsani, and H.A. Khonakdar, *Morphology, rheological and protective properties of epoxy/nano-glassflake systems*. *Progress in Organic Coatings*, 2014. **77**(1): p. 124-130.
146. González-Guzmán, J., et al., *Resistance of metallic substrates protected by an organic coating containing glass flakes*. *Progress in Organic Coatings*, 2010. **68**(3): p. 240-243.
147. Nematollahi, M., et al., *Comparison between the effect of nanoglass flake and montmorillonite organoclay on corrosion performance of epoxy coating*. *Corrosion Science*, 2010. **52**(5): p. 1809-1817.
148. Ehsani, M., H.A. Khonakdar, and A. Ghadami, *Assessment of morphological, thermal, and viscoelastic properties of epoxy vinyl ester coating composites: Role of glass flake and mixing method*. *Progress in Organic Coatings*, 2013. **76**(1): p. 238-243.
149. Sathiyarayanan, S., S. Syed Azim, and G. Venkatachari, *Corrosion protection coating containing polyaniline glass flake composite for steel*. *Electrochimica Acta*, 2008. **53**(5): p. 2087-2094.
150. Feng, Z., et al., *Influence of surface pretreatments on the corrosion protection of sol-gel coated AA2024-T3 aluminium alloy*. *Surface and Interface Analysis*, 2013. **45**(10): p. 1452-1456.
151. See Supplemental Material at <http://www.wilsonsmetals.com/> for QQ-A-250/4 AA2024-T3 alloy (Date of reference : 2014/08/01).
152. See Supplemental Material at <http://www.q-lab.com/> for QQ-A-250/4 AA2024-T3 alloy (Date of reference: 2014/08/01).
153. Huang, W.-S., B.D. Humphrey, and A.G. MacDiarmid, *Polyaniline, a novel conducting polymer. Morphology and chemistry of its oxidation and reduction in aqueous electrolytes*. *Journal of the Chemical Society, Faraday Transactions 1: Physical Chemistry in Condensed Phases*, 1986. **82**(8): p. 2385-2400.

154. YENER, F. and O. JIRSAK, *Improving performance of polyvinyl butyral electrospinning*. Proceedings of Nanocon, 2011: p. 21-23.
155. See Supplemental Material at <http://www.glassflake.com/> for GF001 glass flake (Date of reference: 2014/08/01).
156. *Test Methods for Measuring Adhesion by Tape Test*. 2009, ASTM International.
157. See Supplemental information at <http://www.elcometer.com/> for Elcometer 107 Cross Hatch Cutter (Date of reference: 2014/08/01).
158. Álvarez, P., et al., *The electrochemical behaviour of sol-gel hybrid coatings applied on AA2024-T3 alloy: Effect of the metallic surface treatment*. Progress in Organic Coatings, 2010. **69**(2): p. 175-183.
159. Huang, J. and R.B. Kaner, *The intrinsic nanofibrillar morphology of polyaniline*. Chem Commun (Camb), 2006(4): p. 367-76.
160. Zheludkevich, M.L., et al., *On the application of electrochemical impedance spectroscopy to study the self-healing properties of protective coatings*. Electrochemistry Communications, 2007. **9**(10): p. 2622-2628.
161. Mostafa, M., *Hybrid sol-gel/polyaniline coating for the corrosion protection of AA2024*. 2009, Sheffield Hallam University.
162. López, D.A., S.N. Simison, and S.R. de Sánchez, *Inhibitors performance in CO<sub>2</sub> corrosion: EIS studies on the interaction between their molecular structure and steel microstructure*. Corrosion Science, 2005. **47**(3): p. 735-755.
163. Franquet, A., H. Terryn, and J. Vereecken, *Study of the effect of different aluminium surface pretreatments on the deposition of thin non-functional silane coatings*. Surface and Interface Analysis, 2004. **36**(8): p. 681-684.
164. Daoud, W.A., J.H. Xin, and X. Tao, *Superhydrophobic Silica Nanocomposite Coating by a Low - Temperature Process*. Journal of the American Ceramic Society, 2004. **87**(9): p. 1782-1784.
165. Schmidt, H., S. Langenfeld, and R. Naß, *A new corrosion protection coating system for pressure-cast aluminium automotive parts*. Materials & Design, 1997. **18**(4-6): p. 309-313.
166. Szczygiał, B. and M. Kołodziej, *Composite Ni/Al<sub>2</sub>O<sub>3</sub> coatings and their corrosion resistance*. Electrochimica Acta, 2005. **50**(20): p. 4188-4195.

167. Rincon Troconis, B.C. and G.S. Frankel, *Effect of Roughness and Surface Topography on Adhesion of PVB to AA2024-T3 using the Blister Test*. Surface and Coatings Technology, 2013. **236**(0): p. 531-539.
168. Sun, Y.-K. and I.-H. Oh, *Synthesis of LiNiO<sub>2</sub> powders by a sol-gel method*. Journal of materials science letters, 1997. **16**(1): p. 30-32.
169. Zhang, X., et al., *Preparation and characterization of polyvinyl butyral/silica hybrid antireflective coating: effect of PVB on moisture-resistance and hydrophobicity*. Journal of sol-gel science and technology, 2010. **53**(1): p. 79-84.
170. Agrafiotis, C., et al., *Evaluation of sol-gel methods for the synthesis of doped-ceria environmental catalysis systems. Part I: preparation of coatings*. Journal of the European Ceramic Society, 2002. **22**(1): p. 15-25.
171. Nelson, K., et al., *Characterisation of aluminium alloys after HNO<sub>3</sub>/HF-NaOH-HNO<sub>3</sub>/HF pretreatment*. Materials science and technology, 2001. **17**(10): p. 1211-1221.
172. Wu, H., et al., *Biomimetic nanofiber patterns with controlled wettability*. Soft Matter, 2008. **4**(12): p. 2429-2433.
173. Zhu, Y., et al., *Chemical Dual - Responsive Wettability of Superhydrophobic PANI - PAN Coaxial Nanofibers*. Macromolecular rapid communications, 2007. **28**(10): p. 1135-1141.
174. Joshi, S., W.G. Fahrenholtz, and M.J. O'Keefe, *Effect of alkaline cleaning and activation on aluminum alloy 7075-T6*. Applied Surface Science, 2011. **257**(6): p. 1859-1863.
175. Holub, K.J. and L.J. Matienzo, *Magnesium diffusion in several aluminum alloys*. Applications of Surface Science, 1981. **9**(1-4): p. 22-38.
176. Gospodinova, N. and L. Terlemezyan, *Conducting polymers prepared by oxidative polymerization: polyaniline*. Progress in Polymer Science, 1998. **23**(8): p. 1443-1484.
177. Wei, Y., et al., *A study of the mechanism of aniline polymerization*. Journal of Polymer Science Part A: Polymer Chemistry, 1989. **27**(7): p. 2385-2396.
178. Zhang, D. and Y. Wang, *Synthesis and applications of one-dimensional nano-structured polyaniline: An overview*. Materials Science and Engineering: B, 2006. **134**(1): p. 9-19.
179. Hoebbel, D., M. Nacken, and H. Schmidt, *A NMR study on the hydrolysis, condensation and epoxide ring-opening reaction in sols and gels of the system*

*glycidoxypropyltrimethoxysilane-water-titaniumtetraethoxide*. Journal of sol-gel science and technology, 1998. **12**(3): p. 169-179.

180. Chan, C.-K., et al., *Effects of heat treatment on the properties of poly (methyl methacrylate)/silica hybrid materials prepared by sol-gel process*. Polymer, 2001. **42**(9): p. 4189-4196.

181. Poznyak, S., et al., *Preparation and corrosion protective properties of nanostructured titania-containing hybrid sol-gel coatings on AA2024*. Progress in Organic Coatings, 2008. **62**(2): p. 226-235.

182. José Velasco, M.a., et al., *DSC and FT-IR analysis of the drying process of titanium alkoxide derived precipitates*. Thermochimica Acta, 1999. **326**(1-2): p. 91-97.

183. Li, G., et al., *Fabrication and adhesive properties of thin organosilane films coated on low carbon steel substrates*. Surface and Coatings Technology, 2007. **201**(24): p. 9571-9578.

184. Fedel, M., et al., *Influence of formulation and application parameters on the performances of a sol-gel/clay nanocomposite on the corrosion resistance of hot-dip galvanized steel. Part II. Effect of curing temperature and time*. Surface and Coatings Technology, (0).

185. Song, J. and W. Van Ooij, *Bonding and corrosion protection mechanisms of  $\gamma$ -APS and BTSE silane films on aluminum substrates*. Journal of adhesion science and technology, 2003. **17**(16): p. 2191-2221.

186. Bertoluzza, A., et al., *Raman and infrared spectra on silica gel evolving toward glass*. Journal of Non-Crystalline Solids, 1982. **48**(1): p. 117-128.

187. Fidalgo, A. and L.M. Ilharco, *The defect structure of sol-gel-derived silica/polytetrahydrofuran hybrid films by FTIR*. Journal of Non-Crystalline Solids, 2001. **283**(1-3): p. 144-154.

188. Tanner, P., B. Yan, and H. Zhang, *Preparation and luminescence properties of sol-gel hybrid materials incorporated with europium complexes*. Journal of materials science, 2000. **35**(17): p. 4325-4328.

189. Liu, Z. and R.J. Davis, *Investigation of the structure of microporous Ti-Si mixed oxides by X-ray, UV reflectance, FT-Raman, and FT-IR spectroscopies*. The Journal of Physical Chemistry, 1994. **98**(4): p. 1253-1261.

190. Jeon, H.-J., S.-C. Yi, and S.-G. Oh, *Preparation and antibacterial effects of Ag-SiO<sub>2</sub> thin films by sol-gel method*. Biomaterials, 2003. **24**(27): p. 4921-4928.

191. Grill, A. and D.A. Neumayer, *Structure of low dielectric constant to extreme low dielectric constant SiCOH films: Fourier transform infrared spectroscopy characterization*. Journal of Applied Physics, 2003. **94**(10): p. 6697-6707.
192. Ardhyanta, H., et al., *Effect of pendant group of polysiloxanes on the thermal and mechanical properties of polybenzoxazine hybrids*. Polymer, 2009. **50**(25): p. 5959-5969.
193. Sharma, R.K., S. Das, and A. Maitra, *Surface modified ormosil nanoparticles*. Journal of Colloid and Interface Science, 2004. **277**(2): p. 342-346.
194. Binder, A., A. Heel, and G. Kasper, *Deposition of Palladium Nanodots of Controlled Size and Density onto Surface - Modified SiO<sub>2</sub> Particles by an Atmospheric Pressure CVS/MOCVD Process*. Chemical Vapor Deposition, 2007. **13**(1): p. 48-54.
195. Peri, J., *Oxygen exchange between carbon dioxide (oxygen-18) and acidic oxide and zeolite catalysts*. The Journal of Physical Chemistry, 1975. **79**(15): p. 1582-1588.
196. Wei, Y., D. Yang, and L. Tang, *Synthesis of new polyacrylonitrile - silica hybrid sol - gel materials and their thermal properties*. Die Makromolekulare Chemie, Rapid Communications, 1993. **14**(5): p. 273-278.
197. Jha, P., P.R. Arya, and A. Ganguli, *Dielectric properties of lead zirconium titanates with nanometer size grains synthesized by the citrate precursor route*. Materials chemistry and physics, 2003. **82**(2): p. 355-361.
198. Suzuki, M., et al., *Novel dumbbell-form low-molecular-weight gelators based on L-lysine: their hydrogelation and organogelation properties*. New journal of chemistry, 2005. **29**(11): p. 1439-1444.
199. Sayin, S., E. Aköz, and M. Yilmaz, *Enhanced catalysis and enantioselective resolution of racemic naproxen methyl ester by lipase encapsulated within iron oxide nanoparticles coated with calix [8] arene valeric acid complexes*. Organic & biomolecular chemistry, 2014. **12**(34): p. 6634-6642.
200. Cohn, D., et al., *PEO-PPO-PEO-based poly (ether ester urethane) s as degradable reverse thermo-responsive multiblock copolymers*. Biomaterials, 2006. **27**(9): p. 1718-1727.
201. Gnyba, M., et al., *Raman investigation of sol-gel-derived hybrid polymers for optoelectronics*. Optoelectronics Review, 2002(2): p. 137-144.
202. GNYBA, M., M. KOZANECKI, and P. WIERZBA, *Spectroscopic Studies of Sol-Gel Derived Thin-Film Structures for Integrated Optics*. Molecular and Quantum Acoustics, 2005. **26**: p. 81.

203. Itagaki, Y., et al., *Development of porphyrin dispersed sol-gel films as HCl sensitive optochemical gas sensor*. Sensors and Actuators B: Chemical, 2006. **117**(1): p. 302-307.
204. Chen, Y.C., C.C. Tsai, and Y.D. Lee, *Preparation and properties of silylated PTFE/SiO<sub>2</sub> organic-inorganic hybrids via sol-gel process*. Journal of Polymer Science Part A: Polymer Chemistry, 2004. **42**(7): p. 1789-1807.
205. Mehner, A., et al., *Mechanical and chemical properties of thick hybrid sol-gel silica coatings from acid and base catalyzed sols*. Journal of Sol-Gel Science and Technology, 2010. **54**(3): p. 355-362.
206. Carturan, G., et al., *Hybrid gels as host matrices of perfumed essences*. Journal of Sol-Gel Science and Technology, 1997. **8**(1-3): p. 1115-1119.
207. Yang, X., et al., *Direct synthesis and characterization of bifunctional Me-Zr-MCM-41*. Materials Letters, 2009. **63**(20): p. 1754-1756.
208. Ha, T.-J., et al., *The improvement of mechanical and dielectric properties of ordered mesoporous silica film using TEOS-MTES mixed silica precursor*. Ceramics International, 2008. **34**(4): p. 947-951.
209. Yunsheng, Z., et al., *Synthesis and heavy metal immobilization behaviors of slag based geopolymer*. Journal of hazardous materials, 2007. **143**(1): p. 206-213.
210. Aguiar, H., et al., *Structural study of sol-gel silicate glasses by IR and Raman spectroscopies*. Journal of Non-Crystalline Solids, 2009. **355**(8): p. 475-480.
211. Çetin, N.S., et al., *New transesterification reaction between acetylated wood and tetramethoxysilane: A feasibility study*. European Polymer Journal, 2005. **41**(11): p. 2704-2710.
212. Koç, K., F.Z. Tepehan, and G.G. Tepehan, *Characterization of MPS capped CdS quantum dots and formation of self-assembled quantum dots thin films on a glassy substrate*. Chalcogenide Lett, 2011. **8**: p. 239-247.
213. Trasferetti, B., C. Davanzo, and M. Bica de Moraes, *Infrared and Raman studies on films of organosiloxane networks produced by PECVD*. Macromolecules, 2004. **37**(2): p. 459-466.
214. Shu, Z., X. Jiao, and D. Chen, *Synthesis and photocatalytic properties of flower-like zirconia nanostructures*. CrystEngComm, 2012. **14**(3): p. 1122-1127.
215. Zhang, Y., et al., *Mullite fibres prepared by sol-gel method using polyvinyl butyral*. Journal of the European Ceramic Society, 2009. **29**(6): p. 1101-1107.

216. Erkov, V., et al., *Si-TiO<sub>2</sub> interface evolution at prolonged annealing in low vacuum or N<sub>2</sub> O ambient*. Applied surface science, 2000. **166**(1): p. 51-56.
217. Joseph, J. and E.D. Jemmis, *Red-, blue-, or no-shift in hydrogen bonds: a unified explanation*. Journal of the American Chemical Society, 2007. **129**(15): p. 4620-4632.
218. Zheludkevich, M.L., et al., *Triazole and thiazole derivatives as corrosion inhibitors for AA2024 aluminium alloy*. Corrosion Science, 2005. **47**(12): p. 3368-3383.
219. Hsu, C. and F. Mansfeld, *Technical note: concerning the conversion of the constant phase element parameter Y<sub>0</sub> into a capacitance*. Corrosion, 2001. **57**(9): p. 747-748.
220. Shi, H., F. Liu, and E. Han, *Corrosion behaviour of sol-gel coatings doped with cerium salts on 2024-T3 aluminum alloy*. Materials Chemistry and Physics, 2010. **124**(1): p. 291-297.
221. Conde, A., A. Durán, and J.J. de Damborenea, *Polymeric sol-gel coatings as protective layers of aluminium alloys*. Progress in Organic Coatings, 2003. **46**(4): p. 288-296.
222. Luo, C., *Role of Microstructure on Corrosion Control of AA2024-T3 Aluminium Alloy*. 2011.
223. De Rosa, R., et al., *Surface analysis of various methods of preparing Al 2024-T3 surfaces for painting*. Corrosion, 2000. **56**(4): p. 395-400.
224. Hughes, A., et al., *Study of deoxidation of 2024-T3 with various acids*. Materials science and technology, 2001. **17**(12): p. 1642-1652.
225. Mittal, K.L., *Adhesion aspects of polymeric coatings*. 1983: Plenum press.